**Algerian Democratic and Popular Republic**
**Ministry of Higher Education and Scientific Research**
**Abdelhamid Ibn Badis University – Mostaganem**
**Faculty of Exact Sciences and Computer Science**
**Department of Physics**
**Elaboration and Characterization Physico-Mechanical and Metallurgical of Materials Laboratory**

**Doctoral Thesis**
**In view of obtaining the Degree of PhD of Physics**

**Department: Physics**
**Specialty: Materials Physics**

Presented by:

**LATRECHE Laid**

**Title:**

# Ab initio study of disorder effects on the electronic and magnetic properties in quaternary Heusler alloys

**Defended on:** 07/04/2026

**In front of a jury of:**

| Name | Position | Grade | Affiliation |
|---|---|---|---|
| Mr SENOUCI Khaled | Chairman | Professor | University of Mostaganem |
| Mme MEGHOUFEL Zahira Faiza | Examiner | MCA | University of Mostaganem |
| Mr AMRANI Bouhalouane | Examiner | Professor | University of Oran 1 |
| Mr ABBASSA Hamza | Thesis supervisor | Professor | University of Mostaganem |

**Academic Year 2025-2026**

# Acknowledgements

I want to express my gratitude to my supervisor, **Prof. Hamza Abbassa**, for his support and for the time he devoted to reviewing my drafts and for his sharp insights that enhanced both the quality of this thesis and my methodology for research. His support and guidance made a real difference for me at every step of my PhD journey.

I am also deeply honoured to have this work evaluated by such a distinguished jury. I would like to sincerely thank **Prof. Khaled Senouci** for accepting to chair this committee. My gratitude also extends to **Dr. Zahira Faiza Meghoufel** for examining this manuscript. A special thanks goes to **Prof. Bouhalouane Amrani** from the University of Oran 1, who kindly accepted to travel to Mostaganem to examine this work; I am very grateful for the effort he made to be present today.

I'm truly grateful, to **Prof. Abdelkader Boukortt**, ECP3M laboratory Head, for his help and encouragement, and especially for supplying the necessary hardware and software for my computational tasks. Working with large systems required a great deal of time and computing power, and the high-performance machines he made available allowed me to complete my work much more effectively. I would also like to warmly thank our laboratory engineer, **Hammou Abdelhadi**, whose dedication to maintaining the lab and handling the day-to-day work behind the scenes created the conditions for smooth research.

My sincere thanks go as well to all the members of the ECP3M group for their collaboration, encouragement, and the friendly atmosphere they fostered, which made my time in the lab both productive and enjoyable. The spirit of the team and the good weather that accompanied our work made my experience look easy.

Finally, I want to thank my parents for their constant support and encouragement, which have been a source of strength for me in both difficult and joyful times. I would not have reached this point without them.

# Abstract

First-principles calculations, combined with the supercell approach, are employed to investigate the effects of atomic disorder on the electronic and magnetic properties of the CoFeMnZ (Z = Ge or Al) equiatomic quaternary Heusler alloy (LiMgPdSn-type). The ordered CoFeMnGe alloy is a nearly-half-metallic ferromagnet and can be transformed into full half-metal at 28.35 GPa of pressure. The ideal CoFeMnAl is half-metallic; Both compounds follow the Slater-Pauling rule with Curie temperature $T_C$ above 300 K. We analysed twelve antisite and six swap disorder configurations. For CoFeMnGe Calculations show that the $Fe_{Ge}$ antisite is the most energetically favourable defect (-9.95 eV), followed by the $Fe_{Mn}$, $Co_{Ge}$ and $Co_{Mn}$ antisite structures. Half-metallicity is completely lost for $Co_{Ge}$, $Ge_{Fe}$ antisite and CoGe, FeGe swap defects. $Ge_{Co}$ and $Mn_{Ge}$ antisite, FeGe and MnGe swap enhance half-metallicity by pushing the $V_{BM}$ below the Fermi level. The $Fe_{Mn}$ antisite gives 4.135 $\mu_B$/*f.u*, which is very close to the experimental value of 4.2 $\mu_B$. For CoFeMnAl Calculations show that the $Fe_{Mn}$ antisite is the most energetically favourable defect (-1.25 eV), followed by the FeCo antisite and the MnAl swap. The disorder generally contracts the spin-down gap. Half-metallicity is largely preserved but completely lost for $Co_{Al}$, $Co_{Mn}$ antisite and CoAl, CoMn swap defects. The $Fe_{Mn}$ antisite gives 3.12 $\mu_B$, which is very close to the experimental value of 3.10 $\mu_B$. Disorder has a significant effect on the magnetic moment and Curie temperature for both compounds. This study demonstrates the importance of considering disorder when predicting the properties of Heusler alloys.

Keywords: Quaternary Heusler, Disorder, half metal, FP-LAPW calculations.

# Résumé

Des calculs de premiers principes, combinés à l'approche de super-cellule, sont employés pour étudier les effets du désordre atomique sur les propriétés électroniques de l'alliage quaternaire de Heusler équiatomique CoFeMnZ (Z = Ge ou Al) (type LiMgPdSn). L'alliage ordonné CoFeMnGe est un ferromagnétique quasi-demi-métallique et peut être transformé en demi-métal à 28.35 GPa de pression. Le CoFeMnAl idéal est demi-métallique ; les deux composés suivent la règle de Slater-Pauling avec une température de Curie TC supérieure à 300 K. Nous avons analysé douze configurations de désordre antisite et six configurations d'échange. Pour CoFeMnGe, les calculs montrent que l'antisite FeGe est le défaut énergétiquement le plus favorable (-9,95 eV), suivi par les structures antisite FeMn, CoGe et CoMn. La demi-métallicité est complètement perdue pour les défauts antisite CoGe, GeFe et d'échange CoGe, FeGe. Les antisites GeCo et MnGe, les échanges FeGe et MnGe améliorent la demi-métallicité en poussant le VBM en dessous du niveau de Fermi. L'antisite FeMn donne 4,135 μB/u.f., ce qui est très proche de la valeur expérimentale de 4,2 μB. Pour CoFeMnAl, les calculs montrent que l'antisite FeMn est le défaut énergétiquement le plus favorable (-1,25 eV), suivi par l'antisite FeCo et l'échange MnAl. Le désordre contracte généralement la bande interdite spin-down. La demi-métallicité est largement préservée mais complètement perdue pour les défauts antisite CoAl, CoMn et d'échange CoAl, CoMn. L'antisite FeMn donne 3,12 μB, ce qui est très proche de la valeur expérimentale de 3,10 μB. Le désordre a un effet significatif sur le moment magnétique et la température de Curie pour les deux composés. Cette étude démontre l'importance de considérer le désordre lors de la prédiction des propriétés des alliages de Heusler.

Mots-clés : Heusler quaternaire, Désordre, demi-métal, calculs FP-LAPW.

## الملخص:

تم استخدام حسابات المبادئ الأولية ونظرية الكثافة الوظيفية، مقترنة بطريقة الخلية الفائقة، لدراسة تأثيرات الاضطراب الذري على الخصائص الإلكترونية لسبيكة هيوسلر الرباعية متساوية الذرات CoFeMnZ حيث (Z = Ge أو Al) من نوع (LiMgPdSn) تُعد سبيكة CoFeMnGe المرتبة مادة فيرومغناطيسية شبه نصف معدنية تقريبًا، ويمكن تحويلها إلى نصف معدن كامل عند ضغط قدره 28.35 جيجا باسكال. أما سبيكة CoFeMnAl المثالية فهي نصف معدنية؛ ويتبع كلا المركبين قاعدة سلاتر-باولينج (Slater-Pauling) مع درجة حرارة كوري ($T_C$) أعلى من 300 كلفن.

قمنا بتحليل اثني عشر تشكيلًا لاضطراب الموقع البديل (antisite) وستة تشكيلات لاضطراب التبادل (swap) بالنسبة لمركب CoFeMnGe ، تظهر الحسابات أن عيب الموقع البديل $Fe_{Ge}$ هو الأكثر تفضيلًا من حيث الطاقة (-9.95 إلكترون فولت)، يليه هياكل الموقع البديل $Fe_{Mn}$ و $Co_{Ge}$ و$Co_{Mn}$ تُفقد الخاصية نصف المعدنية تمامًا في عيوب الموقع البديل $Co_{Ge}$ و $Ge_{Fe}$ وعيوب التبادل CoGe و FeGe بينما تعزز عيوب الموقع البديل $Ge_{Co}$ و $Mn_{Ge}$ وعيوب التبادل FeGe و MnGe الخاصية نصف المعدنية عن طريق دفع قمة نطاق التكافؤ ($V_{BM}$) إلى ما دون مستوى فيرمي. يعطي عيب الموقع البديل $Fe_{Mn}$ عزمًا مغناطيسيًا قدره 4.135 بور ماغنيتون/وحدة صيغة، وهو قريب جدًا من القيمة التجريبية البالغة 4.2 بور ماغنيتون.

أما بالنسبة لمركب CoFeMnAl، فتُظهر الحسابات أن عيب الموقع البديل $Fe_{Mn}$ هو الأكثر تفضيلًا من حيث الطاقة (-1.25 إلكترون فولت)، يليه عيب الموقع البديل $Fe_{Co}$ وتبادل $Mn_{Al}$ .يؤدي الاضطراب عمومًا إلى تقليص فجوة العزم المغزلي السالب .(spin-down gap) تظل الخاصية نصف المعدنية محفوظة إلى حد كبير، لكنها تُفقد تمامًا في عيوب الموقع البديل $Co_{Al}$ و $Co_{Mn}$ وعيوب التبادل CoAl و CoMn. يعطي عيب الموقع البديل $Fe_{Mn}$ عزمًا قدره 3.12 بور ماغنيتون، وهو قريب جدًا من القيمة التجريبية البالغة 3.10 بور ماغنيتون.

للاضطراب تأثير كبير على العزم المغناطيسي ودرجة حرارة كوري لكلا المركبين. توضح هذه الدراسة أهمية أخذ الاضطراب بعين الاعتبار عند التنبؤ بخصائص سبائك هيوسلر.



الكلمات المفتاحية :هيوسلر الرباعية، الاضطراب، نصف معدن، حسابات الموجة المستوية المعززة خطيًا بالجهد الكامل (FP-LAPW).

# Table of content

# List of tables

# List of figures

# List of abbreviations

**DFT**: Density Functional Theory

**FP-LAPW**: Full-Potential Linearized Augmented Plane Waves

**GGA**: Generalized Gradient Approximation

**PBE**: Perdew-Burke-Ernzerhof

**mBJ**: modified Becke-Johnson

**DFPT**: Density Functional Perturbation Theory

**SCF**: Self-Consistent Field

**MFA**: Mean-Field Approximation

**MC**: Monte Carlo

**VWN**: Vosko-Wilk-Nusair

**SPS**: Spark Plasma Sintering

**RMT**: Muffin-Tin Radius

**RKmax**: Basis Set Cut-off

**BZ:** Brillouin Zone

**$E_F$:** Fermi Level

**FAST**: Field Assisted Sintering Technology

**FCC**: Face-Centered Cubic

**BCC**: Body-Centered Cubic

**HCP**: Hexagonal Close-Packed

**CD**: Cubic-Diamond

**EQH**: Equiatomic Quaternary Heusler

**ICSD**: Inorganic Crystal Structure Database

**SB**: Strukturberichte

**SG**: Space Group

**FN**: First-Neighbour

**SN**: Second-Neighbour

**TN**: Third-Neighbour

**DOS**: Density of States

**TDOS**: Total Density of States

**PDOS**: Partial Density of States

**IPDOS**: Integrated Partial Density of States

**BS**: Band Structure

**VBM**: Valence Band Maximum

**CBM**: Conduction Band Minimum

**NM**: Non-Magnetic

**FM**: Ferromagnetic

**AFM**: Anti-Ferromagnetic

**HM**: Half-Metallic

**NHM**: Nearly-Half-Metallic

**HMF**: Half-Metallic Ferromagnet

**NHMF**: Nearly-Half-Metallic Ferromagnet

**SGS**: Spin Gapless Semiconductor

**DMI**: Dzyaloshinskii-Moriya Interaction

**GMR**: Giant Magnetoresistance

**TMR**: Tunnelling Magnetoresistance

**MRAM**: Magnetoresistive Random-Access Memory

**HDD**: Hard Disk Drive

**STT**: Spin Torque Transfer

**Tc**: Curie Temperature

$\mu_B$: Bohr Magneton

$E_f$: Formation Energy

$E_{fd}$: Formation Energy of Disorder

$E_b$: Pair Binding Energy

**B**: Bulk Modulus

**B'**: Pressure derivative of the bulk modulus

**G**: Shear Modulus

**E**: Young's Modulus

**Ae**: Zener Anisotropy Factor

$v_l$: Longitudinal elastic wave velocity

$v_t$: Transverse elastic wave velocity

$v_m$: Average acoustic velocity

$\sigma$: Poisson's Ratio

$\rho$: Density

$\theta_D$: Debye Temperature

$J_{ij}$: Exchange coupling parameters

# Introduction

Spintronics is a dynamic and rapidly advancing research topic that explores the intrinsic spin degree of freedom of electrons, along with their charge, to enable innovative capabilities in electronic devices. Initially, electronics relied merely on charge transport; however, spintronics expands this framework by employing spin-polarised currents, hence enabling faster, energy-efficient, and multifunctional devices. Giant Magnetoresistance (GMR) and Tunnelling Magnetoresistance (TMR) [1] are two major phenomena in this area of science that are now crucial to modern spintronic technologies. These effects have fundamentally transformed various applications, including ultra-sensitive magnetic sensors in biomedical and automotive sectors, high-density digital data storage technologies, and innovative non-volatile memories such as magnetoresistive random-access memory (MRAM), which integrates speed, durability, and low power consumption. The efficacy of these applications fundamentally relies on the meticulous regulation and manipulation of electron spins and magnetic orientations within sophisticated multilayered materials and nanoscale heterostructures.

In the broad realm of spintronic materials [2], Heusler compounds have garnered significant attention owing to their remarkable tunability and intricate interaction between electrical and magnetic characteristics. These ternary and quaternary intermetallic alloys are distinguished by their capacity to demonstrate half-metallicity a distinctive electronic arrangement wherein electrons of one spin orientation conduct metallically, facilitating unimpeded conduction, while electrons of the opposing spin experience an electronic band gap, functioning as semiconductors or insulators. This yields complete spin polarisation at the Fermi level, a highly sought-after characteristic that renders Heusler alloys exemplary candidates for applications necessitating effective spin injection, detection, and transport. Furthermore, when it comes to half-metallic properties [3], Heusler compounds exhibit significant chemical flexibility, enabling adjustments to their composition and crystal structure that optimise Curie temperatures, magnetic anisotropy, and other key physical characteristics. Such features have established Heusler alloys as leaders in the forthcoming generation of spintronic devices.

However, the practical realisation of these materials' inherent potential is significantly affected by atomic disorder [4, 5], which is unavoidable in any real material. In Heusler alloys, these imperfections can appear as vacancies, antisite defects, or interstitials, each possessing the potential to disrupt the equilibrium of electronic and magnetic interactions [6, 7]. Defects can serve as scattering centres that modify the spin polarisation and coherence, hence impairing essential properties, including magnetoresistance and spin-transfer torque efficiency. On the other hand, if precisely controlled, these defects provide a significant tool to manipulate material properties, transforming prospective liabilities into benefits. The role of defects underscores the importance of comprehending their creation mechanisms and their impact on macroscopic material behaviour.

This thesis investigates the influence of disorder on the electrical and magnetic properties of quaternary Heusler alloys within the CoFeMnZ family, where Z represents either Ge or Al. These compounds offer an optimal framework for examining the influence of structural defects on spin-dependent events, including GMR and TMR effects. This study aims to elucidate the microscopic mechanisms by which disorder alters electronic band structures, magnetic exchange interactions [4], and transport parameters by integrating experimental characterisation with theoretical modelling. The insights obtained aim to inform the systematic design of Heusler materials with enhanced performance, thereby propelling the advancement of spintronics towards more efficient, dependable, and scalable technologies.

The structure of this thesis is organized to progressively build a comprehensive understanding of the complex phenomena associated with disorder in Heusler alloys. The first chapter establishes the theoretical foundation of spintronics, focusing on the fundamental principles of Giant Magnetoresistance and Tunnelling Magnetoresistance. The second chapter delves into the physical and chemical properties of Heusler compounds, their crystal structures, and their role as spintronic materials. The third chapter explores defect types, formation mechanisms, and their effects on solid-state materials, with particular attention to defects in Heusler alloys. Chapter four presents detailed results and discussions, synthesizing experimental data and theoretical insights to elucidate the impact of disorder on the electronic and magnetic behaviour of CoFeMnZ alloys. Supplementing these analyses, multiple comprehensive methodological details, including the use of

Wien2k FP-LAPW [8] with GGA and mBJ [5] corrections for electronic structure calculations, Phonopy combined with DFPT for lattice dynamics, SPRKKR [9] for exchange coupling computations, and Vampire for Monte Carlo simulations [10, 11] and temperature-dependent magnetic properties.

## References:


1. Bainsla, L., Suresh, K.G.: Equiatomic quaternary Heusler alloys: a material perspective for spintronic applications.
2. Felser, C., Hirohata, A.: Springer Series in Materials Science 222 Heusler Alloys Properties, Growth, Applications.
3. Elphick, K., Frost, W., Samiepour, M., Kubota, T., Takanashi, K., Sukegawa, H., Mitani, S., Hirohata, A.: Heusler alloys for spintronic devices: review on recent development and future perspectives. Sci. Technol. Adv. Mater. 22, 235–271 (2021). https://doi.org/10.1080/14686996.2020.1812364
4. Kirievsky, K., Gelbstein, Y., Fuks, D.: Phase separation and antisite defects iN the thermoelectric TiNiSn half-Heusler alloys. J. Solid State Chem. 203, 247–254 (2013). https://doi.org/10.1016/j.jssc.2013.04.032
5. Hamad, B., Hu, Q.M.: The effect of defects on the electronic and magnetic properties of Fe2MnSi Heusler alloy. Phys. Status Solidi B Basic Res. 248, 2893–2898 (2011). https://doi.org/10.1002/pssb.201147305
6. Freysoldt, C., Grabowski, B., Hickel, T., Neugebauer, J., Kresse, G., Janotti, A., Van De Walle, C.G.: First-principles calculations for point defects in solids. Rev. Mod. Phys. 86, 253–305 (2014). https://doi.org/10.1103/RevModPhys.86.253
7. Arrigoni, M., Madsen, G.K.H.: A comparative first-principles investigation on the defect chemistry of TiO2 anatase. Journal of Chemical Physics. 152, (2020). https://doi.org/10.1063/1.5138902
8. Blaha, P., Schwarz, K., Tran, F., Laskowski, R., Madsen, G.K.H., Marks, L.D.: WIEN2k: An APW+lo program for calculating the properties of solids. Journal of Chemical Physics. 152, (2020). https://doi.org/10.1063/1.5143061/16727314/074101_1_ACCEPTED_MANUSCRIPT.PDF
9. Wei, X.P., Zhang, Y.L., Sun, X.W., Song, T., Guo, P., Gao, Y., Zhang, J.L., Zhu, X.F., Deng, J.B.: Exchange interactions and Curie temperatures in Fe2 NiZ compounds. J. Alloys Compd. 694, 1254–1259 (2017). https://doi.org/10.1016/J.JALLCOM.2016.10.105
10. Evans, R.F.L., Fan, W.J., Chureemart, P., Ostler, T.A., Ellis, M.O.A., Chantrell, R.W.: Atomistic spin model simulations of magnetic nanomaterials. Journal of Physics: Condensed Matter. 26, 103202 (2014). https://doi.org/10.1088/0953-8984/26/10/103202
11. Wei, X.P., Zhou, Y.H.: First-principles and Monte Carlo studies of the Fe2NiZ compounds on exchange interactions and Curie temperatures. Intermetallics (Barking). 93, 283–289 (2018). https://doi.org/10.1016/j.intermet.2017.10.006

# Chapter I : Heusler compounds

## I.1 Introduction:

### I.1.1. Historical Background:

In 1903, Fritz Heusler revealed the discovery of a ferromagnetic substance at room temperature, which is curiously created by the elements Cu, Mn, and Al that show no magnetism at room temperature [1]. In 1934, Otto Heusler (Fritz Heusler son) and Bradley identified the crystal structure of $Cu_2MnAl$, which had previously been unknown [2,3]. Following Heusler's discovery, Nowotny and Juza presented results on a new set of materials, all main group element compounds, now known as Nowotny-Juza Phases. In the same continuation, L. Castelliz was the first to synthesize NiMnSb, establishing the link between Nowotny-Juza phases and Heusler compounds [4,5]. Currently, these phases are known as half-Heusler compounds, meaning one of the four FCC sublattices is vacant. Filling the fourth sublattice creates compounds ranging from half to full Heusler, noted as XYZ and $X_2YZ$, where X and Y are transition metal elements and Z is a main group element. When one of the two X atoms is replaced by a different transition metal X', a new quaternary Heusler alloy with the formula XX'YZ and F-43m symmetry (space group 216) is obtained [6–8]. Due to their greater flexibility in component selection and lattice site arrangement, compounds from the quaternary Heusler family have proven to be promising for spintronic-based applications. exhibiting half-metallicity, high Curie temperature, and spin gapless semiconducting properties [9].

## I.2 Nomenclature and Classification of Heusler alloys:

Heusler alloys are divided into two groups: Compounds with the chemical formula $X_2YZ$, which have four fcc sublattices, and compounds with the formula XYZ, which contain three fcc sublattices. Full-Heusler $X_2YZ$ compounds can be formed by combining different elements according to the color palette indicated on the periodic table in the **Figure 1**.

However, in some cases, Y is replaced by either a rare-earth element or an alkaline-earth metal. Traditionally, in the case of full-Heusler compounds, the metal that appears twice is

placed at the beginning of the formula, while the main group element is placed at the end [10–12].

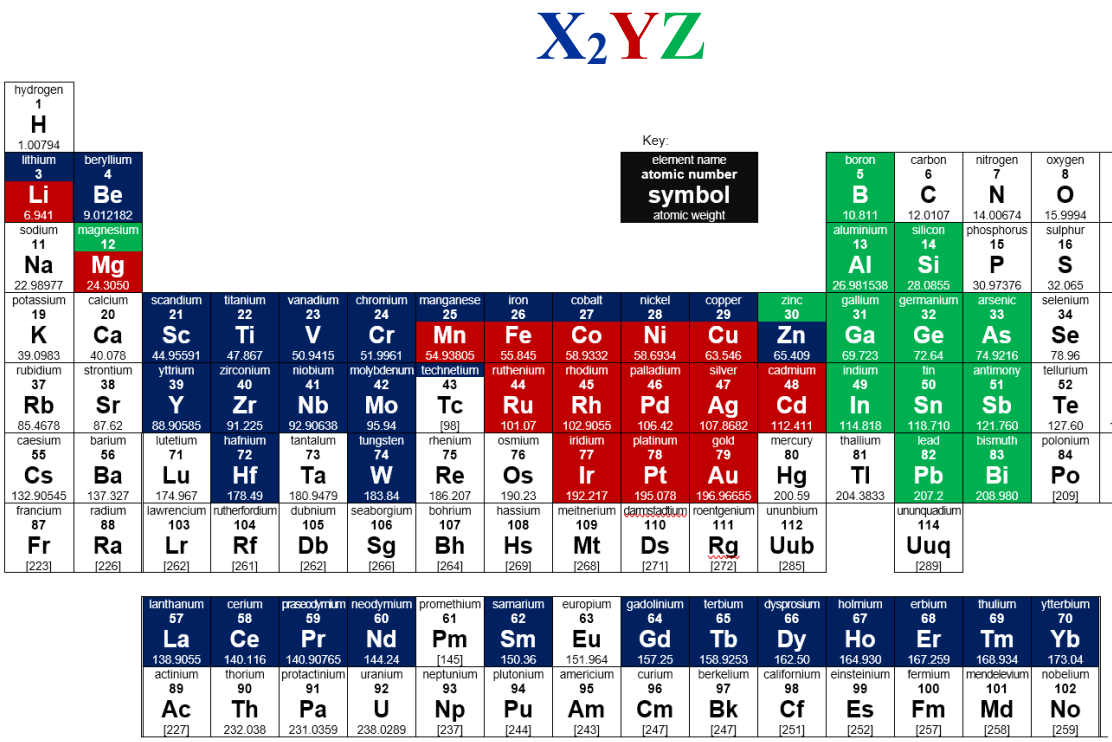


**Figure 1.** Periodic table of element $X_2YZ$ Heusler

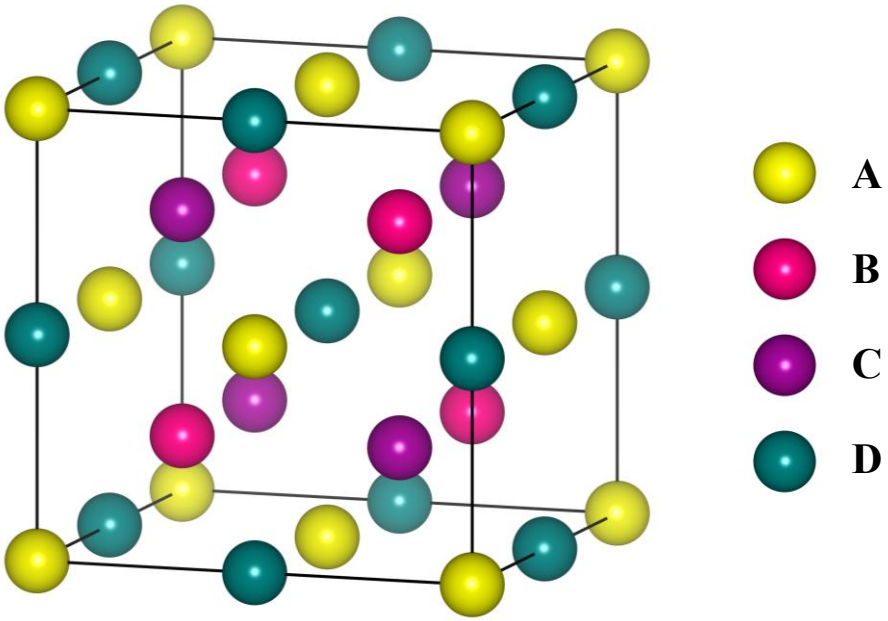


**Figure 2.** The different structures of the Heusler compounds

**Table 1:** Different variations of Heusler compound.

| | A | B | C | D |
|---|---|---|---|---|
| Full Heusler | X | Y | X | Z |
| Half Heusler | X | Y | | Z |
| Quaternary Heusler | X | Y | X' | Z |
| Inverse Heusler | X | X | Y | Z |

### I.2.1. Half Heusler Alloys (XYZ):

The $C1_b$-type structure of Half Heusler alloy structure (space group no. 216, $F\bar{4}3m$) matches the $L2_1$ structure of a full Heusler alloy ($X_2YZ$) but one X atom is removed. The absence of inversion symmetry resulting from an unoccupied X site and the low coordination number of the d-band metals in Half Heusler alloys is considered crucial for the unique electronic and magnetic properties of these materials [13]. Several research groups have identified three potential different atomic configurations, designated as Type-I, Type-II, and Type-III phases, resulting from the absence of the X atom in the Half Heusler alloys [12,14]

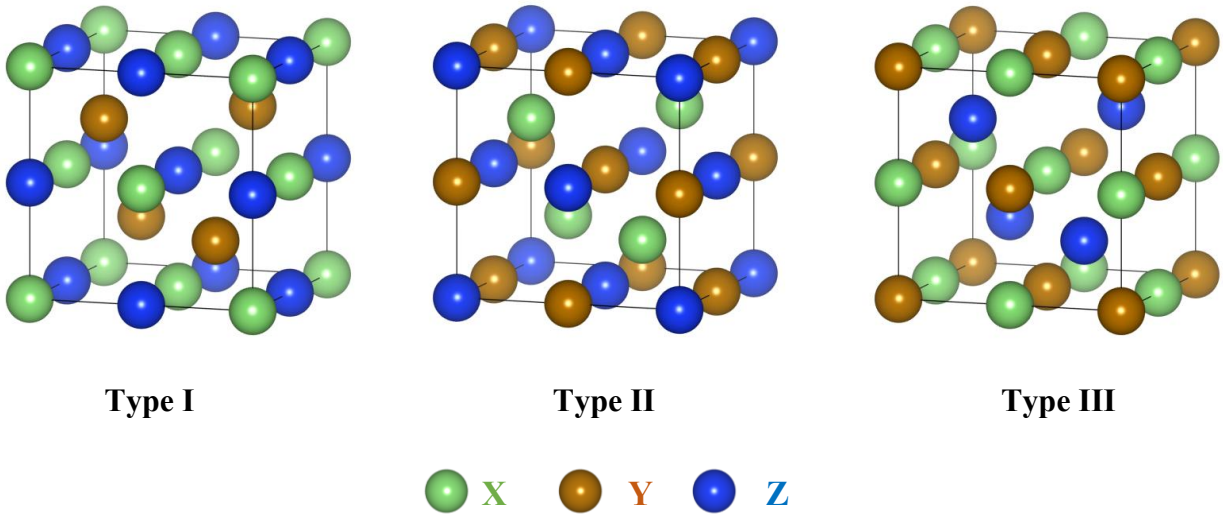


**Figure 3.** Different structure types for half Heusler compounds.

**Table 2:** Atomic arrangement of XYZ half Heusler compound in $C1_b$ structure.

| Structure | Wyckoff coordinates | | |
|---|---|---|---|
| | **4a (0 0 0)** | **4b (1/4 1/4 1/4)** | **4c (1/2 1/2 1/2)** |
| **Type I** | X | Y | X’ |
| **Type II** | Z | X | X’ |
| **Type III** | Z | Y | X |

## I.2.2. Full Heusler Alloys ($X_2YZ$):

Full-Heusler alloys are ternary compounds with an elemental chemical arrangement of 2:1:1, represented by the chemical formula $X_2YZ$. They often exhibit two possible phases of crystal structures: the $AlCu_2Mn$ type, which crystallizes in the cubic $L2_1$ structure with the space group $Fm\bar{3}m$ (SG number 225). In this structure, the X, Y, and Z atoms occupy the Wyckoff positions 8c (1/4,1/4, 1/4), 4a (0, 0,0) and 4b (1/2, 1/2, 1/2), respectively. The second structure is the $CuHg_2Ti$ type, crystallising in the cubic $X_A$ structure with the space group $F\bar{4}3m$ (SG number 216). In this structure, the X atoms are located at non-equivalent positions 4a (0, 0,0) and 4c (1/4, 1/4, 1/4), while Y and Z atoms occupy the 4b (1/2, 1/2, 1/2) and 4d (3/4, 3/4, 3/4) positions, respectively. Both structures consist of interpenetrating FCC lattices, each occupied by X, Y, and Z atoms [12]. In the presence of the Jahn Teller effect, the ideal cubic structure can be transformed into a tetragonal structure resulting of a distortion along the c-axis. In this situation, the two cubic structures, $L2_1$ and XA, become tetragonal structures crystallizing in the space I4/mmm (SG number139) and I-4m2 (SG number 119), respectively [8, 15]. The tetragonal structure with the space group I4/mmm is often referred to as the $D0_{22}$ structure.

**Table 3:** Atomic arrangement of $X_2YZ$ full Heusler compound.

| Structure | Wyckoff coordinates | | | |
|---|---|---|---|---|
| | **4a (0 0 0)** | **4b (1/4 1/4 1/4)** | **4c (1/2 1/2 1/2)** | **4d (3/4 3/4 3/4)** |
| **$L2_1$ (Conventional)** | X | Y | X | Z |
| **$X_A$ (Inverse Heusler)** | Z | X | Y | Y |

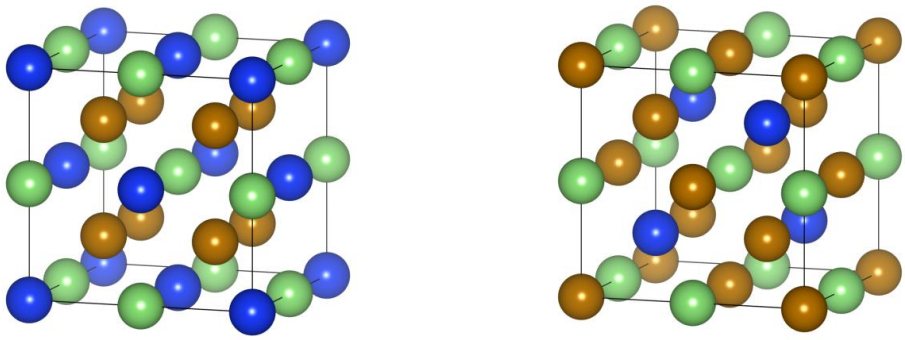


**Figure 4.** Full Heusler compounds ordered structures.

### I.2.3. Quaternary Heusler Alloys (XX'YZ):

Quaternary Heusler compounds with the 1:1:1:1 stoichiometry has the general formula XX'YZ. There are two different elements X and X'. They are located at the 4a (0, 0, 0), and 4d (1/4, 1/4, 1/4). positions, respectively, Y is placed on 4b (1/2, 1/2, 1/2), and Z on 4c (3/4, 3/4, 3/4), Where the valence of X' is lower than the valence of X atoms and the valence of the Y element is lower than the valence of both X and X'. The sequence of the atoms along the fcc cube's diagonal is X-Y-X'-Z which is energetically the most stable [16]. This structure has the LiMgPdSn structure [9,17–19] and crystallises in (space group no. 216, $F\bar{4}3m$).

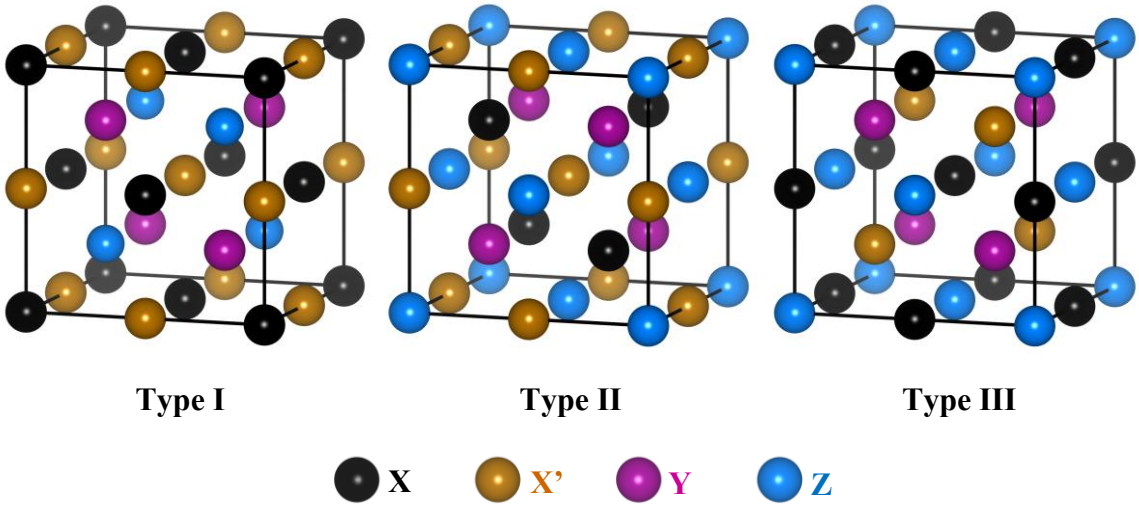


**Figure 5.** Crystalline structures of XX'YZ quaternary Heusler Y-Types alloy.

**Table 4:** Possible different types of atomic arrangement of XX'YZ quaternary Heusler compound.

| Structure | Wyckoff coordinates | | | |
|---|---|---|---|---|
| | **4a (0 0 0)** | **4b (1/4 1/4 1/4)** | **4c (1/2 1/2 1/2)** | **4d (3/4 3/4 3/4)** |
| **Type I** | X | Y | X' | Z |
| **Type II** | Z | X | X' | Y |
| **Type III** | Z | Y | X | X' |

## I.3 Synthesis of Heusler compounds:

There are several methods for synthesising Heusler compounds, such as the arc melting of stoichiometric quantities of high-purity elements and flash sintering.

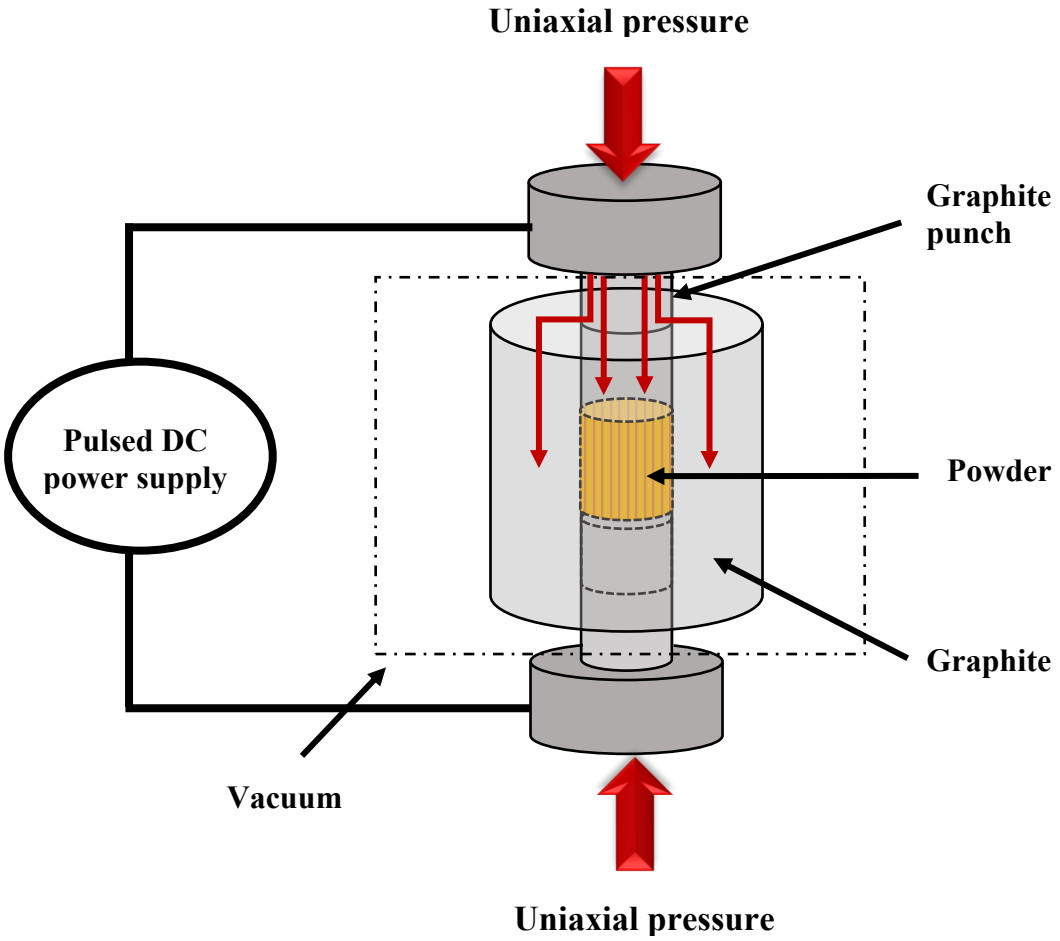


**Figure 6.** Schematic diagram of the operating principle of Spark Plasma Sintering.

Flash sintering (spark plasma sintering), or "Spark Plasma Sintering as illustrated in **figure 6**," identified by SPS, is a sintering and synthesis technique that first appeared in 1930. It consists of passing a pressure-activated, low-voltage, pulsed direct current to rapidly sinter nanosized powder materials. Nowadays, the FAST/SPS technique is widely used. It is a mechanical loading system that acts simultaneously with a high-power electrical circuit, placed in a controlled atmosphere, where low voltages produce high currents. Thanks to the compact geometry of the die, sintering cycles with heating rates as high as 1000 °C $min^{-1}$ are possible. Standard cooling rates up to 150 °C $min^{-1}$ are possible (Figure 8).

## I.4 Magnetism in Heusler compounds:

### I.4.1. Introduction

Scientific studies on magnetism have continued for countless years; early observations record back to the times of the Iron Age. First used for navigation, lodestone (magnetite) possessed natural magnetic properties that allowed the early compass devices to be developed by aligning with Earth's magnetic field. Further research was grounded in the realisation that magnetic poles could interact, attract or repel and that magnetite could draw iron.

### I.4.2. Origin of magnetism:

Magnetism encompasses a set of physical phenomena in which objects exert attractive or repulsive forces on other materials. These forces arise from electric currents and the magnetic moments of fundamental elementary particles, which generate the magnetic field responsible for the forces.

There are two types of external sources of a magnetic field:

- the intrinsic magnetic moment of particles, known as spin (which is the origin of permanent magnets).
- and electric current, that is, the collective movement of electric charges.

The coupling between spins and the crystal structure determines the type of magnetism.

### I.4.3. Magnetic Ordering (collinear magnetism):

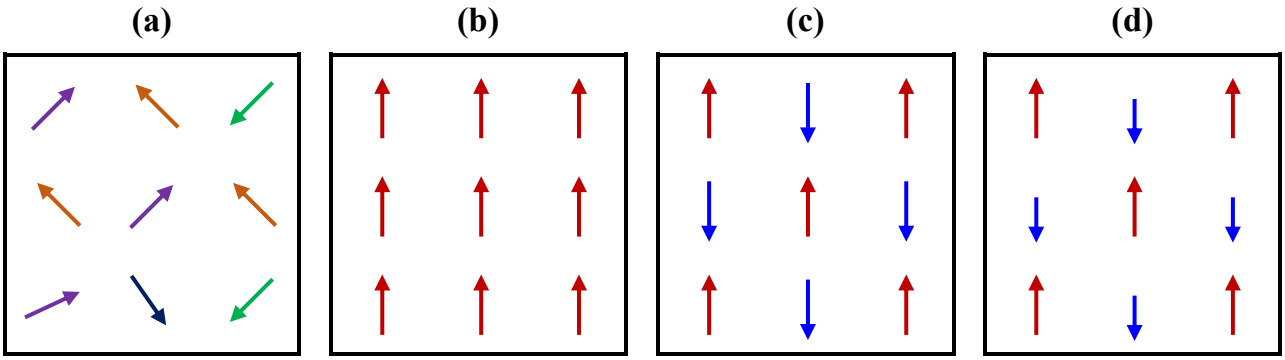


**Figure 7.** Schematic diagrams of the alignment of magnetic moments, (a) in paramagnetic materials at all temperatures, and (b) in ferromagnetic materials, (c) in antiferromagnetic materials, and (d) in ferrimagnetic materials at low temperatures.

### I.4.4. Diamagnetism:

Diamagnetic behaviour is characterised by a very weak and negative susceptibility to magnetic fields. A diamagnetic material is slightly repelled by a magnetic field and does not retain magnetic properties when the external magnetic field is removed. Diamagnetic materials are solids with paired electrons and, therefore, no permanent magnetic moment per atom. Their magnetic properties arise from the realignment of electronic orbits under the influence of an external magnetic field [20–22]. Most elements in the periodic table, including Copper, Silver, and Gold, are diamagnetic.

### I.4.5. Paramagnetism:

In the absence of an applied magnetic field, paramagnetic materials exhibit no net magnetic moment. At room temperature, thermal agitation induces disorder in the alignment of magnetic moments. Individual magnetic moments cancel each other out, resulting in zero overall magnetization of the material. However, these magnetic moments align in the direction of the applied magnetic field when it is present [21,22]. Consequently, paramagnetic materials are characterized by a positive magnetic susceptibility, as observed in Aluminum, Manganese, and Tungsten.

### I.4.6. Ferromagnetism:

Ferromagnetic materials possess the property of becoming magnetic, that is, to become magnetized, when placed in a magnetic field and to retain a portion of this

magnetism when the field is removed. Ferromagnetic materials consist of metallic elements such as iron (especially), nickel, and cobalt, which allow them to take on a strong magnetisation [22]. Ferromagnetic materials are divided into small domains within which all atoms have a parallel magnetization. These domains tend to align in the direction of an external magnetic field, which gives the material a strong magnetisation. Furthermore, the magnetic moments of each atom can align spontaneously within these domains, even in the absence of an external field. Ferromagnetic substances are used for their magnetic properties because not only can they be strongly magnetized, but they can also remain so, thanks to the phenomenon of magnetic hysteresis. This is referred to as remanent magnetization.

### I.4.7. Antiferromagnetism:

Unlike ferromagnetic materials, in antiferromagnetic materials, the exchange interaction between neighbouring atoms leads to an antiparallel alignment of atomic magnetic moments. The total magnetization of the material is therefore zero. The magnetic susceptibility of these materials is positive but generally weaker than that of ferromagnetic materials [20].

In the periodic table, the only element possessing antiferromagnetic properties at room temperature is chromium. Generally, antiferromagnets are ceramics composed of transition metals along with oxygen or sulfur.

### I.4.8. Ferrimagnetism:

Somewhat situated between paramagnetism (all electrons orient in the same direction) and antiferromagnetism (electrons orient in pairwise opposite directions), we find ferrimagnetism: the magnetic moments of the electrons are indeed opposed in pairs, but those aligned with the external magnetic field are stronger than those in the opposite direction [21]. The total magnetic moment in one direction is therefore greater than that in the other direction, and consequently, the total magnetic moment of the sample is not zero. Ferrimagnetism is observed in materials containing two types of atoms that behave like magnets of different strengths oriented in opposite directions.

## I.5 Non collinear magnetism

Non-collinear magnetism, refers to a stable, spatially non-uniform configuration of magnetic moments (spins) that deviates from a simple collinear order (e.g., ferromagnetic or antiferromagnetic). These are not imperfections in the crystal lattice, but rather stable textures or "defects" *within the magnetic order itself*. Their stability often arises from their topological nature, meaning they possess a characteristic winding number that cannot be continuously undone, similar to a knot in a rope. Their existence is governed by a competition between fundamental magnetic interactions, including the Heisenberg exchange, Dzyaloshinskii-Moriya interaction (DMI) [23], magnetic anisotropy, and magnetostatic (dipolar) energy (**Figure 8**).

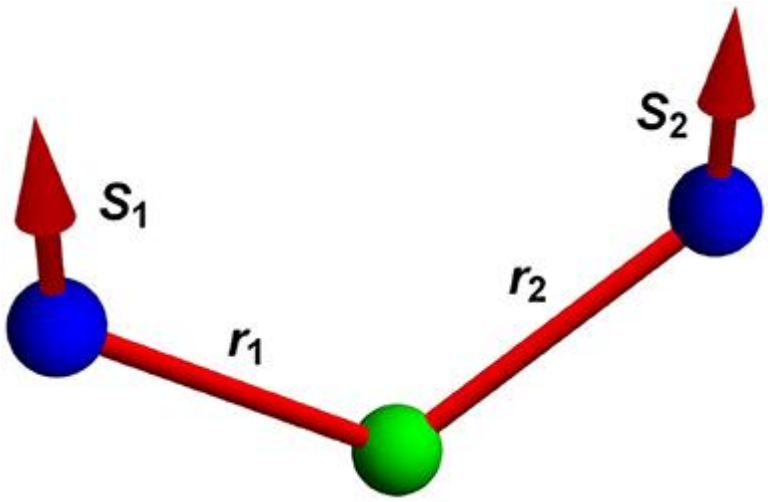


**Figure 8.** Interaction between two neighbouring spins is mediated by the non-magnetic atom. The direction of DMI vector resulting from such interaction is defined by the bond vectors, i.e., $D_{12} \propto r_1 \times r_2$.

### I.5.1. Spins spirals:

A spin spiral is a particular, non-collinear magnetic structure in which the magnetic moments (spins) of atoms are not aligned parallel or anti-parallel (as in standard ferromagnets or antiferromagnets). Instead, the value of magnetisation and the direction of the spins rotates **Figure 9** continuously from one atomic site to the next along a specific direction in the crystal lattice [24].

Spin spirals arise when "simple" magnetic ordering (all up or up-down) is frustrated by competing forces due to:

- Frustrated Exchange: The interaction between immediate neighbours wants them parallel (ferromagnetic), but the interaction with further neighbours wants them anti-parallel. The compromise is to rotate slightly, satisfying neither fully but lowering the total energy.
- Dzyaloshinskii-Moriya Interaction (DMI) [23]: The absence of inversion symmetry twists the magnetic structure into a spiral form.

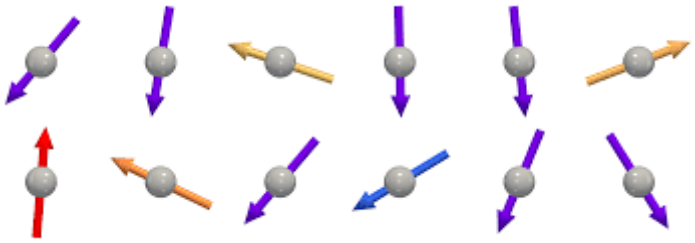

**Figure 9.** Schematic illustrations of spin spirals

### I.5.2. Magnetic skyrmions:

In 1962, Tony Skyrme proposed a model of a nucleon to describe the stable field configuration of a certain class of nonlinear sigma models [25]. In 1980s, Bogdanov and Yablonskii predicted a type of vortex-like magnetic structure (**Figure 10**) in some low-symmetry magnetic crystal structures [26,27] called magnetic skyrmion, which was first coined in a theoretical work by Rößler et al. [28] in 2006. Three years later, their prediction was experimentally demonstrated in reciprocal space using neutron scattering in chiral magnetic MnSi [29] and in real space using Lorentz transmission electron microscopy (LTEM) in chiral magnetic $Fe_{0.5}Co_{0.5}Si$ [30]. Since then, several promising features of magnetic skyrmions such as nontrivial topology, small size, and high mobility driven by electric current have been reported. These advantages make magnetic skyrmions suitable to study magnetic topological defects and as information carriers in future high-density memory devices with low energy consumption.

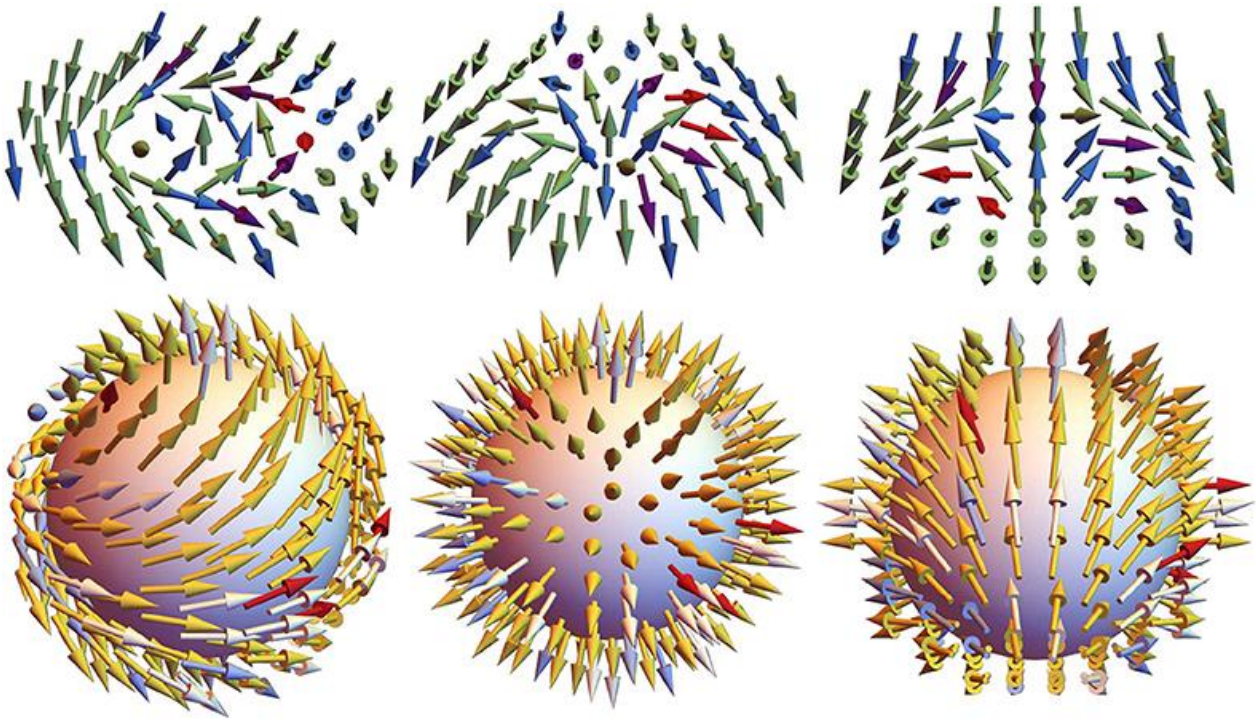

**(a)** **(b)** **(c)**

**Figure 10.** Schematic illustrations of four types of magnetic skyrmions: (a) Bloch-type skyrmion, where spins rotate perpendicularly to radial direction; (b) Néel-type skyrmion, where spins rotate along radial direction; (c) Antiskyrmion, where spins located on two diagonal lines rotate along radial direction, while other spins rotate perpendicularly to radius.

## I.6 Half-metallic compounds:

In 1983, Groot and colleagues formulated a theoretical prediction concerning half-metallicity in Heusler alloys. Their research established the theoretical foundations of half-metallicity in these materials, with the goal of calculating the band structure of the half-Heusler alloy NiMnSb [10,14]. A common approach is to examine the electronic density of states $N(E_F)$ at the Fermi level for majority spin ($N\uparrow(E_F)$) and minority spin ($N\downarrow(E_F)$). This analysis allows the spin polarization, representing the spin asymmetry, to be defined by the following expression:

$$P = \frac{\rho\uparrow(E_F) - \rho\downarrow(E_F)}{\rho\uparrow(E_F) + \rho\downarrow(E_F)} \times 100\%$$

ρ represent the density of states

For half-metallic materials, the conduction properties differ completely between minority and majority spin states, thus presenting a metallic property for one spin direction (non-zero density of states at the Fermi level) and a semiconducting or even insulating property for the other direction, and consequently a 100% spin polarization rate (**Figure 12**). That is, one of the two spin orientations do not contribute to conduction. This characteristic is called half-metallic ferromagnetism [7–9].

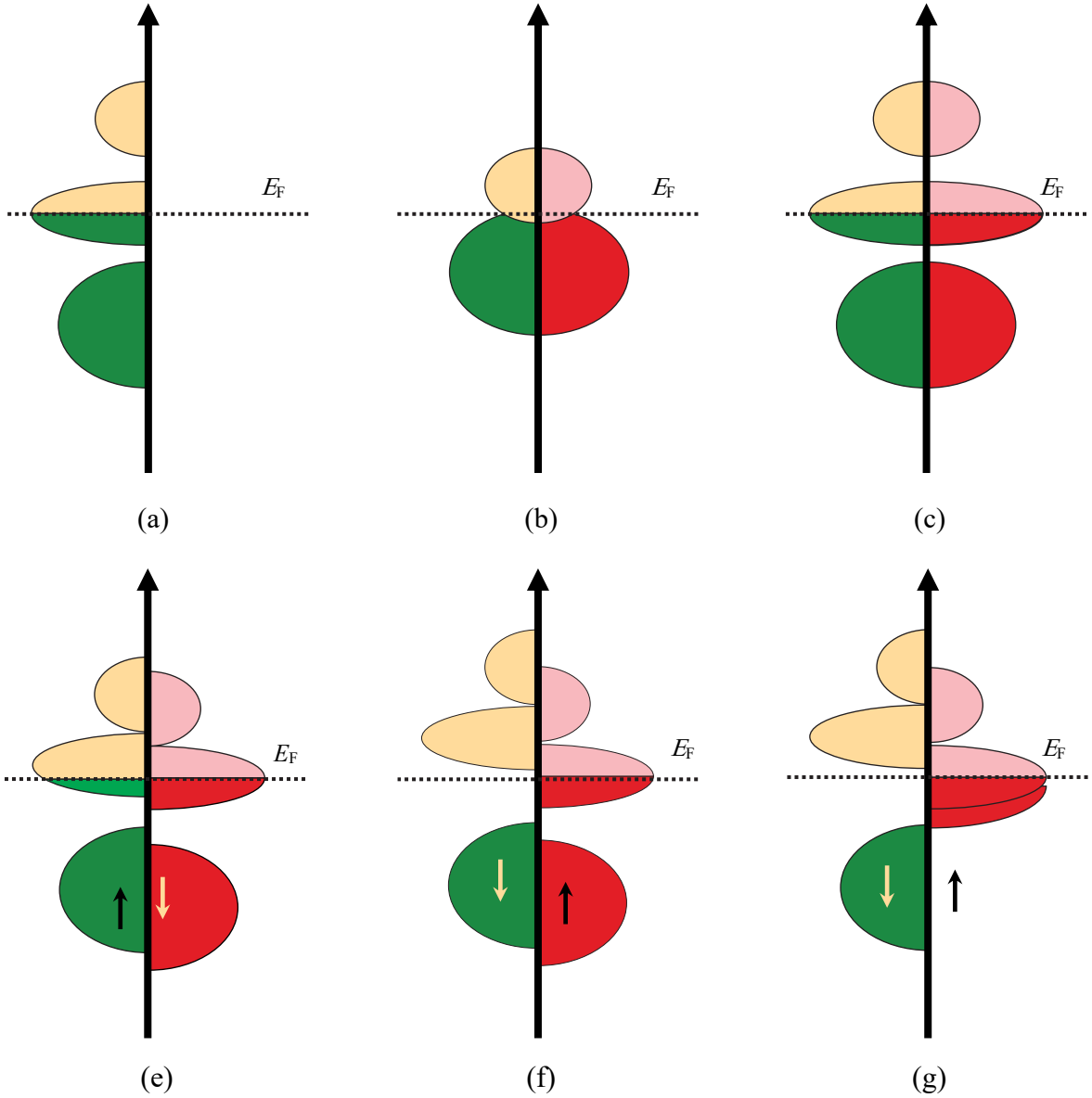


**Figure 11.** Schematic DOS curve (a) for a metal, (b) ferromagnet, (c) spin polarised metal, (e) ferromagnet, (f) half-metallic ferromagnet and (g) compensated half-metallic ferrimagnet, the band gap occurs in the minority DOS (left).

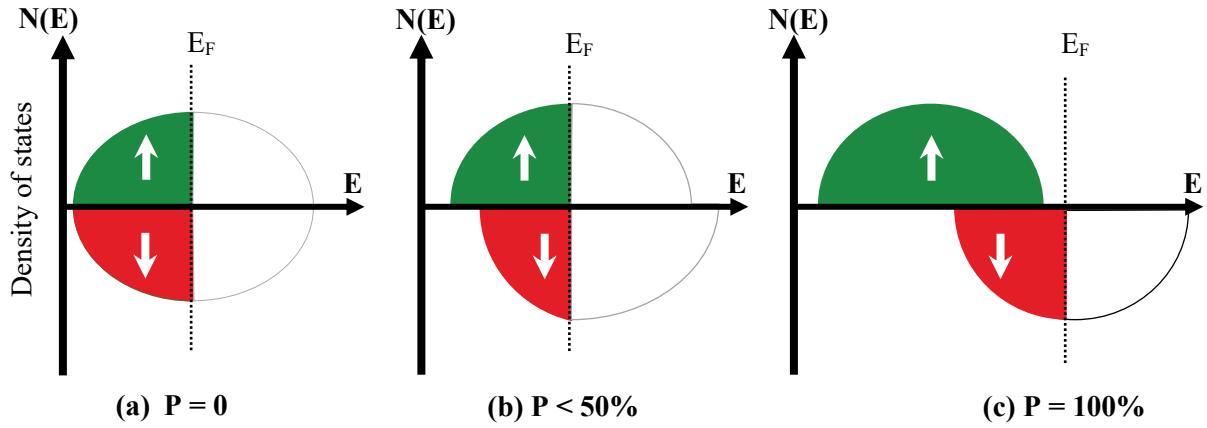


**Figure 12.** Schematic representation of a material's density of states and spin polarization: (a) non-ferromagnetic, (b) ferromagnetic, and (c) half-metallic ferromagnetic.

## I.7 Application of Heusler compounds:

The potential use of Heusler alloys for high-performance spintronics comes from its electronic and magnetic (Half-Metallic Ferromagnetism with nearly 100% spin polarisation High Curie Temperature, low Damping Constant, Low Coercivity, Slater-Pauling Behaviour)

Leveraging these strengths, Heusler alloys are applied in two primary domains:

- MRAM / Spin-RAM: Non-volatile, high-speed random access memory.
- HDD Sensors: High-sensitivity read heads for dense hard drives.
- Racetrack Memories: 3D domain-wall storage devices.
- GMR & TMR: Giant and Tunnel Magnetoresistance sensors.
- Spin Torque Transfer (STT): Energy-efficient writing mechanisms for memory.
- Spin Injection & Accumulation: Efficient spin transfer.
- Spin Resonance: High-frequency oscillators and signal processing.
- Spin Operation: General spin-based logic processing.

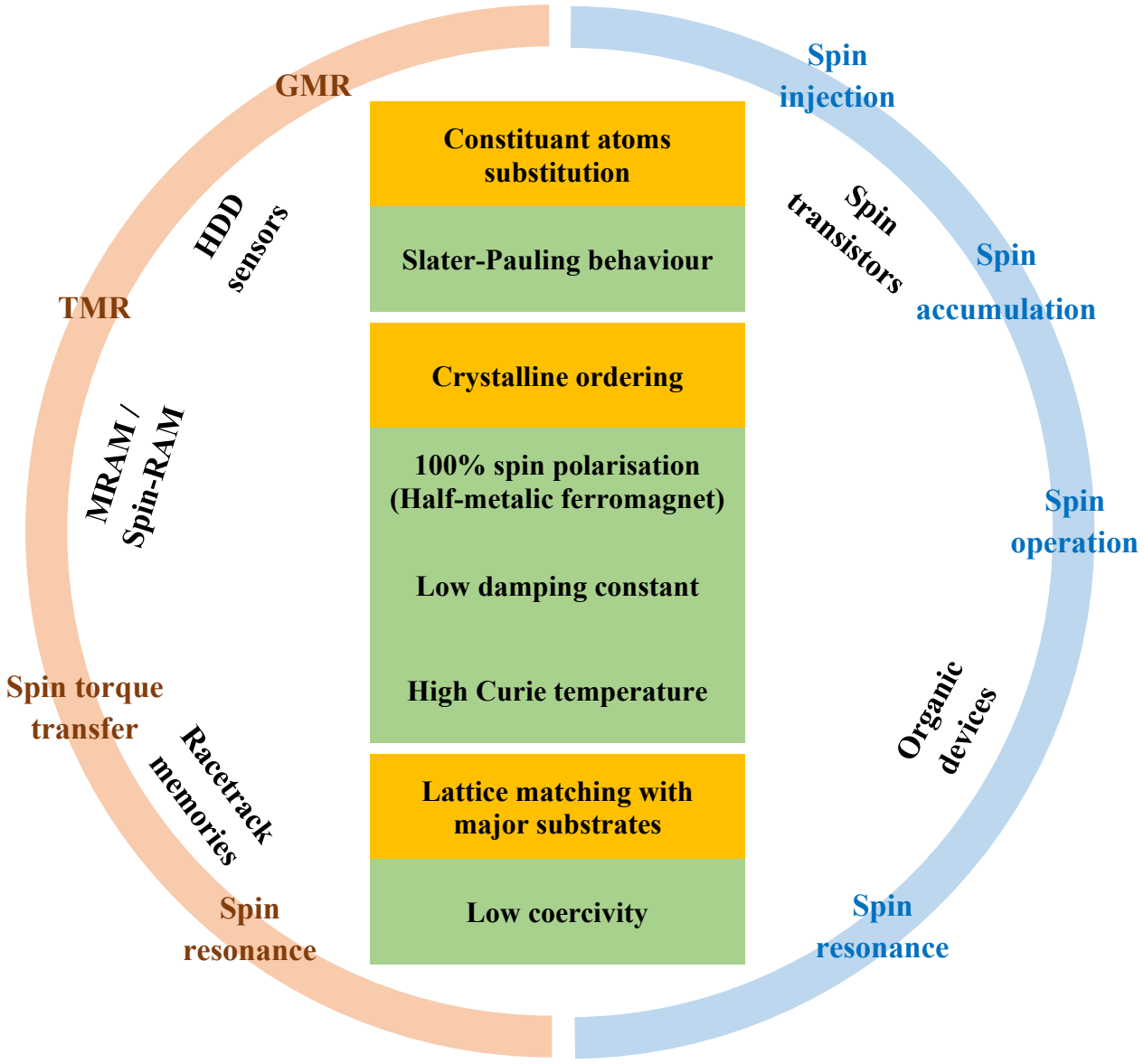


**Figure 13.** Applications of Heulser alloys

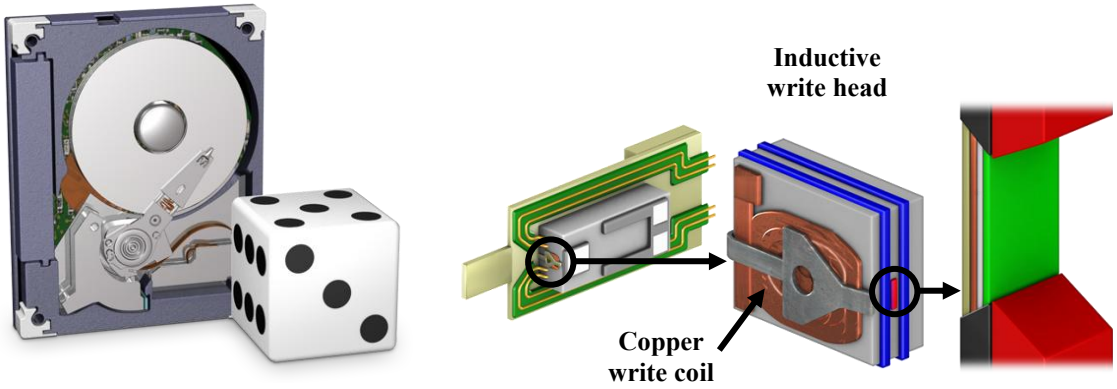


**Figure 14.** Hard drive GMR.

### I.7.1. Concept of spintronics:

spintronics, is a technique that exploits the quantum property of the electron's spin for the purpose of storing information. Spintronics can be described as a type of electronics that utilizes not only the charge but also an additional property: the spin of electrons. Spintronics emerged with the discovery of giant magnetoresistance (GMR) in 1988 by Albert Fert and Peter Grünberg (which would earn them the Nobel Prize in Physics in 2007), consisting of a succession of thin multilayers alternating between ferromagnetic and non-magnetic layers (for example, Fe/Cr or Co/Cu) [7, 8]. The general concept of spintronics is to place ferromagnetic materials in the path of electrons and to exploit the influence of spin on the mobility of electrons in these materials. This influence, first suggested by Mott in 1936, was later demonstrated experimentally and described theoretically in the late 1960s. The discovery of GMR opened up a field of possibilities for many other phenomena that also exploit the spin of electrons and which later proved to be very interesting and completely innovative. Today, spintronics is developing in many directions: tunnel magnetoresistance, spin-transfer phenomena, spintronics with semiconductors, molecular spintronics, spintronics with multiferroics.

### I.7.2. Spintronics Phenomena:

Giant Magnetoresistance (GMR): A phenomenon consisting of a switching of the electrical resistance of multilayers composed of an alternation of thin ferromagnetic and non-magnetic layers, depending on the configuration of the ferromagnetic layers magnetisations: either antiparallel, leading to a very high resistance, or parallel following the application of an external magnetic field, leading to the collapse of this resistance [7].

Tunnel Magnetoresistance (TMR): In physics, tunnel magnetoresistance is a property that appears in a tunnel junction. A tunnel junction, in its simplest form, is a thin insulating barrier between two conductive electrodes. The passage of current occurs by the tunnel effect through this barrier.

The electrical resistance to the current tunnelling from one material to another through the insulating layer then varies according to the relative orientation of the magnetization of the two layers. For a parallel alignment, the current will have a greater tendency to pass through the insulator, as the Tunnel effect is more probable[8, 9]. But when the magnetizations are

antiparallel, the resistance is then at its maximum. The application of a magnetic field allows the orientation of one layer's magnetization to be individually modified. Thus, one can switch from a maximum of resistance to a minimum.

## References:


1. Heusler, F.: Über magnetische Manganlegierungen. Verhandlungen der Deutschen Physikalischen Gesellschaft; German. 219–223 (1903)

2. Heusler, O.: Kristallstruktur und Ferromagnetismus der Mangan-Aluminium-Kupferlegierungen. Ann Phys. 411, 155–201 (1934). https://doi.org/10.1002/ANDP.19344110205

3. Bradley, A.J., Rodgers, J.W., Bradley, A.J., Rodgers, J.W.: The Crystal Structure of the Heusler Alloys. RSPSA. 144, 340–359 (1934). https://doi.org/10.1098/RSPA.1934.0053

4. Castelliz, L.: Eine ferromagnetische Phase im System Nickel-Mangan-Antimon. Monatsh Chem. 82, 1059–1085 (1951). https://doi.org/10.1007/BF00899384/METRICS

5. Castelliz, L.: Über eine mischkristallreihe zwischen zwei terären vertretern des C1-Typs. Monatsh Chem. 83, 1314–1317 (1952). https://doi.org/10.1007/BF00913833/METRICS

6. De Groot, R.A., Mueller, F.M., Engen, P.G.V., Buschow, K.H.J.: New class of materials: Half-metallic ferromagnets. Phys Rev Lett. 50, 2024–2027 (1983). https://doi.org/10.1103/PHYSREVLETT.50.2024

7. Žutić, I., Fabian, J., Sarma, S. Das: Spintronics: Fundamentals and applications. Rev Mod Phys. 76, 323–410 (2004). https://doi.org/10.1103/REVMODPHYS.76.323

8. Felser, C., Fecher, G.H., Balke, B.: Spintronics: A Challenge for Materials Science and Solid-State Chemistry. Angewandte Chemie International Edition. 46, 668–699 (2007). https://doi.org/10.1002/ANIE.200601815

9. Elphick, K., Frost, W., Samiepour, M., Kubota, T., Takanashi, K., Sukegawa, H., Mitani, S., Hirohata, A.: Heusler alloys for spintronic devices: review on recent development and future perspectives. Sci Technol Adv Mater. 22, 235–271 (2021). https://doi.org/10.1080/14686996.2020.1812364

10. Enamullah, Johnson, D.D., Suresh, K.G., Alam, A.: Half-metallic Co-based quaternary Heusler alloys for spintronics: Defect- and pressure-induced transitions and properties. Phys Rev B. 94, (2016). https://doi.org/10.1103/PhysRevB.94.184102

11. Rani, D., Bainsla, L., Suresh, K.G., Alam, A.: Experimental and Theoretical Investigation on the Possible Half-metallic Behaviour of Equiatomic Quaternary Heusler Alloys: CoRuMnGe and CoRuVZ (Z = Al, Ga). (2019). https://doi.org/10.1016/j.jmmm.2019.165662.

12. Felser, C., Wollmann, L., Chadov, S., Fecher, G.H., Parkin, S.S.P. (2016). Basics and Prospectives of Magnetic Heusler Compounds. In: Felser, C., Hirohata, A. (eds) Heusler Alloys. Springer Series in Materials Science, vol 222. Springer, Cham. https://doi.org/10.1007/978-3-319-21449-8_2.

13. Kirievsky, K., Gelbstein, Y., Fuks, D.: Phase separation and antisite defects iN the thermoelectric TiNiSn half-Heusler alloys. J Solid State Chem. 203, 247–254 (2013). https://doi.org/10.1016/j.jssc.2013.04.032

14. Bainsla, L., Suresh, K.G.: Equiatomic quaternary Heusler alloys: a material perspective for spintronic applications.

15. Wurmehl, S., Fecher, G.H., Kandpal, H.C., Ksenofontov, V., Felser, C., Lin, H.J., Morais, J.: Geometric, electronic, and magnetic structure of Co2FeSi: Curie temperature and magnetic moment measurements and calculations. Phys Rev B Condens Matter Mater Phys. 72, 184434 (2005). https://doi.org/10.1103/PHYSREVB.72.184434/FIGURES/9/THUMBNAIL

16. Sarvazad, K., Boochani, A., Zarghani, S. et al. Mechanical and thermodynamic stabilities, half-metallic and thermoelectric comparison between CoFeMnZ (Z = Si, Ge) Heuslers by DFT. Appl. Phys. A 127, 646 (2021). https://doi.org/10.1007/s00339-021-04779-0

17. Wei, X.P., Zhang, X., Shen, J., Chang, W.L., Tao, X.: Gilbert damping, electronic and magnetic properties for quaternary Heusler alloys CrYCoZ: First-principles and Monte Carlo studies. Comput Mater Sci. 210, (2022). https://doi.org/10.1016/j.commatsci.2022.111453

18. Abbassa, H., Labdelli, A., Meskine, S., Cherif, Y.B., Boukortt, A.: Half-metallic properties in Co2XSn (X = Ti, V and Cr) full-Heusler compound. https://doi.org/10.1142/S0217984920500281. 34, (2019). https://doi.org/10.1142/S0217984920500281

19. Latreche, L., Abbassa, H., Abbes, E.H., Boukortt, A.: First-Principles Investigation of the Influence of Disorder on Electronic and Magnetic Properties in CoFeMnAl Quaternary Heusler Alloys. Journal of Superconductivity and Novel Magnetism 2025 38:5. 38, 1–19 (2025). https://doi.org/10.1007/S10948-025-07048-W

20. Hilzinger, R., & Rodewald, W. (2013). Magnetic Materials: Fundamentals, Products, Properties, Applications.

21. J. M.D. Coey, Stuart S. Stuart, Handbook of Magnetism and Magnetic Materials: Volume 1,2, 1-2, 1 2021.

22. Tamayo, K. B. (2010). Magnetic Properties of Solids (Material Science and Technologies). Nova Science Publishers.

23. Dzyaloshinsky, I.: A thermodynamic theory of "weak" ferromagnetism of antiferromagnetics. Journal of Physics and Chemistry of Solids. 4, 241–255 (1958). https://doi.org/10.1016/0022-3697(58)90076-3

24. Rybakov, F.N., Borisov, A.B., Blügel, S.: Type II multiferroic order in two-dimensional transition metal halides from first principles spin-spiral calculations You may also like New spiral state and skyrmion lattice in 3D model of chiral magnets. (2023). https://doi.org/10.1088/2053-1583/acd4d0

25. Skyrme, T.H.R.: A unified field theory of mesons and baryons. Nuclear Physics. 31, 556–569 (1962). https://doi.org/10.1016/0029-5582(62)90775-7

26. Bogdanov, A. & Yablonskiui, D. (1989). Thermodynamically stable "vortices" in magnetically ordered crystals. The mixed state of magnets. Sov. Phys. JETP. 68. 101.

27. A. Bogdanov, A. Hubert, Thermodynamically stable magnetic vortex states in magnetic crystals, Journal of Magnetism and Magnetic Materials, Volume 138, Issue 3, 1994, https://doi.org/10.1016/0304-8853(94)90046-9.

28. Rößler, U.K., Bogdanov, A.N., Pfleiderer, C.: Spontaneous skyrmion ground states in magnetic metals. Nature 2006 442:7104. 442, 797–801 (2006). https://doi.org/10.1038/nature05056

29. Mühlbauer, S., Binz, B., Jonietz, F., Pfleiderer, C., Rosch, A., Neubauer, A., Georgii, R., Böni, P.: Skyrmion Lattice in a Chiral Magnet. (2024)

30. Yu, X.Z., Onose, Y., Kanazawa, N., Park, J.H., Han, J.H., Matsui, Y., Nagaosa, N., Tokura, Y.: Real-space observation of a two-dimensional skyrmion crystal. Nature. 465, 901–904 (2010). https://doi.org/10.1038/NATURE09124

# Chapter II : Defects in Solids

## II.1 Introduction to Defects in Solids

According to the principles of thermodynamics, it is challenging to produce a crystal with a perfect atomic structure at a specified temperature due to the opposing influences of ordering (enthalpy) and disorder (entropy) .

## II.2 Importance of Defects in Materials Science

Point defects are important because they influence many physical properties and are responsible for many diffusion-controlled processes. The mechanical properties of metals are particularly sensitive to the presence of point defects because of their strong interactions with dislocations [1],[2]. Diffusion processes, which are responsible for many solid-state reactions, are largely controlled by the migration characteristics of point defects, primarily vacancies. Thus, both the static and dynamic properties of point defects are of crucial importance in many areas of materials science.

## II.3 Classification of Defects

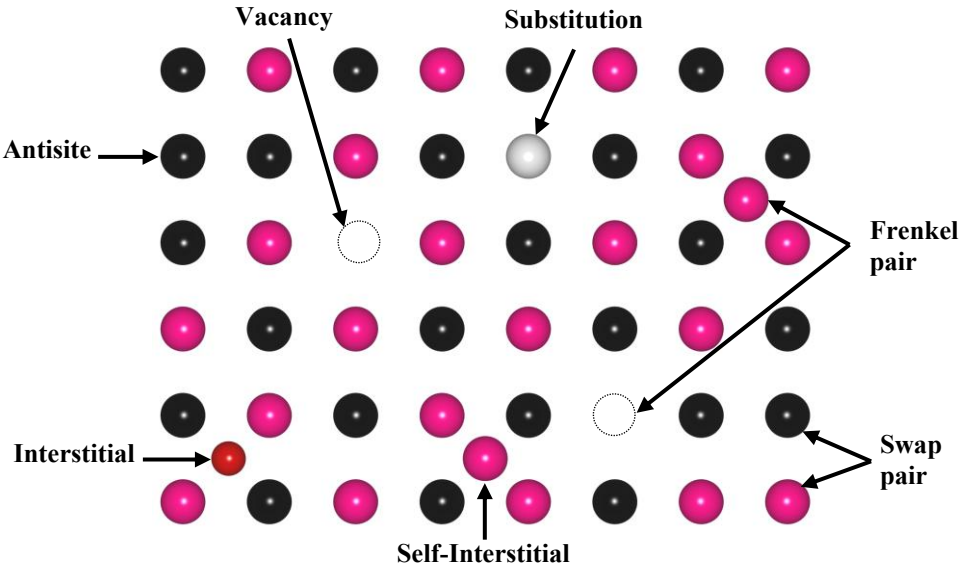


**Figure 15.** Different types of point defects.

## II.3.1. Point Defects

Point defects (zero-dimensional defects) are local imperfections in the crystal lattice that include one or two atoms and cause lattice disruption at a few atomic positions [3],[4]. Primary point defects are classified as vacancies, interstitials, and substitutions (**Figure 15**).

### *II.3.1.1. Vacancies:*

A vacancy is a missing atom at a regular lattice site. In a magnetic material, a vacancy removes a magnetic moment and, more importantly, breaks the exchange interaction pathways with its neighbouring atoms, which can lead to a local weakening or modification of the magnetic order [3],[5].

### *II.3.1.2. Interstitials*

An interstitial is formed when an atom occupies a site that is normally vacant in the perfect crystal... The number of available interstitial sites is generally larger than the number of vacancies. The formation energies of interstitials are generally so high, however, that their equilibrium concentration is negligible for all practical purposes.

### *II.3.1.3. Substitutional Defects*

Substitutional defects occur when an atom is discovered to replace a regular atomic site of a different atom; for example, impurity X substituting a Fe site in the CoFeMnAl lattice is denoted as $X_{Fe}$. If the X atom is from the same lattice, this type of defect is called antisite; for example, a Co atom occupying a Fe-site in a regular CoFeMnAl lattice is referred to as Co-antisite ($Co_{Fe}$). If the antisite defect is compensated; for instance, if there is a Co atom occupying a Fe-site while having at the same time a Fe atom occupying a Co-site in the crystal, this is known as a swap defect, and its noted CoFe [6],[7].

### *II.3.1.4. Swap Defects*

A swap defect (sometimes referred to as a "site exchange" or "site swap defect") occurs when two atoms exchange their positions within the lattice. The most common scenario is in a binary compound or alloy where an atom of type A at its designated lattice site exchanges places with an atom of type B at its respective site. This process results in both atoms occupying each other's original positions. Swap defects conserve both the overall composition and stoichiometry but disrupt the local chemical ordering.

### *II.3.1.5. Antisite Defect*

An antisite defect happens when an atom resides on a lattice site that is typically reserved for another element, but without a corresponding exchange. For instance, in a binary crystal AB, an antisite defect would be an A atom located on a B site, or vice versa, without the B atom necessarily occupying an A site in return [2],[7]-[8].

## II.3.2. The Kröger–Vink nomenclature :

Kröger–Vink nomenclature is a standardised notation used in solid-state/ceramic defect chemistry to describe point defects (vacancies, interstitials, and substitutional defects) and their effective charges relative to the perfect crystal lattice [4].

A defect is typically written as $X_Y^q$ : the species X occupying a site, the site Y being occupied, and the effective charge q relative to the ideal lattice. This convention is widely used for writing defect reactions and for constructing defect diagrams in ionic solids.

**Table 5:** Kröger–Vink notation for point defects in an ionic binary compound. The table lists notation for defects where X represents the atom forming the positive ion (cation) and Y represents the atom forming the negative ion (anion). Effective charges are denoted by dots (·) for positive, primes (′) for negative, and crosses (×) for neutral relative to the perfect lattice.

| **Sites** | **Notation** | **Sites** | **Notation** |
|---|---|---|---|
| $X^+$ on X site | $X_X^\times$ | $Y^-$ on Y site | $Y_Y^\times$ |
| Vacancy on X site | $V_X^{'}$ | Vacancy on Y site | $V_Y^{\bullet}$ |
| Interstitial X ion | $X_i^{\bullet}$ | Interstitial Y ion | $Y_i^{'}$ |
| Interstitial X atom | $X_i^\times$ | Interstitial Y atom | $Y_i^\times$ |
| Foreign ion $A^+$ on X site | $A_X^\times$ | Foreign ion $A^{2+}$ on $X^+$ site | $A_X^{\bullet}$ |
| Free electron | $e'$ | Free hole | $h^{\bullet}$ |

## II.4 Defects in Heusler alloys:

Various variants of the $L2_1$ structure can be formulated, if the X, Y, and/or Z atoms are intermixed on the respective crystallographic positions, leading to different (local) symmetries and structure types. In the following, we will describe the most common types of structures:

### II.4.1. Defected half-Heusler structures:

Various forms of atomic disorder can occur within the Half-Heusler structure. **Figure 16Error! Reference source not found.** illustrates an overview of potential disorder types. A mixture of atoms in Wyckoff positions 4a and 4b results in a CaF2-type structure (C1, space group $Fm\bar{3}m$, no 225). Conversely, the unoccupied sites may become partially filled, while simultaneously, vacancies emerge in the other sublattices.

**Table 6:** Site occupancy and general formula for different atomic order of half-Heusler compounds. The notations according to the Inorganic Crystal Structure Database (ICSD), the Strukturberichte (SB), the Pearson database, as well the space group are given.

| Site occupancy | Formula | ICSD | SB | Pearson | Space group |
|---|---|---|---|---|---|
| 4a, 4b, 4c | XYZ | LiAlSi (MgAgAs) | $C1_b$ | cF16 | $F\bar{4}3m$ (No. 216) |
| 4a = 4b, 4c | $XZ_2$ | $CaF_2$ | C1 | cF12 | $Fm\bar{3}m$(No. 225) |
| 4a, 4b, 4c = 4d | $X_2YZ$ | $Cu_2MnAl$ | $L2_1$ | cF16 | $Fm\bar{3}m$(No. 225) |
| 4a = 4b, 4c = 4d | XZ | CsCl | B2 | cP2 | $Pm\bar{3}m$(No. 221) |
| 4a = 4c, 4b = 4d | YZ | NaTl | B32a | cF16 | $Fd\bar{3}m$ (No. 227) |
| 4a = 4b = 4c = 4d | X | W | A2 | cI2 | $Im\bar{3}m$ (No. 229) |

Consequently, a partial occupation of the 4d sites, coupled with vacancies at the 4c sites, results in a Cu2MnAl-type structure (L21, space group $Fm\bar{3}m$, no. 225), while further intermixing of atoms at the 4a and 4b positions induces a CsCl-type disorder (B2, $Pm\bar{3}m$, no. 221). Conversely, if the unoccupied lattice site is partially filled by atoms from the 4b site, along with intermixing of the 4a and 4c positions, a NaTl-type structure is achieved

(B32a, $Fd\bar{3}m$ , no. 227). A wholly arbitrary distribution of the three atoms across the four available positions results in a tungsten-type disorder (W, $Im\bar{3}m$, no. 229). Table **6** presents a summary of various structural types and corresponding notations as per the Inorganic Crystal Structure Database (ICSD), Strukturberichte (SB), Pearson database, and space group classifications.

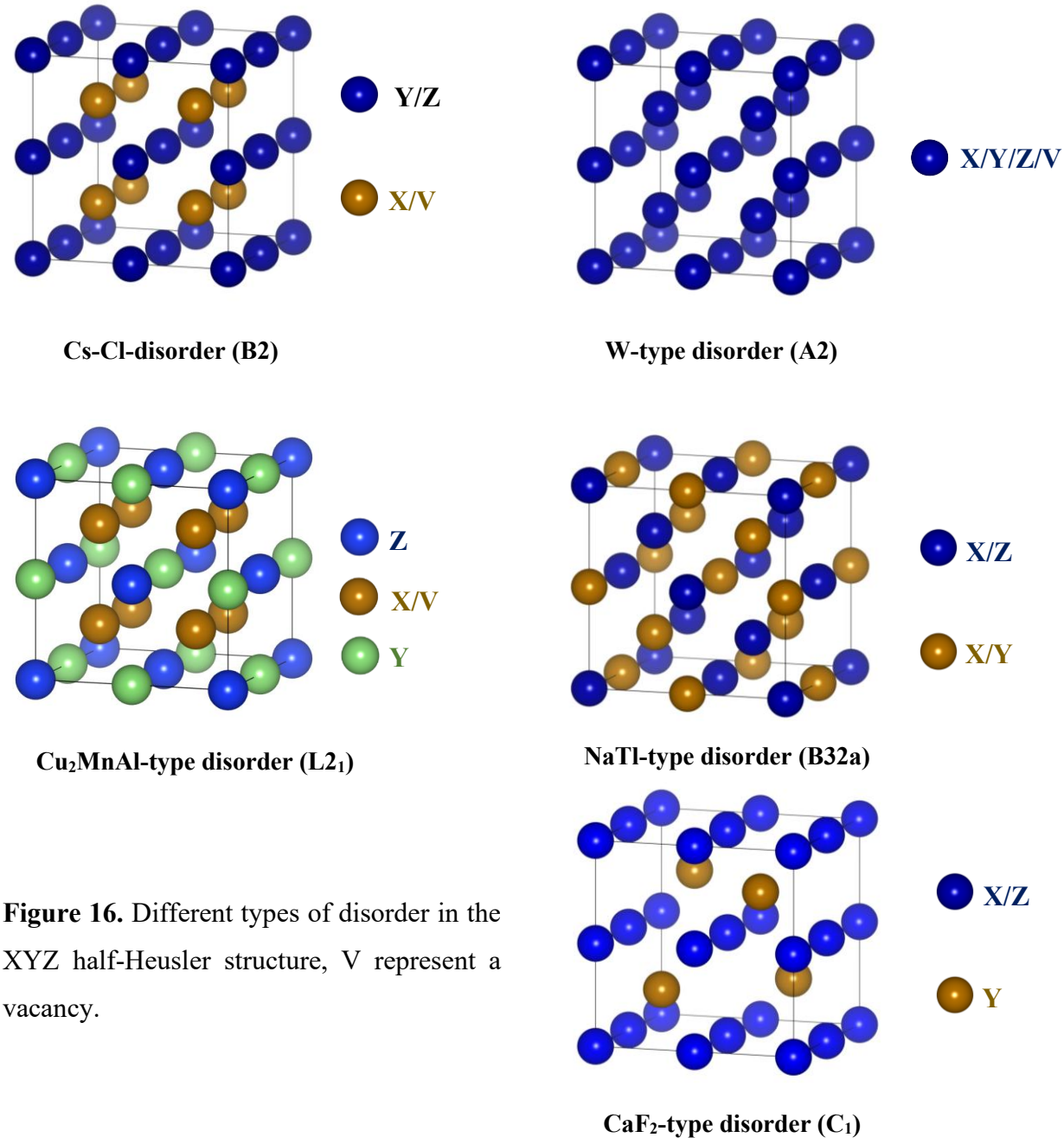


**Figure 16.** Different types of disorder in the XYZ half-Heusler structure, V represent a vacancy.

## II.4.2. Defected full-Heusler structures:

The properties of Heusler compounds, analogous to Half-Heusler materials, are significantly influenced by atomic arrangement. Band structure calculations indicate that even minimal disorder in the atomic distribution on lattice sites results in significant alterations to their electronic structure, subsequently affecting their magnetic and transport properties [5],[7],[9] Consequently, a meticulous examination of their crystal structure is imperative to comprehend the structure-property relationship of Heusler compounds. **Figure 17** illustrates the transition from ordered to the most prevalent disordered Heusler structures, which will be elucidated subsequently. [10]-[12] Should the Y and Z atoms be uniformly distributed, the 4a and 4b positions will be rendered equivalent. This results in a CsCl-type structure, referred to as B2-type disorder. Consequently, the symmetry diminishes, resulting in the space group $Pm\bar{3}m$. The random distribution of X and Y or X and Z results in a BiF3-type disorder (Space group no. 225: $Fm\bar{3}m$, $DO_3$).

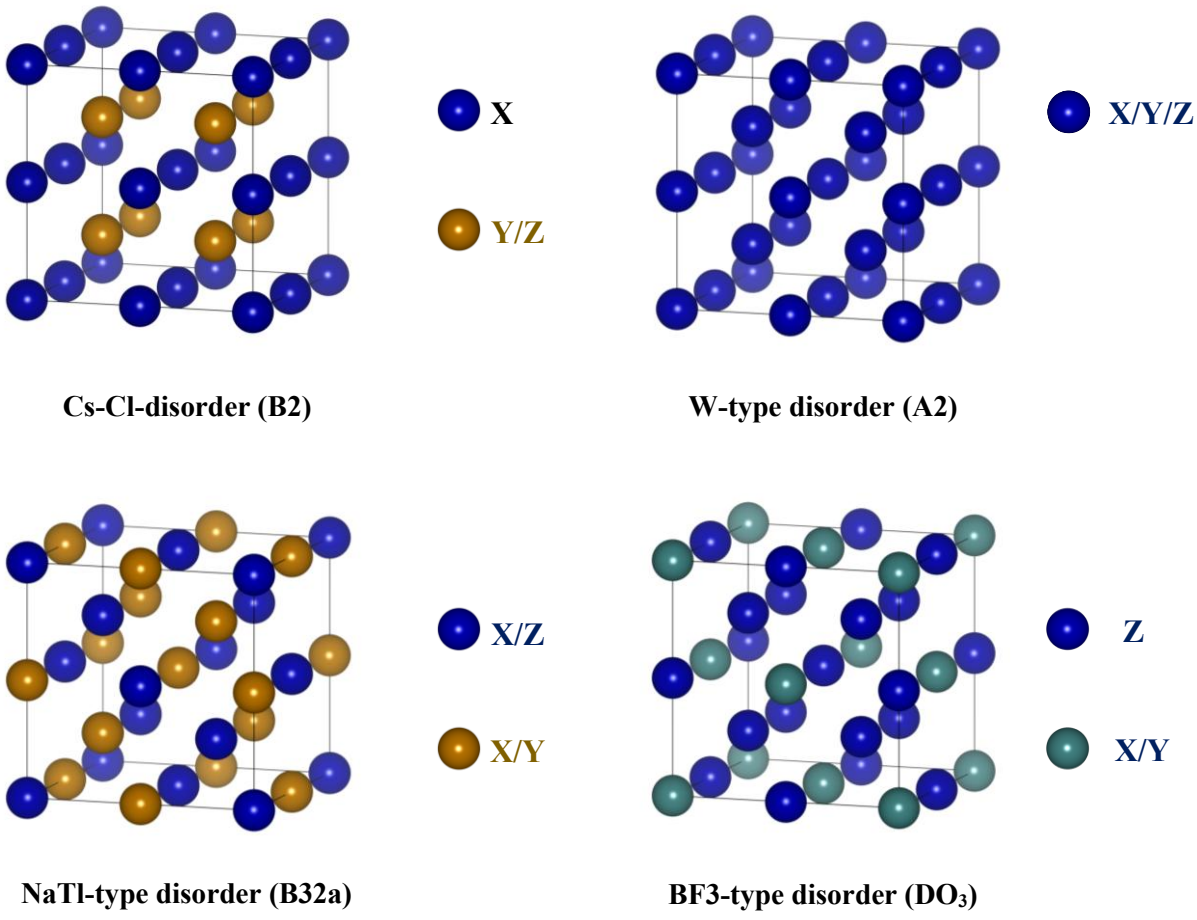


**Figure 17.** Different types of disorder for the Full Heusler structure.

In contrast to these types of disorders, the NaTl-type structure is infrequently observed. In this structural type, the X atoms sitting in one of the fcc sublattices are intermixed with the Y atoms, while the X atoms in the second sublattice are combined with the Z atoms.

**Table 7:** Site occupancy and general formula for different atomic order of Heusler compounds. The notations according to the Inorganic Crystal Structure Database (ICSD), the Strukturberichte (SB), the Pearson database, as well the space group are given.

| Occupancy | Formula | ICSD | SB | Pearson | Space group |
|---|---|---|---|---|---|
| X, X', Y, Z | XX'YZ | LiMgPdSn | Y | cF16 | $F4\bar{3}m$(No. 216) |
| X = X', Y, Z | $X_2YZ$ | $Cu_2MnAl$ | $L2_1$ | cF16 | $Fm\bar{3}m$(No. 225) |
| X, X' = Y, Z | $XX_2'Z$ | $CuHg_2Ti$ | X | cF16 | $F4\bar{3}m$(No. 216) |
| X = X' = Y, Z | $X_3Z$ | BiF3 | $DO_3$ | cF16 | $Fm\bar{3}m$(No. 225) |
| X = X', Y = Z | $X_2Y_2$ | CsCl | B2 | cP2 | $Pm\bar{3}m$(No. 221) |
| X = Y, X' = Z | $X_2X_2'$ | NaTl | B32a | cF16 | $Fd\bar{3}m$(No. 227) |
| X = X' = Y = Z | $X_4$ | W | A2 | cI2 | $Im\bar{3}m$(No. 229) |

This disorder is also referred to as B32a disorder (Space group number 227, $Fd\bar{3}m$ ). The X atoms occupy the Wyckoff position 8a (0, 0, 0), whereas Y and Z are randomly distributed at position 8b (1/2, 1/2, 1/2). Unlike these partial disorder phenomena, all positions in the tungsten-type structure with a body-centered cubic lattice and diminished symmetry ($Im\bar{3}m$(A2)) become equivalent [3], [11]. In contrast to these types of disorders, the NaTl-type structure is infrequently observed. In this structural type, the X atoms sitting in one of the fcc sublattices are intermixed with the Y atoms, while the X atoms in the second sublattice are combined with the Z atoms.

**In contrast** to these types of disorders, the NaTl-type structure is infrequently observed. In this structural type, the X atoms sitting in one of the fcc sublattices are intermixed with the Y atoms, while the X atoms in the second sublattice are combined with the Z atoms.

**Table 7** shows the various ordering variants of Heusler compounds. The site occupancy is associated with the relevant general formula. The various notations of crystal structures according to the Inorganic Crystal Structure Database (ICSD), Strukturberichte (SB), and Pearson database, along with the corresponding space group, are provided. All types of disorder present in the Heusler structure can also manifest in Half-Heusler compounds, where vacancies are statistically distributed across all positions. In the CaF2-type disorder, the vacant site is maintained. The values associated with t ("translationsgleich") and k ("klassengleich") denote the degree of symmetry reduction. It is important to note that there are two atoms per unit cell in both the tungsten-type and CsCl structures. For all other structural types, there are 16 atoms per unit cell due to the duplication of all cell axes.

## References:


[1] J. Herran, R. Dalal, P. Gray, P. Kharel, and P. V. Lukashev, "Atomic disorder induced modification of magnetization in MnCrVAl," *J Appl Phys*, vol. 122, no. 15, Oct. 2017, doi: 10.1063/1.4998308.

[2] P. Borgohain and M. B. Sahariah, "Effect of compositional and antisite disorder on the electronic and magnetic properties of Ni-Mn-In Heusler alloy," *Journal of Physics Condensed Matter*, vol. 27, no. 17, May 2015, doi: 10.1088/0953-8984/27/17/175502.

[3] D. A. (David A. ) Drabold and S. K. Estreicher, "Theory of defects in semiconductors," p. 295, 2007.

[4] R. J. D. Tilley, "Defects in Solids," *Encyclopedia of Inorganic and Bioinorganic Chemistry*, Sep. 2005, doi: 10.1002/9781119951438.EIBC0058.

[5] C. Freysoldt *et al.*, "First-principles calculations for point defects in solids," *Rev Mod Phys*, vol. 86, no. 1, pp. 253–305, Mar. 2014, doi: 10.1103/RevModPhys.86.253.

[6] C. S. Jiang, W. Peng, Z. Q. Liu, and X. Deng, "First-principles calculations for formation energy and magnetism of defect structures in Heusler alloys Mg-V-Z (Z = Al, Ga, In)," *Physica B Condens Matter*, vol. 600, Jan. 2021, doi: 10.1016/j.physb.2020.412388.

[7] B. Hamad and Q. M. Hu, "The effect of defects on the electronic and magnetic properties of Fe2MnSi Heusler alloy," *Phys Status Solidi B Basic Res*, vol. 248, no. 12, pp. 2893–2898, Dec. 2011, doi: 10.1002/pssb.201147305.

[8] K. Kirievsky, Y. Gelbstein, and D. Fuks, "Phase separation and antisite defects iN the thermoelectric TiNiSn half-Heusler alloys," *J Solid State Chem*, vol. 203, pp. 247–254, 2013, doi: 10.1016/j.jssc.2013.04.032.

[9] M. Arrigoni and G. K. H. Madsen, "A comparative first-principles investigation on the defect chemistry of TiO2 anatase," *Journal of Chemical Physics*, vol. 152, no. 4, Jan. 2020, doi: 10.1063/1.5138902.

[10] G. E. Bacon and J. S. Plant, “Magnetic order in the AuMn alloy derivatives Au2(Mn,Z) 2 where Z is Al, Cu, Ga, In or Zn,” *Journal of Physics F: Metal Physics*, vol. 3, no. 11, pp. 2003–2020, 1973, doi: 10.1088/0305-4608/3/11/020.

[11] T. Graf, C. Felser, and S. S. P. Parkin, “Simple rules for the understanding of Heusler compounds,” *Progress in Solid State Chemistry*, vol. 39, no. 1, pp. 1–50, May 2011, doi: 10.1016/J.PROGSOLIDSTCHEM.2011.02.001.

[12] L. Latreche, H. Abbassa, E. H. Abbes, and A. Boukortt, “First-Principles Investigation of the Influence of Disorder on Electronic and Magnetic Properties in CoFeMnAl Quaternary Heusler Alloys,” *Journal of Superconductivity and Novel Magnetism 2025 38:5*, vol. 38, no. 5, pp. 1–19, Sep. 2025, doi: 10.1007/S10948-025-07048-W.

# Chapter III : Results and discussions

In this chapter, we present and discuss the results of our first-principles investigations into the quaternary Heusler alloys **CoFeMnGe** and **CoFeMnAl**. The primary objective of this study is to elucidate the complex interplay between atomic ordering, electronic structure, and magnetic behaviour.

## III.1 Methodology:

Our first-principles calculations implemented two complementing techniques to calculate the properties of CoFeMnZ (Z = Ge and Al) alloys. We employed the WIEN2k ab initio simulation software, utilising density functional theory (DFT), for preliminary structural optimisations and analyses of disordered structures [1]-[4]. We utilised the Perdew-Burke-Ernzerhof (PBE) generalised gradient approximation (GGA) for the exchange-correlation interaction [5]. Initially, we constructed the ordered EQH alloys CoFeMnGe and CoFeMnAl and relaxed its geometry to identify the ground state. Then we employed the supercell approach for evaluating the disordered structure [18,19]. This requires building a large supercell from the ordered unit cell to integrate antisite and exchange defects at a specified concentration [6],[7]. To attain a 12.5% concentration, we built a 32-atom supercell of CoFeMnGe and CoFeMnAl from the relaxed unit cell. After that, we inserted antisite disorder by substituting one atom X with another Y (designated as YX antisite in Kröger–Vink nomenclature), and we simulated swap disorder by interchanging the locations of two randomly chosen atoms (designated as XY swap). Following that, we optimised these disordered structures to evaluate their total energy, together with their electronic and magnetic properties. The stability of the Twelve antisite and Six swap disordered structures has been evaluated relative to the ordered (ideal) CoFeMnZ EQH alloy. This comparison is primarily conducted by the computation of disordered formation energies, allowing the evaluation of the energetic favorability of each defect arrangement. Furthermore, we investigate the impact of these defects on the electronic and magnetic properties, clarifying their implications on half-metallicity and magnetism. For the calculations of the ordered structure, we assigned muffin-tin sphere radii of 2.20 a.u. for Co, Fe, Mn, and Ge, and 2.0 a.u. for Al. The cut-off parameter

RMTKmax is established at 9, utilising 3000 k-points across the whole Brillouin zone, with a separation energy selected at -6 Ry. The self-consistent field (SCF) convergence criteria were set at $10^{-4}$ Ry for energy and $10^{-3}$ e for charge. The dynamical and thermal stability was determined by phonons calculations using the Density functional perturbation theory (DFPT) method implemented in Phonopy package [8],[9], it involves creating a 2×2×2 supercell and calculating the force constants. Subsequently, we employed these force constants to compute the phonon dispersion curves and the phonon density of states. Furthermore, we acquired the exchange interaction parameters Jij of the CoFeMnZ alloys utilising the Munich SPRKKR algorithm [10] in accordance with the Vosko-Wilk-Nusair (VWN) approximation [11]. We employed the full-potential mode with an angular momentum cutoff of $l_{max} = 3$ on a 250 k-point mesh.We used the Monte Carlo method to simulate the Curie temperature. We created a 12 × 12 × 12 supercell for the calculations, utilising 10,000 equilibrium steps and the Hinzke–Nowak algorithm within the Vampire package [12] to estimate the magnetisation at each temperature.

## III.2 Investigation of ideal CoFeMnZ (Z = Ge, Al) structures:

### III.2.1. Structural Properties

In order to identify the ground state of the ordered CoFeMnGe and CoFeMnAl compounds, we have primarily investigated the variation of total energies versus the lattice parameter for the three types. The results we obtained indicate that Type I has a lower total energy for booth compound **Figure 18** and **Figure 19**. Next, we have investigated the following magnetic orders: non-magnetic (NM), ferromagnetic (FM), and anti-ferromagnetic (AFM), as shown in (Figure 10) and (Figure 12). Based on these results, it can be concluded that the ferromagnetic state is the most favourited for both investigated materials.

electronic, and magnetic properties for this compound are conducted solely on Type I FM structure.

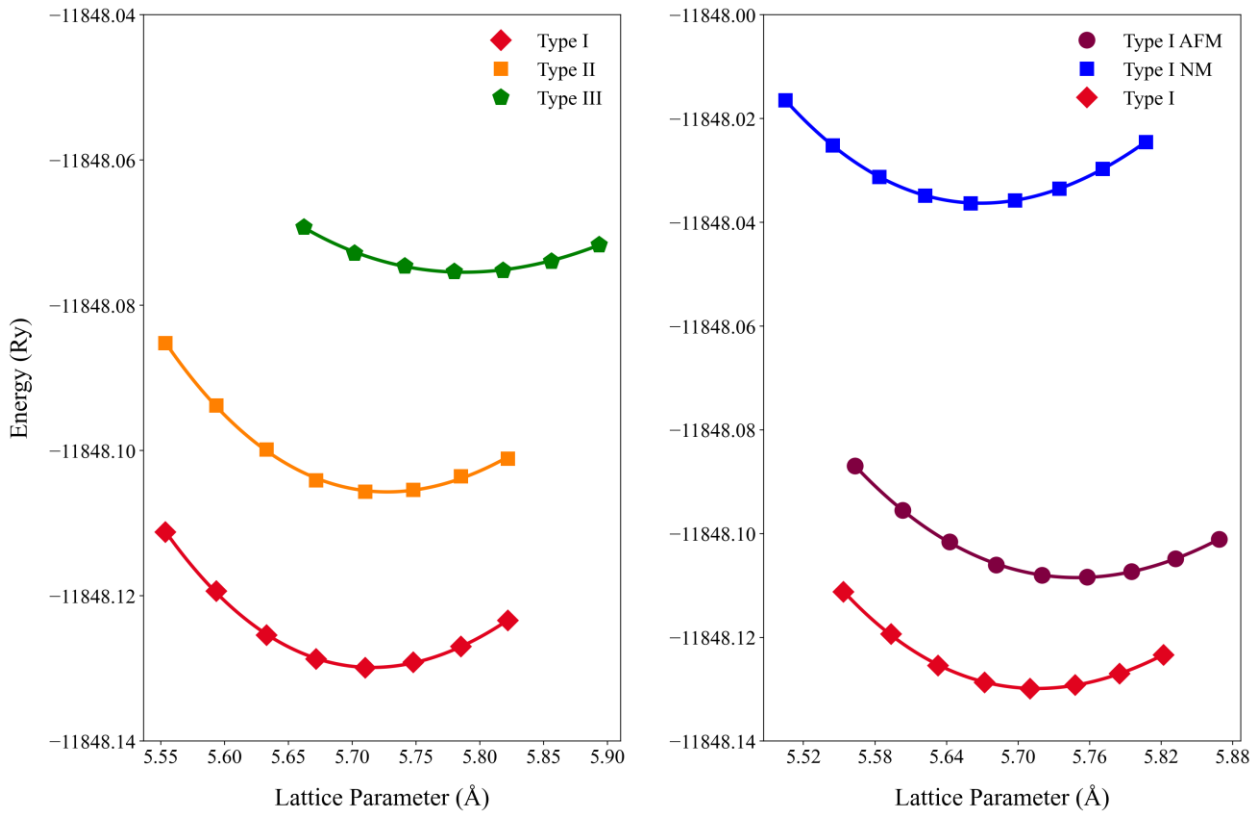


**Figure 18.** Total energies E versus lattice parameter for CoFeMnGe Heusler alloy: (a) for Type I, Type II and Type III structures in ferromagnetic (FM) order, (b) for different magnetic orders in type I.

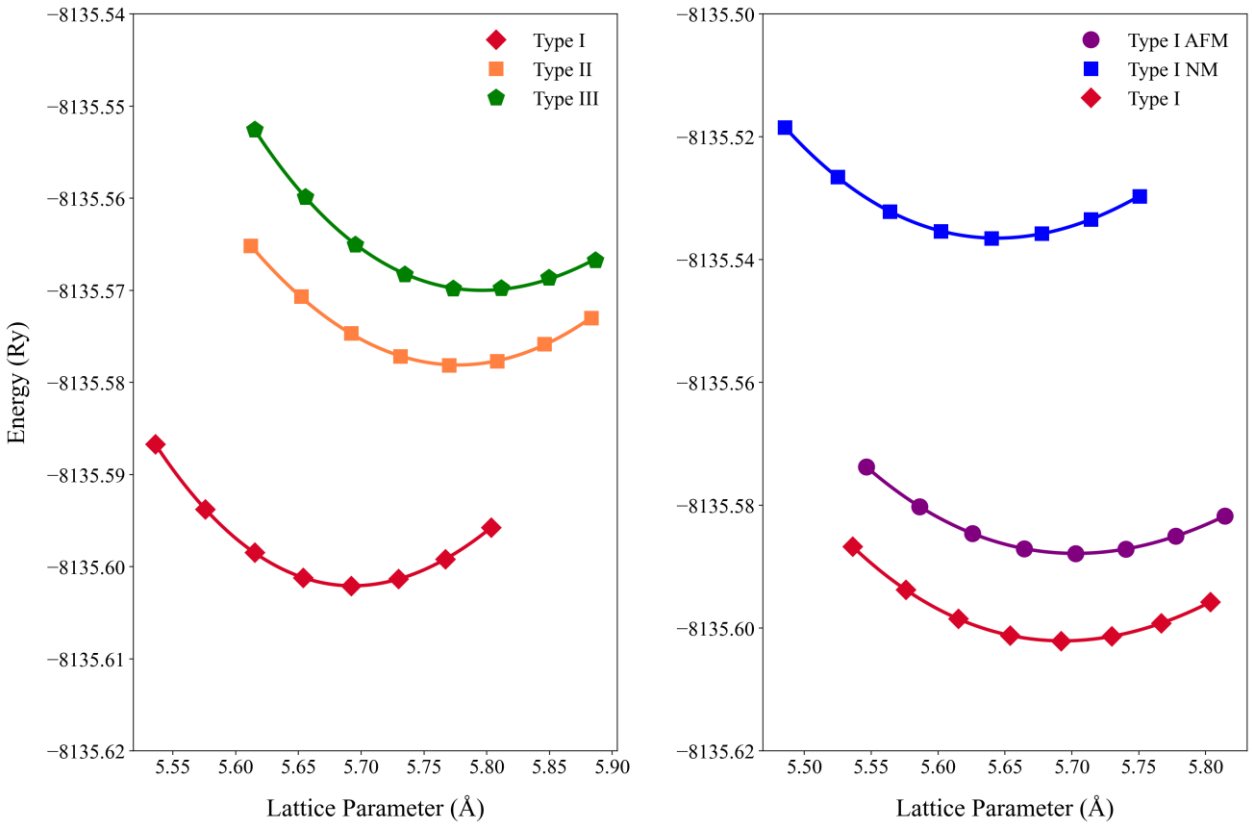


**Figure 19.** Total energies E versus lattice parameter for CoFeMnAl Heusler alloy: (a) for Type I, Type II and Type III structures in ferromagnetic (FM) order, (b) for different magnetic orders in type I.

The ground state for the studied compound was determined using the non-linear fitting Murnaghan's equation of state [13].

$$E(V) = E(V_0) - \frac{BV_0}{B' - 1} + \frac{BV}{B'}\left[\frac{\left(\frac{V_0}{V}\right)^{B'}}{B' - 1} + 1\right] \quad (1)$$

The formation energy for each structure is determined using the equation (2) provided from reference [14]:

$$E_f = E_{Total}^{CoFeMnZ} - (E_{Co}^{Bulk} + E_{Fe}^{Bulk} + E_{Mn}^{Bulk} + E_Z^{Bulk}) \quad (2)$$

$E_{Total}^{CoFeMnZ}$ represents the total energy of the compound, incorporating $E_{Co}^{Bulk}$, $E_{Fe}^{Bulk}$, $E_{Mn}^{Bulk}$, $E_Z^{Bulk}$.The bulk values denote the chemical potentials of the respective pure component elements (Co, Fe, Mn, and Z (Ge or Al) within their stable bulk reference structures. The

Hexagonal Close-Packed (HCP) structure is observed in Cobalt (Co), while Iron (Fe, or α-Fe) and Manganese (Mn) exhibit a Body-Centered Cubic (BCC) structure. Germanium (Ge) have a Cubic-Diamond (CD) structure (α-Ge) and Aluminium (Al) is characterised by a Face-Centered Cubic (FCC) crystal structure. The calculated lattice parameters and formation energies ($E_f$) presented in Table 2 align well with existing theoretical and experimental values. For booth compound the Type I FM structure is the easiest to synthesise due to its low formation energy. All the following calculations of the elastic,

**Table 8:** Structural parameters, the lattice parameter a in (Å), bulk modulus B in (GPa) and its first pressure derivative B', total energy E in (Ry) and formation energy Ef in (eV) for CoFeMnGe and CoFeMnAl in the three cubic types.

| | Y - Type | | ***a*** | ***B*** | ***B'*** | ***E*** | $\mathbf{E}_f$ |
|---|---|---|---|---|---|---|---|
| CoFeMnGe | Type I $^{FM}$ | This work | 5.71 | 214.659 | 4.444 | -11848.1272 | -22.34 |
| | | Other work[12] | 5.71 | | | | |
| | | Experimental[12] | 5.75 | | | | |
| | Type I $^{NM}$ | This work | 5.75 | 187.629 | 4.236 | -11848.1085 | -22.17 |
| | Type I $^{AFM}$ | This work | 5.67 | 228.141 | 4.445 | -11848.0363 | -21.19 |
| | Type II $^{FM}$ | This work | 5.73 | 196.700 | 5.863 | -11848.1057 | -22.13 |
| | Type III $^{FM}$ | This work | 5.79 | 119.505 | 4.918 | -11848.0754 | -21.72 |
| CoFeMnAl | Type I $^{FM}$ | This work | 5.69 | 189.539 | 4.819 | -8135.6021 | -5.63 |
| | | Other work[12] | 5.69 | | | -8135.6022 | -5.63 |
| | | Experimental[12] | 5.78 | | | | |
| | Type I $^{NM}$ | | 5.64 | 221.290 | 4.751 | -8135.5365 | -4.73 |
| | Type I $^{AFM}$ | | 5.70 | 177.747 | 4.540 | -8135.5878 | -5.43 |
| | Type II $^{FM}$ | | 5.70 | 209.728 | 4.597 | -8135.5804 | -5.33 |
| | Type III $^{FM}$ | | 5.79 | 157.675 | 4.984 | -8135.5708 | -5.20 |

## III.2.2. Elasticity, mechanical and dynamical properties

Elastic properties are crucial as they establish connections between the mechanical and dynamical properties of materials, which can be analysed through equilibrium total energy calculations [10]. They provide information on stability and offer critical insights into anisotropic properties, binding features, mechanical stability, and elasticity. The elastic constants Cij have been calculated to evaluate the mechanical stability of the cubic

structure. The elastic constants were determined by applying isotropic, tetragonal, and rhombohedral strains to the optimised cubic primitive cell. The quaternary Heusler alloys CoFeMnGe and CoFeMnAl possess a cubic structure, resulting in three independent elastic constants: $C_{11}$, $C_{12}$, and $C_{44}$. Its mechanical stability is confirmed by the criteria of Born-Huang [15],[16]:

$$C_{11} + 2C_{12} > 0, C_{44} > 0, \text{and } C_{11} - C_{12} > 0 \qquad (3)$$

The elastic properties are derived from the elastic constants, specifically the bulk modulus B, shear modulus G, Young's modulus E, and anisotropy factor Ae, utilising the following equations [14],[17]:

$$B = \frac{C_{11} + 2C_{12}}{3} \qquad (4)$$

$$G = \frac{G_V + G_R}{2} \qquad (5)$$

$G_V$ and $G_R$ are the Voigt and Reuss shear modulus, respectively.

$$G_V = \frac{C_{11} - C_{12} + 3C_{44}}{5} \qquad (6)$$

$$G_R = \frac{5C_{44}(C_{11} - C_{12})}{4C_{44} + (C_{11} - C_{12})} \qquad (7)$$

$$E = \frac{9BG}{3B + G} \qquad (8)$$

where the bulk modulus $B$ represents the compressibility of the compound

$$A = \frac{2C_{44}}{C_{11} - C_{12}} \qquad (9)$$

The Poisson's ratio σ, density $\rho$, longitudinal elastic wave velocities $v_l$, average sound velocity $v_m$, transverse elastic wave velocities $v_t$, average acoustic velocity $v_m$ and Debye temperature $\theta_D$ are next obtained using the following equations [17],[18]:

$$\sigma = \frac{3B - 2G}{2(3B + G)} \tag{10}$$

$$v_l = \frac{3B - 2G}{2(3B + G)} \tag{11}$$

$$v_t = \left(\frac{G}{\rho}\right)^{1/2} \tag{12}$$

$$v_m = \left[\frac{1}{3}\left(\frac{2}{v_t^3} + \frac{1}{v_l^3}\right)\right]^{-1/3} \tag{13}$$

$$\theta_D = \frac{h}{k_B}\left(\frac{3n}{4\pi}\frac{\rho}{M}\right)^{1/3} v_m \tag{14}$$

The calculated elastic constants are shown in Table 3. The bulk modulus (B) of CoFeMnGe is 204.80 GPa, which suggests a significant resistance to compression, surpassing that of CoFeMnAl 184.06 GPa. The Young's modulus (E) of 227.23 GPa for CoFeMnGe indicates superior stiffness relative to CoFeMnAl, which possesses an E value of 192.22 GPa. Poisson's ratio (v) is defined as the ratio of lateral contraction to axial elongation. The Poisson's ratios for CoFeMnGe and CoFeMnAl are 0.315 and 0.308, respectively. Since both values exceed 0.25 and are associated with a positive Cauchy pressure, a metallic bonding characteristic is suggested.

**Table 9:** Pressure P in (GPa) All values of the elastic constants $C_{11}$, $C_{12}$ and $C_{44}$ (in GPa), shear modulus G (in GPa), Young modulus E (in GPa), B/G ratio and Zener anisotropy factor $A_e$ for CoFeMnAl quaternary Heusler alloy.

| Compound | | ***P*** | $C_{11}$ | $C_{12}$ | $C_{44}$ | ***B*** | ***G*** | ***E*** | ***B/G*** | $A_e$ |
|---|---|---|---|---|---|---|---|---|---|---|
| **CoFeMnGe** | This work | 0 | 262.96 | 175.72 | 136.14 | 204.80 | 86.39 | 227.23 | 2.37 | 3.12 |
| | This work | 28.35 | 440.44 | 319.55 | 232.31 | 359.85 | 136.13 | 362.65 | 2.64 | 3.84 |
| | Other [19] | 0 | 263.00 | 178.00 | 156.00 | 206.00 | | | | 3.50 |
| **CoFeMnAl** | This work | 0 | 226.74 | 190.50 | 167.28 | 184.06 | 73.29 | 196.22 | 2.76 | 9.23 |
| | Other [21] | 0 | 212.00 | 178.00 | 167.00 | 189.00 | | | | 9.70 |

The Zener anisotropy factor ($A_e$) for CoFeMnAl is 9.23, markedly higher than the value of 3.12 for CoFeMnGe. This indicates an increased elastic anisotropy in CoFeMnAl. The ductility or brittleness of a solid is assessed using Pugh's ratio (B/G). According to Pugh's criteria specify that for ductile materials, the ratio of bulk modulus to shear modulus must exceed 1.75. The calculated ratio is 2.37 and 2.27 for CoFeMnGe and CoFeMnAl respectively, classifying both materials as ductile.

**Table 10:** Calculated Poisson's ratio σ, density ρ (in g.cm$^{-1}$), longitudinal elastic wave velocities $v_l$ (in m/s), transverse elastic wave velocities $v_t$ (in m/s), average acoustic velocity $v_m$ (in m/s) and Debye temperature $\theta_D$ (in K) for CoFeMnAl Heusler alloy.

| Compound | | ***P*** | ***σ*** | ***ρ*** | ***$v_l$*** | ***$v_t$*** | ***$v_m$*** | ***$\theta_D$*** |
|---|---|---|---|---|---|---|---|---|
| **CoFeMnGe** | This work | 0 | 0.315 | 8.62 | 6092 | 3165 | 3542 | 465.0 |
| | This work | 28.35 | 0.332 | 8.64 | 8144 | 3968 | 4436 | 592.0 |
| **CoFeMnAl** | This work | 0 | 0.308 | 7.06 | 6432 | 3389 | 3790 | 499.0 |
| | Other calc [20] | 0 | 0.340 | 7.08 | 6512 | 3217 | 3611 | 599.5 |

The phonon spectrum of CoFeMnGe and CoFeMnAl illustrated in Figure. 3 reveals dynamical stability, confirmed by the absence of imaginary (negative) phonon frequencies, suggesting that the ordered structure of both compounds is dynamically stable and is insensitive to spontaneous distortion or phase transition at low temperatures.

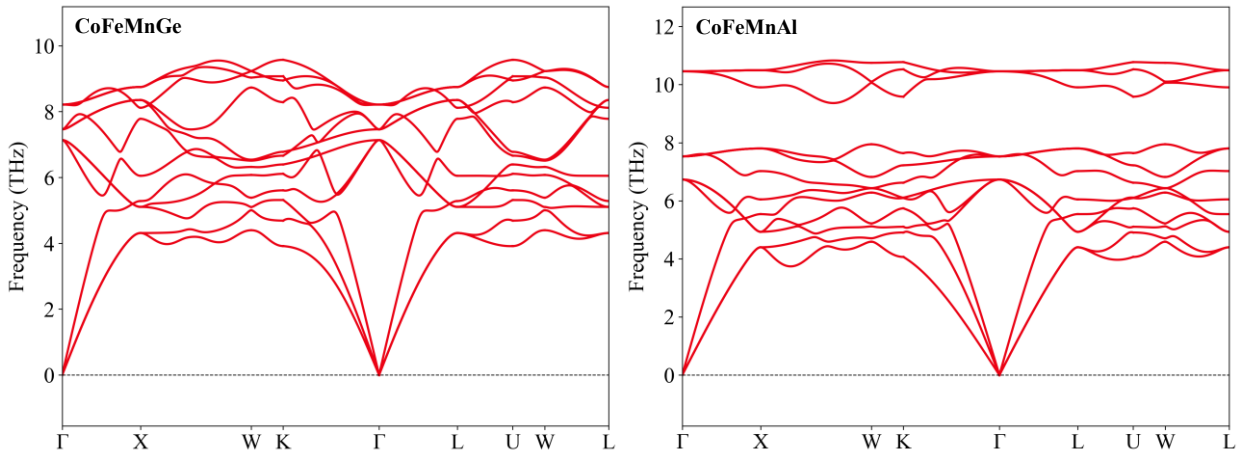


**Figure 20.** Calculated phonons spectrums.

### III.2.3. Electronic Properties:

The electronic structure of a material is an essential tool for determining its range of applications. The presence of the energy gap in the band structure of such a material plays a significant role in spintronic, thermoelectric, and shape-memory devices. Information about the band structure and density of states is crucial for examining the electronic properties of the studied compound. Electronic properties are often analysed through the band structures and densities of states, which depend primarily on the electronic distribution in both the valence and conduction bands and sometimes on the size of the energy gap. These properties help us analyses and understand the nature of the bonds formed between each element in the material, as well as its behaviour.

In this subsection, we offer additional details about the electronic properties of the CoFeMnAl and CoFeMnGe compounds in their stable phases by calculating the densities of states (TDOS and PDOS) and the band structure (BS) for both spin-up and spin-down electrons using the GGA approximation. The electronic valence states considered are 4s/3d for Co, Fe, and Mn; 3s/3p for Al; and 4s/4p for Ge. For the CoFeMnAl compound, the graphical representations of the TDOS and the BS functions are given in **Figure 24**. We observe a 0.62 eV gap near the Fermi level in the minority spin states, which indicates that CoFeMnAl exhibits half-metallic behaviour. Specifically, for the minority spin states, the valence band maximum ($V_{BM}$), primarily composed of hybridised d-states from Co, Fe, and Mn, is observed to be located below the Fermi level. The conduction band minimum ($C_{BM}$), consisting of unoccupied d-states, is situated above the Fermi level ($E_F$), thereby confirming the presence of an energy gap. This specific electronic configuration primarily arises from the ordered Heusler lattice's crystal field effects and resulting interatomic covalent bonding, which allow electron hybridisation and d-state splitting. As evidenced in the partial density of states (PDOS) (**Figure 25**), the d-orbitals of Co, Fe, and Mn undergo characteristic splitting into $t_{2g}$ and $e_g$ components. The dominant orbital splitting and hybridisation are fundamentally responsible for pushing the minority spin states away from the Fermi level, thereby creating the requisite band gap for high spin polarisation and establishing the compound's half-metallic ferromagnetic properties. A similar analysis of the CoFeMnGe compound at its equilibrium lattice parameter (5.72 Å) (**Figure 21**) and (**Figure 22**) reveals a more complex behaviour. While a significant reduction in the density of states is observed

in the minority spin channel around the Fermi level, the valence band maximum is positioned slightly above $E_F$. This feature characterises CoFeMnGe as nearly half-metallic, as it implies a small but non-zero density of states at the Fermi level that prevents complete spin polarisation. Given this nearly half-metallic nature, we investigated the effect of hydrostatic pressure on the material. The calculations demonstrate a pressure-induced transition to a complete half-metallic state. At a compressed lattice parameter of 5.43 Å, the valence band maximum is pushed below the Fermi level, opening a clean gap in the minority channel. Using the Birch-Murnaghan equation of state, the pressure required to induce this transition is estimated to be approximately 28.35 GPa. The stable behaviour of the integer magnetic moment across this transition offers strong evidence for pressure-induced half-metallicity, highlighting an effective approach to manipulating the spintronic properties of CoFeMnGe via pressure.

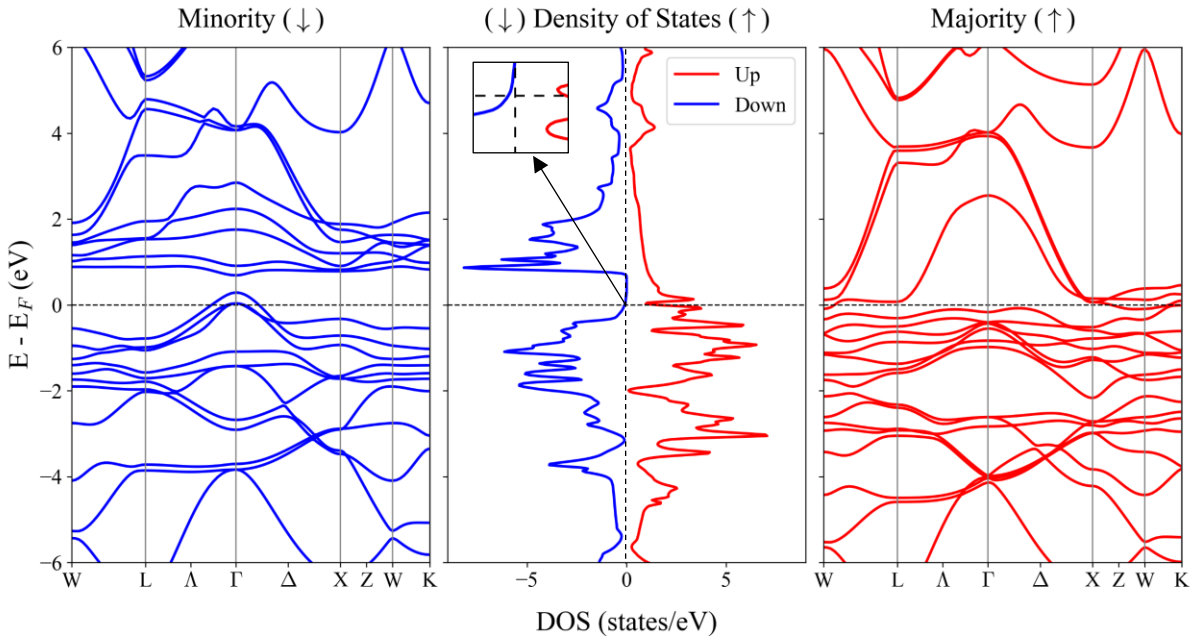


**Figure 21.** The band structure of spin-down electrons (left panel), spin-up electrons (right panel) and total densities of states (middle panel) for CoFeMnGe quaternary Heusler alloy.

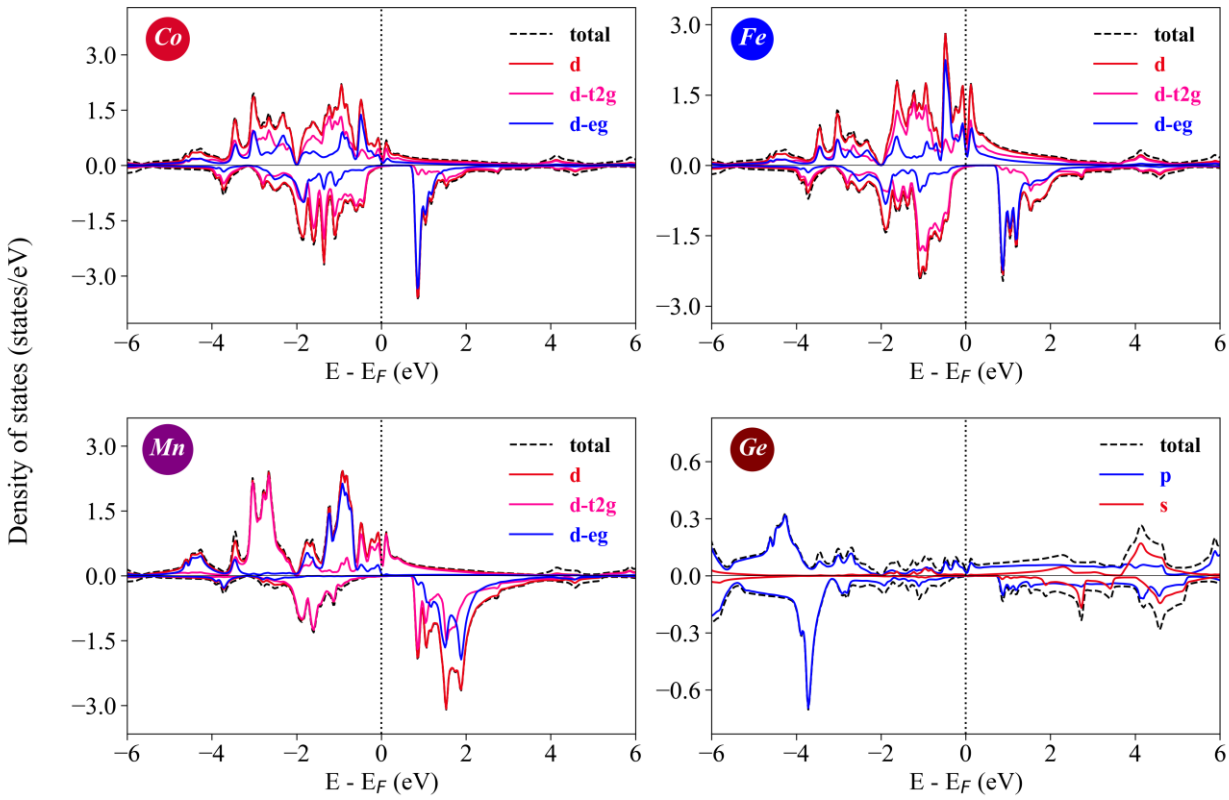


**Figure 22.** Partial density of states for atoms and orbitals for CoFeMnGe compound.

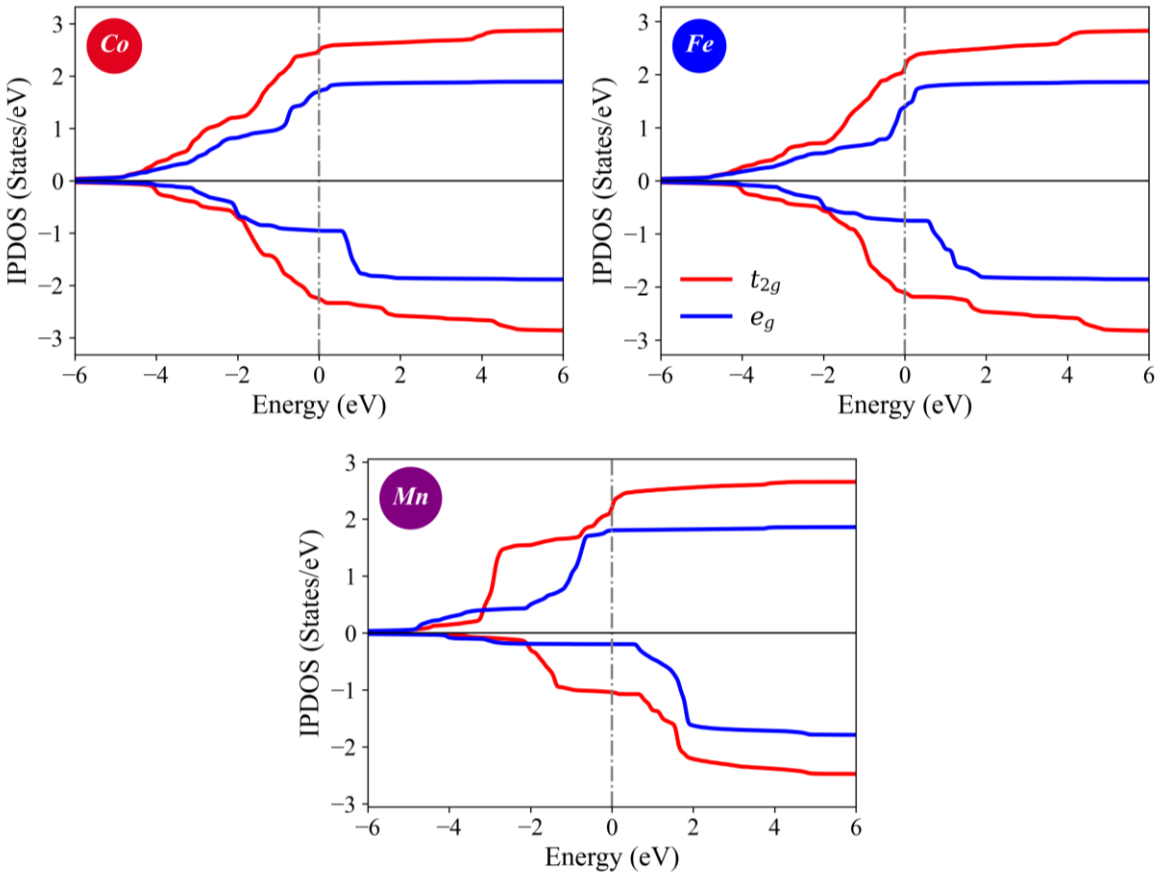


**Figure 23.** The IPDOS of Co-d, Fe-d and Mn-d orbitals for CoFeMnGe.

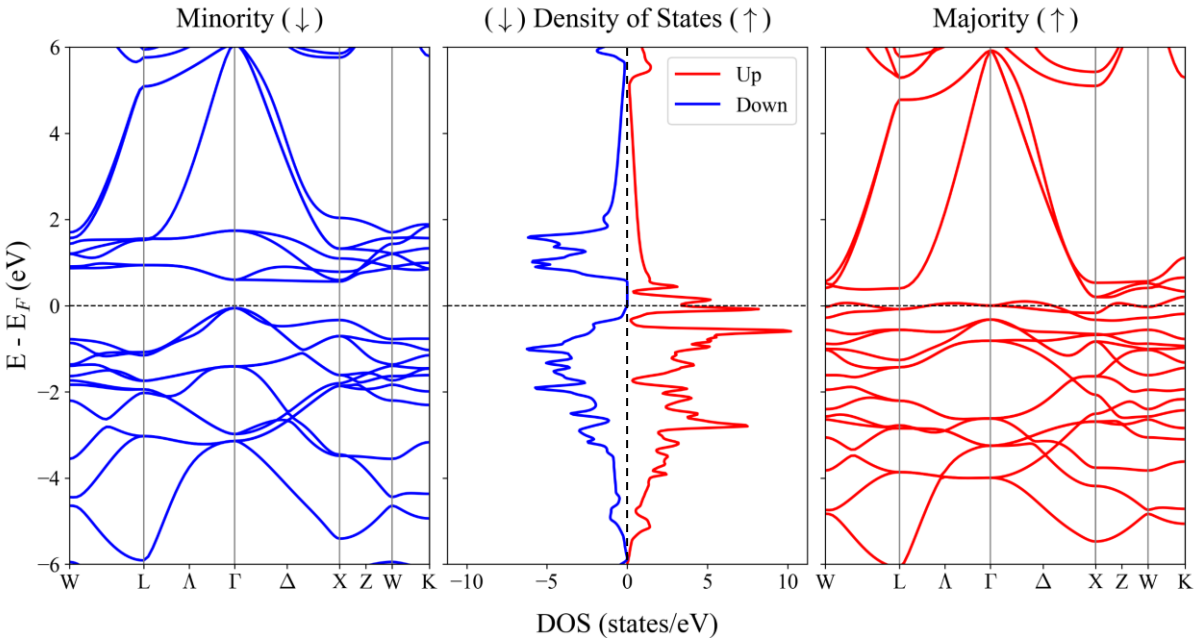


**Figure 24.** The band structure of spin-down electrons (left panel), spin-up electrons (right panel) and total densities of states (middle panel) for CoFeMnAl quaternary Heusler alloy.

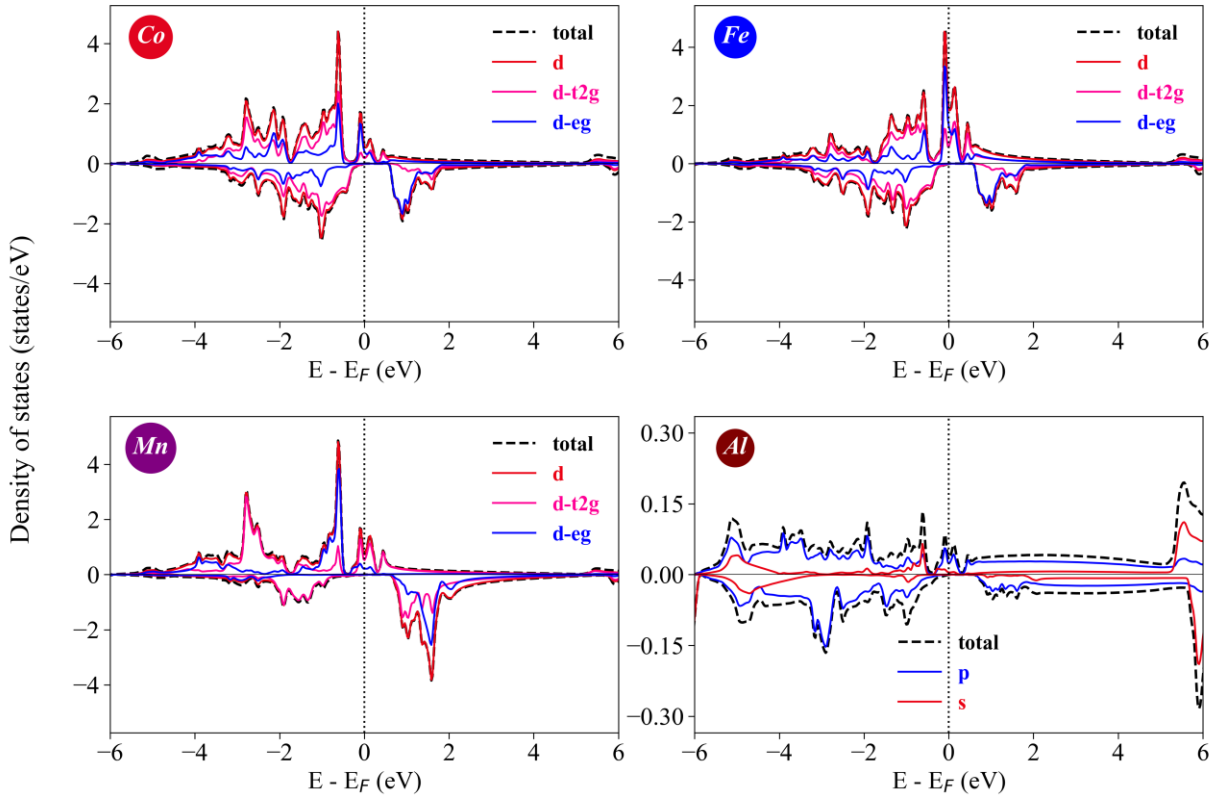


**Figure 25.** Partial density of states for atoms and orbitals for CoFeMnAl compound.

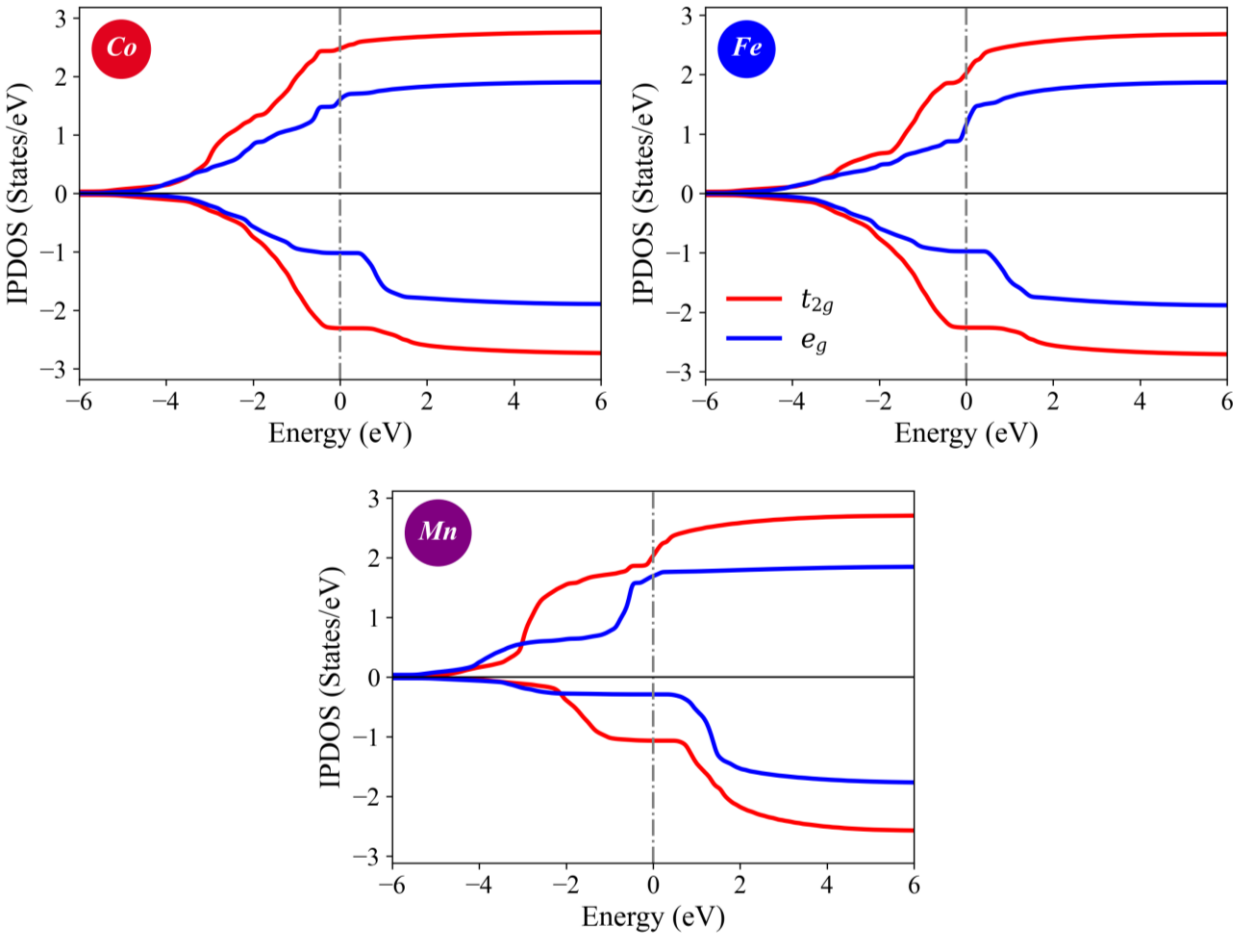


**Figure 26.** The IPDOS of Co-d, Fe-d and Mn-d orbitals for CoFeMnAl.

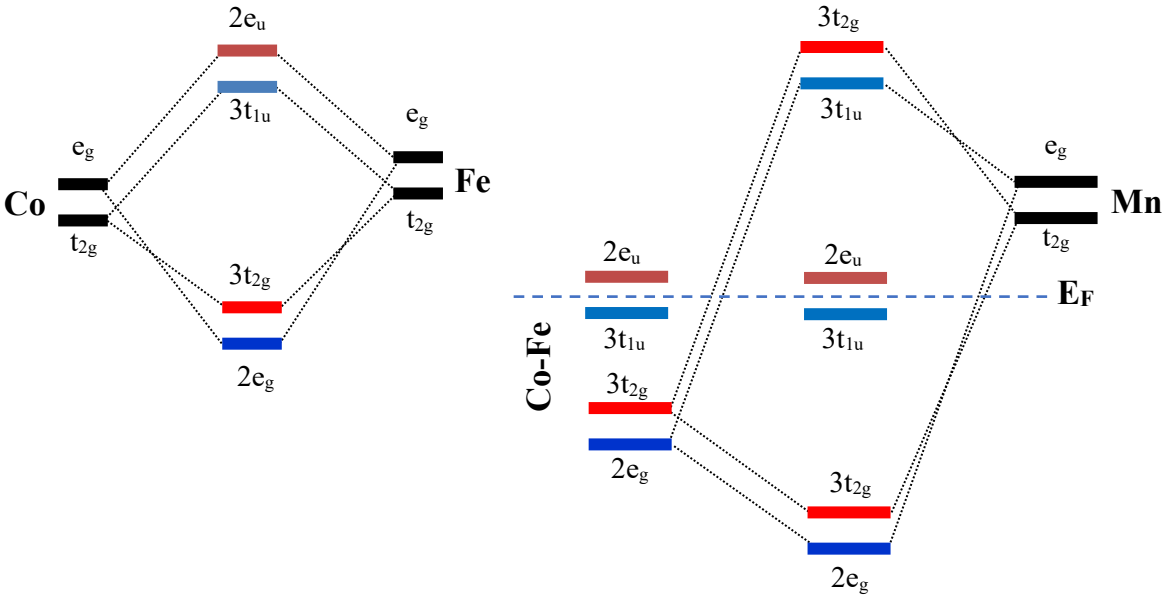


**Figure 27.** The possible d–d hybridizations between the majority spin of Co, Fe, and Mn transition metals of CoFeMnZ compounds.

### III.2.4. Magnetic properties:

One of the most intriguing features of Heusler compounds is their capacity to manipulate the magnetic properties, including the total magnetic moment and the Curie temperature. These properties can be manipulated by altering the atomic configuration or by inducing atomic disorder, rendering these materials suitable candidates in spintronics and magnetic storage technologies. To explain the magnetic origin, the IPDOS plots (Figure. 7) highlight the d-orbital occupancy for transition metal sites in both CoFeMnAl and CoFeMnGe.

The IPDOS of CoFeMnAl (**Figure 26**) indicates that the $t_{2g}$ and $e_g$ orbitals of the Co atom each possess one spin-up and one spin-down electron. The remaining d orbitals have approximately one spin-up electron, resulting in a local contribution of 0.81 $\mu_B$. The Fe atom exhibits a symmetric spin distribution in its d-shell, resulting in a minimal net magnetic moment of -0.13 $\mu_B$. The Mn atom has the most significant influence, as both spin-up and spin-down electrons occupy its $t_{2g}$ and $e_g$ orbitals. All other d orbitals contain solely spin-up electrons, resulting in a magnetic moment of 2.44 $\mu_B$. The aggregate of these site-specific contributions yields a total magnetic moment of 3.00 $\mu_B$. This integer value is expected for half-metallic ferromagnets due to the gap in the minority spin channel at the Fermi level, consistent with the Slater-Pauling rule. The dominant moment arises from the Mn site, and experimental data at 5 K show a slightly higher total value, likely due to antisite disorder.

CoFeMnGe reveals its magnetic behaviour in a similar manner (**Figure 23**). According to the IPDOS, the Co atom d orbitals contribute 0.87 $\mu_B$, the Fe 0.51 $\mu_B$ (both slightly higher than in CoFeMnAl), and the Mn atom 2.71 $\mu_B$, which is the primary source of magnetism. The calculated total magnetic moment reaches 4.02 $\mu_B$ for this alloy, again an integer value, and the Al or Ge sites are essentially nonmagnetic. The Curie temperature of CoFeMnGe, measured at 578.7 K using the mean field approximation, and CoFeMnAl at 557.4 K. The results, corroborated by prior computations and actual data, indicate that Mn is essential for the magnetic property formation.

**Table 11:** Total and partial Magnetic moment $\mu_{total}$ and $\mu_X$ in ($\mu_B$), and the Curie temperature $T_C$ in (K).

| | | $\mu_{total}$ | $\mu_{Co}$ | $\mu_{Fe}$ | $\mu_{Mn}$ | $\mu_{Al}$ | $T_C$ |
|---|---|---|---|---|---|---|---|
| **CoFeMnGe** | This work | 4.02 | 0.87 | 0.51 | 2.71 | -0.03 | 578.7 $^{MFA}$<br>524.9 $^{MC}$ |
| | Other calc[19] | 3.96 | 0.84 | 0.27 | 3.02 | -0.15 | |
| | Other calc[21] | 4.01 | 0.86 | 0.51 | 2.71 | | 711 |
| | Exp (5 K)[21] | 4.20 | | | | | |
| | Exp (300 K)[21] | 3.80 | | | | | |
| **CoFeMnAl** | This work | 3.00 | 0.81 | -0.13 | 2.44 | -0.03 | 557.4 $^{MFA}$<br>448.9 $^{MC}$ |
| | Other calc[21] | 3.00 | 0.81 | -0.13 | 2.44 | | |
| | Other calc[22] | 3.00 | 0.73 | -0.18 | 2.59 | | |
| | Exp (5K)[21] | 3.10 | | | | | |
| | Exp (300K)[21] | 2.70 | | | | | |

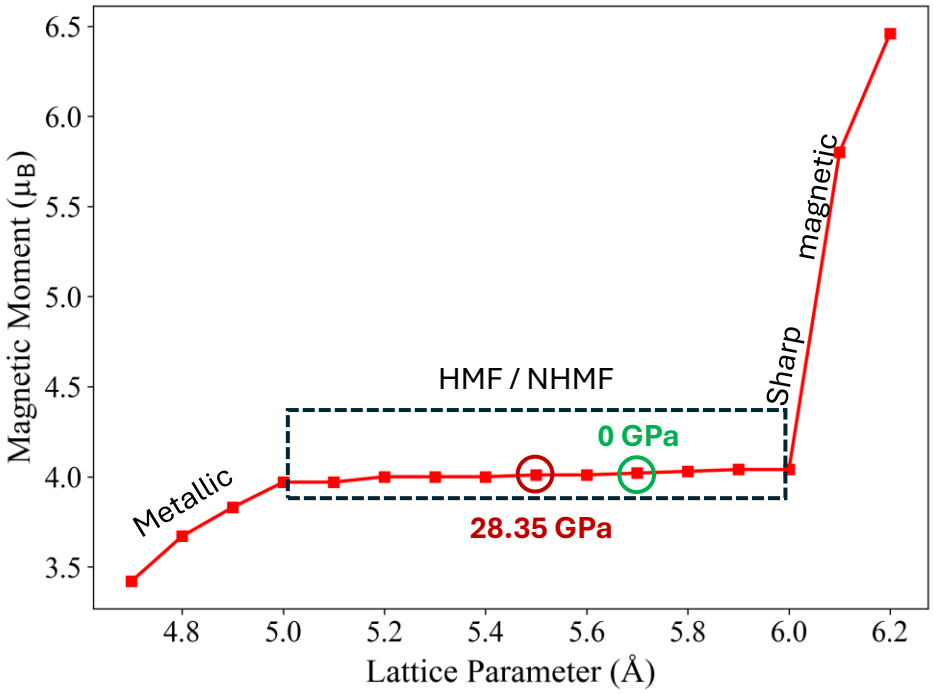


**Figure 28.** The total magnetic moment as a function of the lattice parameter for CoFeMnGe

The estimated total magnetic moment $\mu_{total}$ is an integer, which is common for half-metallic ferromagnets with a minority state band gap at the Fermi level, supporting the Slater-Pauling rule [23],[24]:

$$\mu_{total} = (N_v - 24)\mu_B \quad (15)$$

We used the classical Heisenberg to calculate the Curie temperature [25]. The Hamiltonian of a spin system described by this model is described by equation (15):

$$H = -\sum_{i,j} e_i e_j J_{ij} \quad (16)$$

Where $J_{ij}$ is the exchange coupling parameters, $e_i$ and $e_j$ are the unit vectors indicating the direction of the magnetisation on position *i and j*. The calculation of exchange coupling parameters $J_{ij}$ is done using SPRKKR package by mapping the electronic system onto a Heisenberg Hamiltonian [18].

We used the mean-field approximation (MFA) to obtain the Curie temperatures. For a single-lattice system, the Curie temperature within MFA [26] is given by:

$$\frac{3}{2} k_B T_C^{MFA} = J_0 = \sum_j J_{0j} \quad (17)$$

Where $k_B$ is the Boltzmann constant, and $J_0$ represents the total effective exchange interaction, defined as the sum of individual exchange interactions $J_{0j}$ between a central site 0 and its neighbours *j*. For a Quaternary Heusler such as our CoFeMnZ compounds, we need to extended this concept to multi-sublattice system and solve the coupled equations (17):

$$\frac{3}{2} k_B T_C^{MFA} \langle e^{\mu} \rangle = \sum_{\nu} J_0^{\mu\nu} \langle e^{\nu} \rangle \quad (18)$$

$$J_0^{\mu\nu} = \sum_{r \neq 0} J_{0r}^{\mu\nu} \quad (19)$$

Where $\langle e^{\mu} \rangle$ is the average z component of the unit vector $\langle e_r^{\mu} \rangle$ pointing in the magnetisation direction at position ($v$, $r$). (**Figure 29**) illustrates the calculated exchange coupling parameters $J_{ij}$ for Mn-Co, Mn-Fe, Mn-Mn and Mn-Ge (or Mn-Al) interactions (left panel for CoFeMnGe; right panel for CoFeMnAl) as a function of interatomic distance r.

For booth compounds the main contribution comes from interactions between different transition metal Within the 1st neighbour's atomic distance. For CoFeMnGe

Mn-Co interaction has the largest value of 13.74 meV followed by the Mn-Fe at 2.05 and Co-Fe at 0.6 eV (same for Fe-Fe interaction). For CoFeMnAl the largest value goes to Mn-Co at 15.54 meV followed by Mn-Fe at 4.22 meV and Co-Fe at 1.15 meV while the other interactions are too small and can be ignored for booth compounds.

**Table 12:** Exchange coupling parameters $J_{ij}$ in (meV) between the 1st neighbours 1:Co , 2:Fe, 3:Mn and 4:Ge (or Al).

| | $J_{11}$ | $J_{12}$ | $J_{13}$ | $J_{14}$ | $J_{22}$ | $J_{23}$ | $J_{24}$ | $J_{33}$ | $J_{34}$ | $J_{44}$ |
|---|---|---|---|---|---|---|---|---|---|---|
| **CoFeMnGe** | 0.11 | 0.60 | 13.74 | 0.14 | 0.60 | 2.05 | 0.14 | 0.07 | 0.11 | 0.00 |
| **CoFeMnAl** | 0.00 | 1.15 | 15.54 | 0.26 | 0.00 | 4.22 | 0.12 | 0.00 | 0.24 | 0.00 |

Last, we can calculate the Curie temperature by solving a 4×4 matrix equation for CoFeMnZ multi-sublattice systems. However, the Curie temperature estimated within the Mean Field Approximation is overestimated because the exchange interaction calculated from the first principle is often long-term and oscillatory [18],[26]-[27]. Consequently, it is essential to employ the Monte Carlo simulation to calculate accurate Curie temperature. We Hinzke–Nowak algorithm implemented in the Vampire package [12]. We created a 10 × 10 × 10 supercell for the calculations and set equilibrium steps to 15000 to determine the magnetisation at each temperature.

(**Figure 30**) illustrates the temperature-dependent magnetisation, from which the Curie temperatures can be derived using the fitting equation [26]:

$$m(T) = \left(1 - \frac{T}{T_C}\right)^{\beta} \tag{20}$$

Where $T$ is the temperature, $T_C$ is the Curie temperature, and $\beta$ is the critical exponent. **Table 11** reveals that the calculated Curie temperature is notably higher than room temperature, suggesting that the booth alloys can serve as promising candidates for spintronic devices.

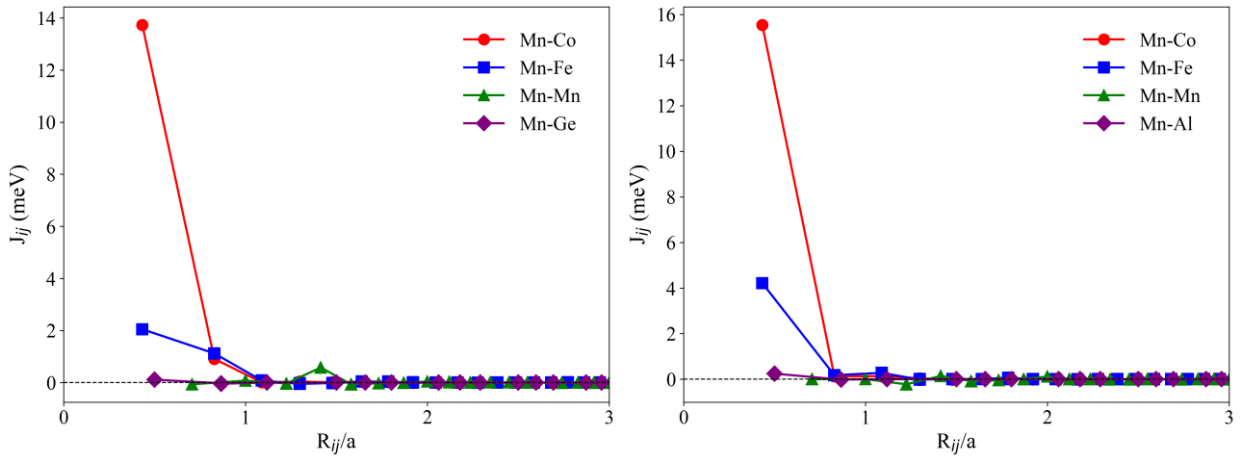


**Figure 29.** Exchange interactions as a function of the interatomic distance r

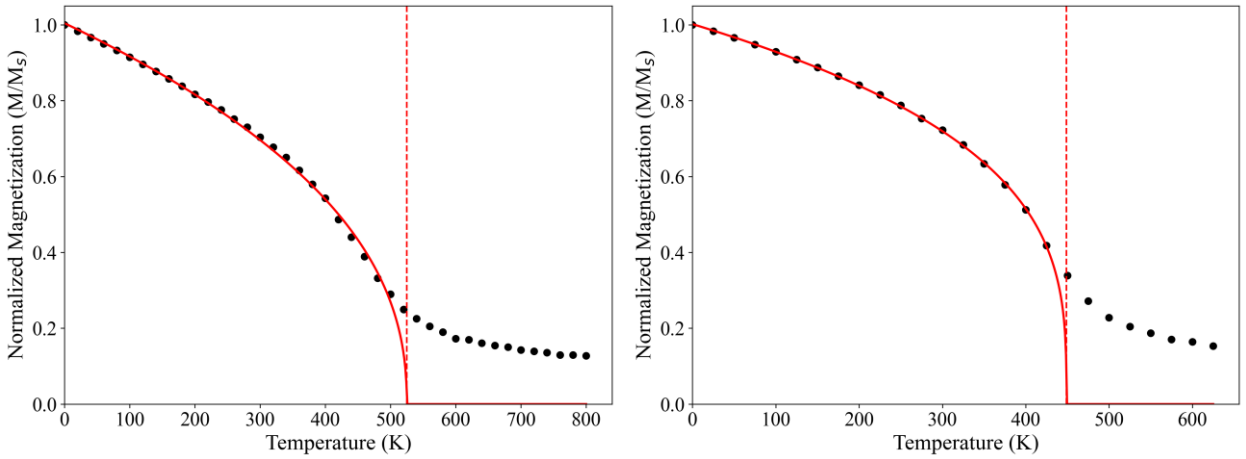


**Figure 30.** Magnetization curve as function of temperature in CoFeMnGe (left panel) and CoFeMnAl (right panel) alloys.

## III.3 Investigation of disordered CoFeMnGe:

### III.3.1. Disordered formation energy of antisite structures:

In order to evaluate the role of antisite disorder on CoFeMnGe, we created 32 atoms supercells. The ideal structure contains 8 atoms of each element. We analyse twelve structures with antisite disorder: $Ge_{Co}$, $Ge_{Fe}$, $Ge_{Mn}$, $Fe_{Co}$, $Fe_{Mn}$, $Fe_{Ge}$, $Co_{Ge}$, $Co_{Fe}$, $Co_{Mn}$, $Mn_{Co}$, $Mn_{Fe}$ and $Mn_{Ge}$. In each of these twelve configurations, one atom of the element indicated in subscript is substituted with an atom that precedes it; for instance, one Ge atom replaces one Co atom in $Ge_{Co}$ antisite. The computed disordered formation energy $E_{fd}$, band gap width, and magnetic moments are presented in Table 13.

**Table 13.** The formation energy of disorder $E_{fd}$ in (eV), total magnetic moment $\mu_{total}$ ($\mu_B$), polarisation (%) and the width of spin down gap $W_{gap}$ (eV) of possible structures with antisite disorder.

| **Antisite** | ***$E_{fd}$*** | ***$W_{gap}$*** | ***Polarisation*** | ***$\mu_{total}$*** | ***$T_C$* (MFA)** |
|---|---|---|---|---|---|
| **Ideal** | | 0.15 | 88.98 | 32.08 | 579 |
| **$Co_{Fe}$** | 0.37 | 0.40 | 95.20 | 33.00 | 596 |
| **$Co_{Ge}$** | -8.84 | 0.00 | 81.82 | 36.78 | 661 |
| **$Co_{Mn}$** | -8.59 | 0.60 | 51.05 | 32.13 | 580 |
| **$Fe_{Co}$** | -0.35 | 0.60 | 90.76 | 31.10 | 562 |
| **$Fe_{Ge}$** | -9.95 | 0.35 | 99.95 | 36.00 | 648 |
| **$Fe_{Mn}$** | -9.77 | 0.40 | 91.13 | 33.08 | 597 |
| **$Ge_{Co}$** | 12.84 | 0.45 | 88.55 | 33.00 | 596 |
| **$Ge_{Fe}$** | 13.27 | 0.00 | 76.41 | 34.00 | 612 |
| **$Ge_{Mn}$** | 1.67 | 0.50 | 88.9 | 29.13 | 527 |
| **$Mn_{Co}$** | 9.38 | 0.40 | 92.02 | 30.00 | 544 |
| **$Mn_{Fe}$** | 9.87 | 0.20 | 89.75 | 31.08 | 562 |
| **$Mn_{Ge}$** | 0.00 | 0.53 | 99.11 | 35.00 | 630 |

The lowest value of formation energy (-9.95 eV) corresponds to $Fe_{Ge}$ antisite disorder, while the highest $E_{fd}$ values (13.27 eV, 12.84 eV, 9.87 eV and 9.38 eV) are associated with $Ge_{Fe}$, $Ge_{Co}$, $M_{nFe}$ and $Mn_{Co}$ antisites, respectively. These high-energy defects can often be removed through annealing processes. $Fe_{Mn}$, $Co_{Ge}$, $Co_{Mn}$ and $Fe_{Co}$ antisite defects are also likely to form due to their negative disordered formation energies of -9.77 eV , -8.84 eV, -8.59 eV and -0.35 eV respectively. These defects are most likely to happen alongside $Fe_{Ge}$ defects. Moreover. $Mn_{Ge}$ antisites have a disordered formation energy of 0 eV and cannot be ignored.

### III.3.2. Effects of Antisite Disorder on the Electronic properties:

The band structures (BS) and density of states (DOS) for each of the twelve antisite configurations are shown in **Figure 31** and **Figure 33**, respectively. All twelve antisite configurations exhibit substantial modifications in their electronic properties compared to the ordered CoFeMnGe configuration, which has a spin polarisation of 98.58% and a spin-down band gap around 0.5 eV with $C_{MB}$ slightly above the Fermi level, thereby establishing nearly-half-metallic behaviour. Antisite defects globally maintain the gap width in minority-spin states; nevertheless, certain configurations can destroy half-metallicity.

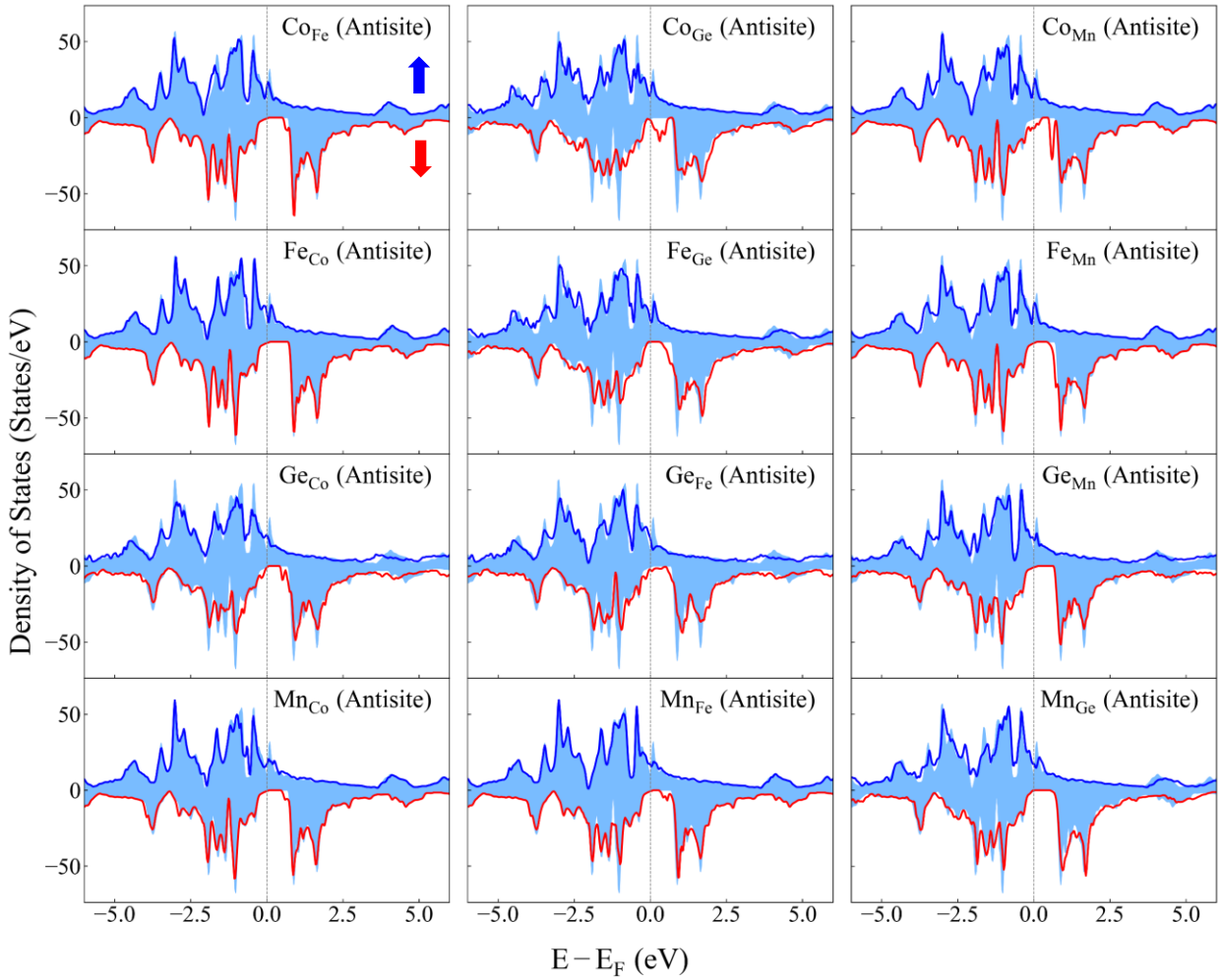


**Figure 31.** The total density of states of possible kinds of antisite disordered structures. The shadow region in blue color is the DOS of ideal CoFeMnGe, the solid line is the DOS of antisite disordered structures.

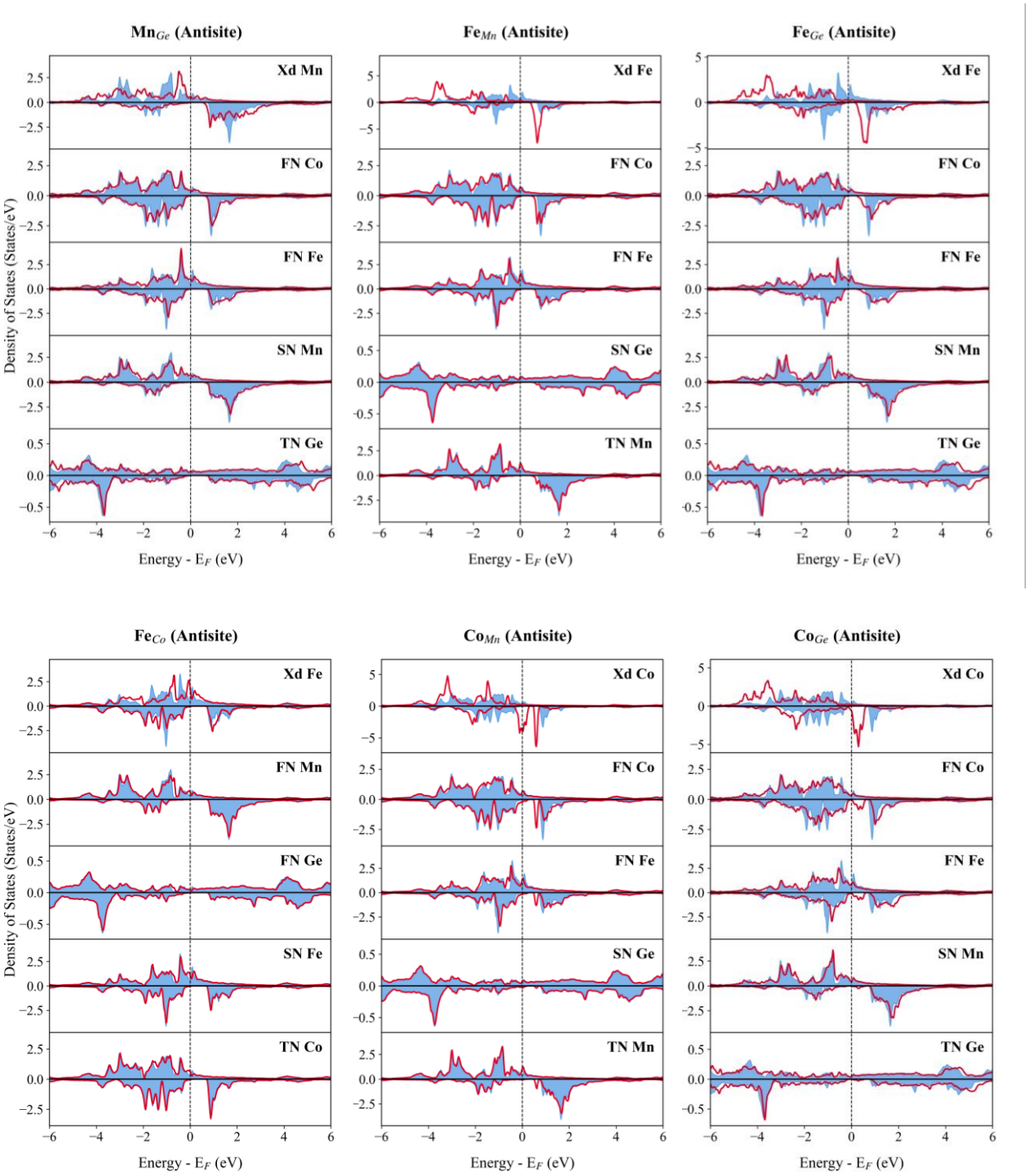


**Figure 32.** The PDOS of most favourable antisite defect structures. The FN, SN and TN are respectively the first-neighbour, second-neighbour and third neighbour of defective atom, the blue shadow is the PDOS of corresponding atom in perfect CoFeMnGe.

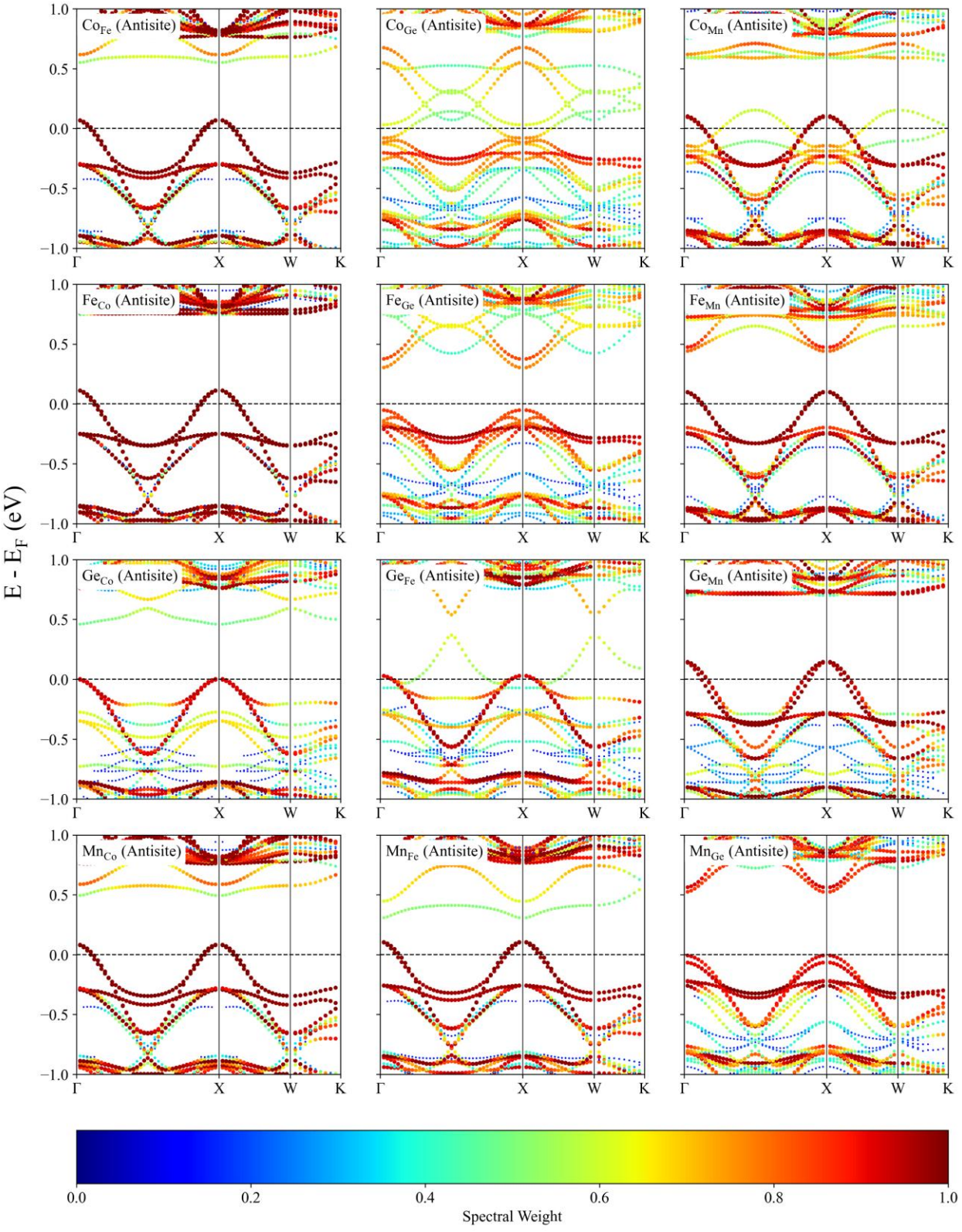


**Figure 33**. The band structure of twelve possible kinds of antisite disordered structures for CoFeMnGe compound.

$Co_{Ge}$ and $Ge_{Fe}$ antisite structures may destroy half-metallicity completely by causing state overlap at the Fermi level, therefore eliminating the spin-down gap. The DOS charts for

these combinations demonstrate that states intersect the Fermi level. Their respective band structures display metallic properties because new electronic states emerge within the minority spin band gap at the Fermi level, converting the material into a regular metal. The polarisation is reduced to 81.82% for $Co_{Ge}$ and 76.41% for $Ge_{Fe}$. $Fe_{Ge}$ and $Mn_{Ge}$ antisite display increased half-metallic properties pushing the $V_{BM}$ below the Fermi level, often leading to a perfect half-metallic phase with band gap width of 0.35eV and 0.53 eV respectively $Fe_{Ge}$ and $Mn_{Ge}$ antisite have the highest increase in spin polarisation to 99.95% and 99.11%.

**Figure 32** illustrates the PDOS of the first, second and third neighbours for the most favourable antisite defects in CoFeMnGe. A clear, distance-dependent influence on electronic properties is revealed. The FN undergo significant shifts in peak positions and intensities in the −2 to +2 eV range around the Fermi level and modified d-orbital hybridisation; second neighbours display moderate perturbations (20–40 % intensity variations concentrated around −1 to +1 eV) yet preserve the overall PDOS profile; third neighbours, by contrast, show only subtle peak deviations, closely mirroring the perfect crystal and confirming the localised nature of defect-induced electronic restructuring.

### III.3.3. Effect of Antisite on the Magnetic Properties:

Antisite imperfections in quaternary Heusler alloys may impact their magnetic properties, particularly the total magnetic moment ($\mu_{total}$) and the Curie temperature ($T_C$). We have summarised these effects across twelve unique antisite combinations in **Table 13** and **Table 15**. The ideal CoFeMnGe supercell configuration, with a total magnetic moment of 32.08 $\mu_B$ and a Curie temperature of 579 K, is taken as a reference for comparison. The introduction of antisite disorder disrupts the d-orbital hybridisation between the transition metals (Co, Fe, Mn). This disturbance can alter the magnetisation and the exchange interactions that define the ferromagnetic state and its thermal stability. For instance, we observed that many antisite defects increase both the total magnetic moment and the Curie temperature, indicating a more robust ferromagnetic state.

The antisites $Co_{Ge}$, $Fe_{Ge}$, $Mn_{Ge}$, $Ge_{Fe}$, $Ge_{Co}$, $Co_{Fe}$ and $Fe_{Mn}$ all enhance $\mu_{total}$ and $T_C$. The $Co_{Ge}$ antisite demonstrates a noticeable enhancement in both characteristics, with $\mu_{total}$

attaining 36.78 $\mu_B$ and $T_C$ reaching 648 K followed by $Fe_{Ge}$ antisite which exhibits an increase to 36.00 $\mu_B$ and 661 K. That demonstrate the replacing Ge atom by one transition metal have a high impact on magnetic behaviour on the compound. Conversely, defects such as $Ge_{Mn}$ , $Mn_{Co}$, $Mn_{Fe}$ and $Fe_{Co}$ antisites result in decreasing $\mu_{total}$ to 29.13 – 31.10 $\mu_B$ and $T_C$ to 527 – 562 K, suggesting reduced magnetic interactions. The magnetic moment for the $Fe_{Mn}$ antisite is 33.08 $\mu_B$ (4.135 $\mu_B/f$.u), closely matching the experimental value measured at 5 K. This indicates that this particular arrangement may represent the material's magnetic state under standard synthesis conditions. These defects may affect the validity of the Slater-Pauling rule. The total number of valence electrons for an ideal 32-atom supercell of CoFeMnGe is 224. Assuming optimal half-metallicity and the rigid band model during an antisite substitution (e.g., Y → X), we can forecast the total magnetic moment by counting valence electrons and modifying the slater equation:

$$\mu_{total_{supercell}} = (4 \times 8) + (V_X - V_Y) = 32 + (V_X - V_Y)\mu_B \quad (21)$$

Or:

$$\mu_{total} = 4 + \frac{(V_X - V_Y)}{8}\mu_B/f.u \quad (22)$$

The total number of valence electrons is modified by $V_X - V_Y$, $V_X$ and $V_Y$ are the valence electrons of the substituting and substituted atoms, respectively.

For example, $Co_{Fe}$ antisite reduces the supercell's total valence electrons by 1.

$$\mu_{total}(\mathrm{Co_{Fe}}) = 32 + 1 = 33\ \mu_B$$

we would anticipate an integer total moment of 33 $\mu_B$ for the 32-atom defected supercell. By normalising this to the formula unit (divided by 8, as our 32-atom supercell contains eight formula units), we derive an expected moment of $\mu_{total} = 33/8 = 4.125\ \mu_B/f$.u. Moreover, the total magnetic moment values obtained for these disordered structures, as presented in **Table 13** (even when normalised to the 32-atom supercell), frequently deviate significantly from these straight forward expectations. Specific configurations such as $Co_{Fe}$, $Fe_{Ge}$, $Ge_{Co}$, $Mn_{Co}$, and $Mn_{Ge}$ antisites produce total supercell moments that are integer values, e.g., Ideal at 32.0 $\mu_B$, $Fe_{Ge}$ at 36.0 $\mu_B$, $Mn_{Ge}$ at 35.0 $\mu_B$). In contrast, others, including

$Co_{Ge}$ (36.78 $\mu_B$), $Co_{Mn}$ (32.13 $\mu_B$), $Fe_{Co}$ (31.10 $\mu_B$), $Ge_{Mn}$ (29.13 $\mu_B$), and $Mn_{Fe}$ (31.08 $\mu_B$), lead to non-integer values for the complete supercell indicating that the simple Slater-Pauling rule **(Figure 34)** is not entirely relevant to these disordered systems. These deviations and complex behaviours occur due to the influence of antisite defects on the hybridisation interactions and crystal field splitting of the transition metal d-orbitals. Modifications in bond lengths, orbital overlaps, and the surrounding atomic environment of the defect significantly influence these factors.

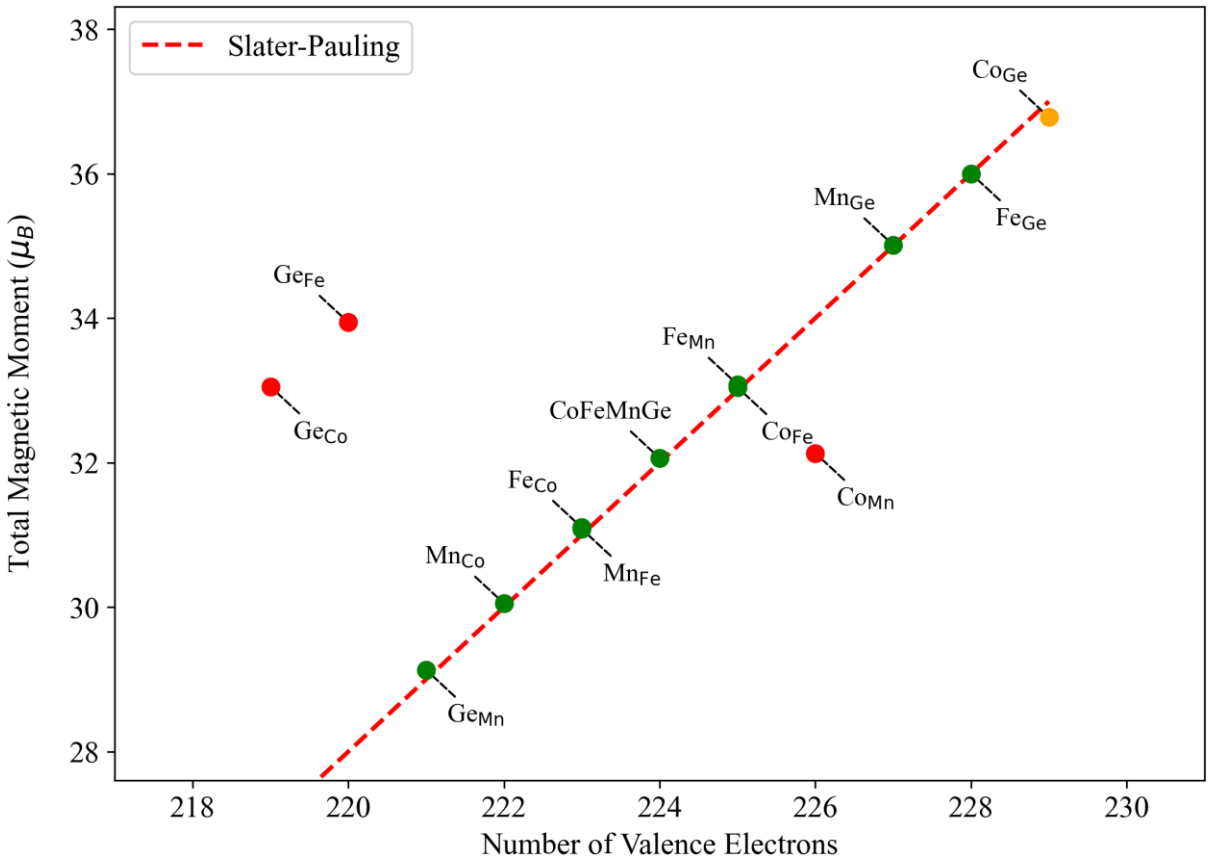


**Figure 34.** Magnetic moment vs valence electrons for antisite defected CoFeMnGe

### III.3.4. Formation Energy of Swap Disordered Structure:

In order to figure out the effects of swap disorder on CoFeMnGe, we constructed supercells with 32 atoms. We investigate all six distinct kinds of swap disorder: CoFe, CoGe, CoMn, FeGe, FeMn, and MnGe. In each of these six configurations, one atom of the element X is exchanging its position with an atom of element Y creating XY swap; for instance, one Fe atom switches its position with a Mn atom in the FeMn structure. Whether the creation of

XY swap disorder is stable regarding its associated X(Y) and Y(X) antisite disorders is dictated by the pair binding energy, which is approximated as [7]:

$$E_b^{XY} = E_f^{X(Y)} + E_f^{Y(X)} - E_f^{XY} \quad (23)$$

Where $E_f^{XY}$ is the disorder formation energy of the XY swap configuration and $E_f^{X(Y)}$and $E_f^{Y(X)}$ are the disorder formation energy for $X_Y$ and $Y_X$ antisite configuration.

A positive pair binding energy relates to a stable swap structure, but simply having a positive pair binding energy does not mean that the compound will certainly form.
Based on the analysis of formation energies and pair binding energies in **Table 14**, all swap configurations have positive disordered formation energy indicating that type of defects isn't favourited for CoFeMnGe compound. CoFe has been identified as the most stable swap defect. It has a negative formation energy of 0 eV and a negative binding energy of -0.02 eV, showing that it is less energetically stable with its corresponding $Fe_{Co}$ antisite. Although not easily removed, it may still impact on the material's formation. CoGe, FeGe and MnGe, have high formation energies of 3.03 eV, 2.64 eV and 1.66 eV, respectively, and can be eliminated.

**Table 14:** The formation energy of disorder $E_{fd}$ in (eV), the magnetic moment $\mu_{total}$ ($\mu_B$), polarization (%) , Curie temperature $T_C$ (K) and width of spin down gap $W_{gap}$ (eV) of possible structures with swap disorder.

| **Swap** | $E_{fd}$ | $E_b$ | $P$ **(%)** | $W_{gap}$ | $\mu_{total}$ | $T_C$ **(MFA)** |
|---|---|---|---|---|---|---|
| **Ideal** | | | 88.98 | 0.15 | 32.08 | 579 |
| **CoFe** | 0.01 | 0.01 | 90.06 | 0.40 | 32.05 | 579 |
| **CoGe** | 3.03 | 0.97 | 82.29 | 0.00 | 37.85 | 680 |
| **CoMn** | 0.82 | -0.03 | 42.51 | 0.40 | 29.62 | 536 |
| **FeGe** | 2.64 | -2.54 | 97.24 | 0.20 | 38.01 | 683 |
| **FeMn** | 0.15 | 3.18 | 88.84 | 0.30 | 32.09 | 579 |
| **MnGe** | 1.66 | 0.02 | 98.57 | 0.50 | 32.00 | 578 |

**Table 15:** The calculated total magnetic moment $\mu_{tot}$ of four most favourable defective structures, magnetic moment of defective atoms ($X_d$) and its first-neighbour atom (FN), second-neighbour atom (SN) as well as third neighbour atom (TN).

| System | Co(uB) | Fe(uB) | Ge(uB) | Mn(uB) | $\mu_{tot}(\mu_B)$ |
|---|---|---|---|---|---|
| **Ideal** | 0.858 | 0.492 | -0.033 | 2.718 | 32.06 |
| **Defect** | **$X_d$** | **FN** | **SN** | **TN** | **$\mu_{tot}(\mu_B)$** |
| **$Co_{Ge}$** | Co: 2.006 | Co: 1.059<br>Fe: 1.154 | Mn: 2.685 | Ge: -0.055 | 36.78 |
| **$Co_{Mn}$** | Co: 1.663 | Co: 0.878<br>Fe: 0.879 | Ge: -0.034 | Mn: 2.648 | 32.13 |
| **$Fe_{Co}$** | Fe: 0.094 | Mn: 2.687<br>Ge: -0.027 | Fe: 0.440 | Co: 0.870 | 31.10 |
| **$Fe_{Ge}$** | Fe: 2.781 | Co: 1.010<br>Fe: 0.788 | Mn: 2.699 | Ge: -0.045 | 36.00 |
| **$Fe_{Mn}$** | Fe: 2.730 | Co: 0.897<br>Fe: 0.783 | Ge: -0.033 | Mn: 2.670 | 33.08 |
| **$Mn_{Ge}$** | Mn: 2.814 | Co: 0.928<br>Fe: 0.560 | Mn: 2.672 | Ge: -0.040 | 35.01 |
| **CoFe** | Fe: 0.236<br>Co: 0.880 | Mn: 2.768<br>Ge: -0.031 | Co: 0.880<br>Fe: 0.236 | Co: 0.863<br>Fe: 0.519 | 32.05 |

## III.3.5. Effect of Swap Disorder on the Electronic Properties:

In addition to antisite imperfections, swap disorder highly impacts the electronic and half-metallic features of CoFeMnAl. The density of states (DOS) and band structures (BS) for all six swap configurations are illustrated in (**Figure 35**), (**Figure 36**) and (**Figure 37**) respectively, with pertinent data summarised in **Table 14**.

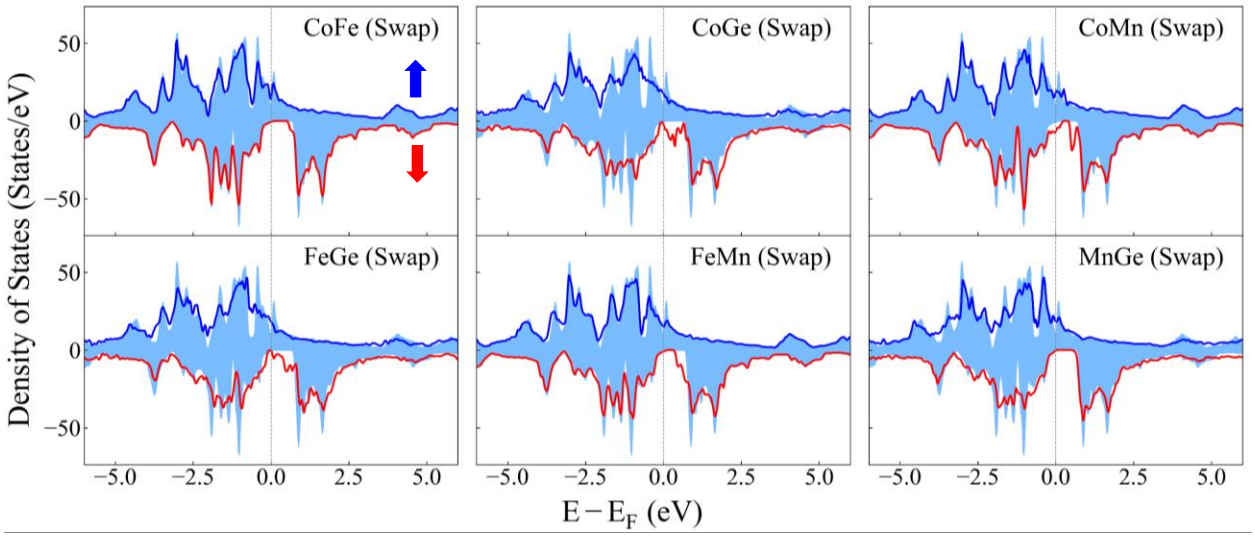


**Figure 35.** The total density of states of possible kinds of swap disordered structures. The shadow region in blue color is the DOS of ideal CoFeMnGe, the red solid line is the DOS of antisite disordered structures.

The investigation of these configurations indicates strong maintenance of near-half-metallicity in CoFe, MnGe and FeM. CoGe and CoMn swap configurations exhibit metallic character, demonstrating no gap in the minority spin channel and notably diminished polarisations to 82.29% and 42.51%. The band structures reveal states overlapping the Fermi level in the minority spin channel. However, the FeGe swap structure displays half-metallic character revealing high polarisation increase and pushing the $V_{BM}$ below the Fermi level.

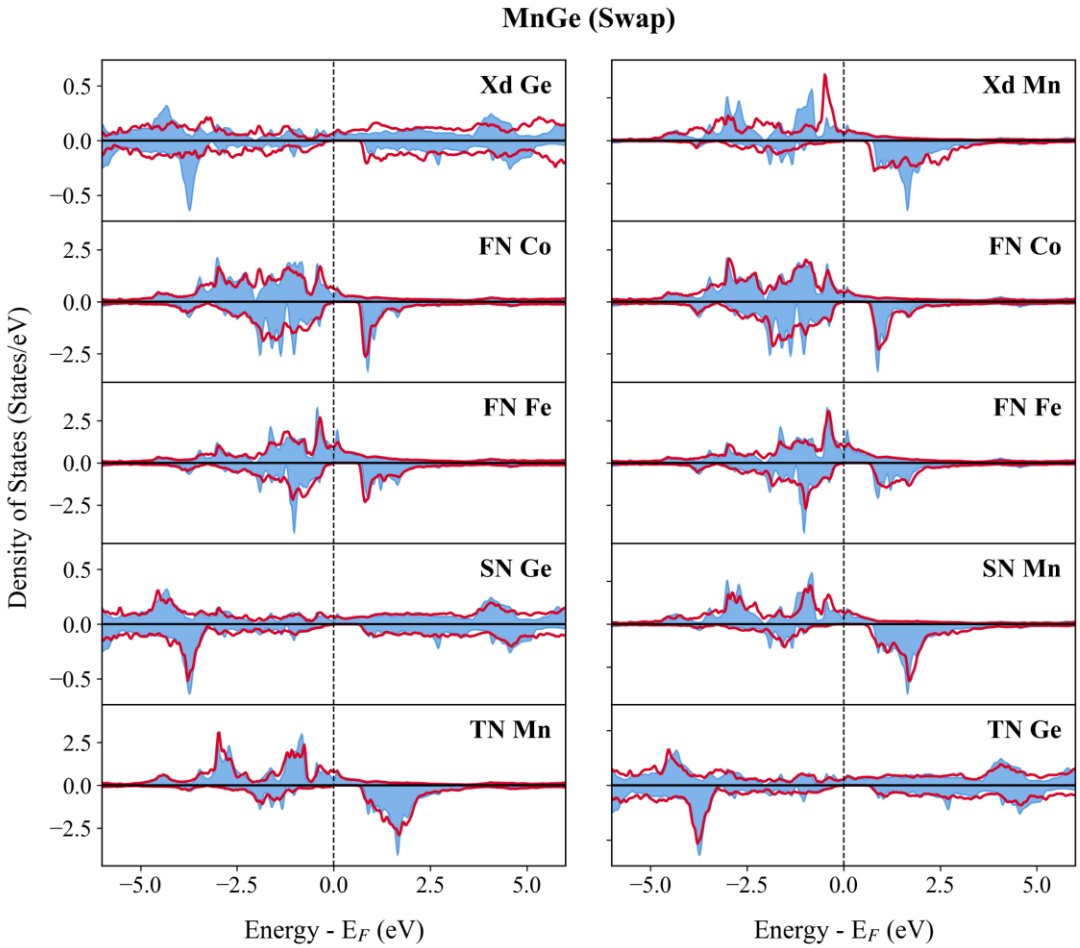


**Figure 36.** The PDOS of most favourable swap defect structures. The FN, SN and TN are respectively the first-neighbour, second-neighbour and third neighbour of defective atom, the blue shadow is the PDOS of corresponding atom in perfect CoFeMnGe.

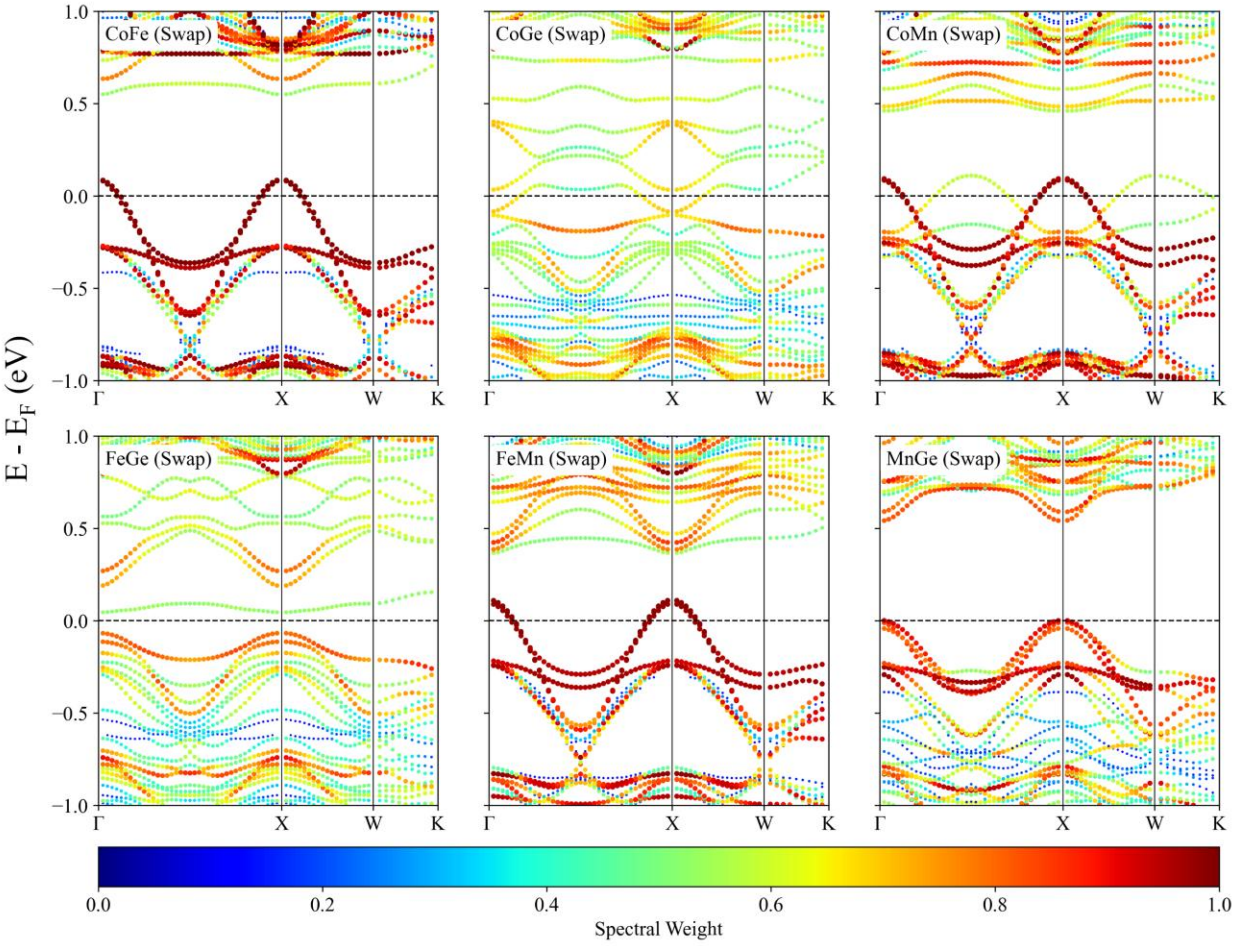


**Figure 37.** The band structure of six possible kinds of swap disordered structures for CoFeMnGe compound.

## III.3.6. Effect of Swap Disorder on the Magnetic Properties

Beyond antisite imperfections, swap disorder, arising from the interchange of atomic positions, also influences the magnetic properties. From **Table 14** and **Table 15**, MnGe swaps maintains a total magnetic moment of 32.00 $\mu_B$. This is attributed to a local moment compensation; for the CoFe swap, the negative moment induced at the Fe(Co) site (-0.37 $\mu_B$) is effectively balanced by the positive moment at the Co(Fe) site (0.94 $\mu_B$). Their Curie temperatures are very close, with CoFe and FeMn swaps at 579 K and MnGe at 578 K. These particular swap disorders have minimal effect on overall magnetisation and the thermal stability of the ferromagnetic state.

On the contrary, the FeGe and CoGe swap configurations increase $\mu_{total}$ to 38.01 $\mu_B$ and 37.85 $\mu_B$ and push the Curie temperatures to 673 K and 672 K, respectively, indicating a significant modification of d-orbital hybridisation and associated exchange interactions.

Defective atoms exhibit enhanced moments (notably 2.814 $\mu_B$ for MnGe, 2.781 $\mu_B$ for FeGe and 2.730 $\mu_B$ for FeMn), while first-neighbour Mn retains remarkable stability (2.68–2.77 $\mu_B$), in contrast to Co and Fe which vary more broadly (0.560–1.154 $\mu_B$ and 0.878–2.77 $\mu_B$, respectively). Second neighbours experience moderate moment deviations (5–40 percent), and third neighbours show minimal change (< 10 percent), with Ge consistently bearing small negative moments (−0.040 to −0.055 $\mu_B$) and Mn remaining close to its ideal moment (2.648–2.670 $\mu_B$). This combined analysis, focused on the near neighbours of the most energetically favourable antisite defects, underscores the intrinsic defect resilience of the quaternary Heusler alloy.

## III.4 Investigation of disordered CoFeMnAl:

### III.4.1. Disordered formation energy of antisite structures:

In order to evaluate the role of antisite disorder on CoFeMnAl, we created 32 atoms supercells. The ideal structure contains 8 atoms of each element. We analyse 12 structures with antisite disorder: $Al_{Co}$, $Al_{Fe}$, $Al_{Mn}$, $Fe_{Co}$, $Fe_{Mn}$, $Fe_{Al}$, $Co_{Al}$, $Co_{Fe}$, $Co_{Mn}$, $Mn_{Co}$, $Mn_{Fe}$ and $Mn_{Ge}$. In each of these 12 configurations, one atom of the element indicated in subscript is substituted with an atom that precedes it; for instance, one Al atom replaces one Co atom in $Al_{Co}$ antisite. The computed disordered formation energy $E_{fd}$, band gap width, and magnetic moments are presented in **Table 16**.

The lowest value of formation energy (-1.25 eV) corresponds to $Fe_{Mn}$ antisite disorder, while the highest $E_{fd}$ values (2.39 eV, 1.94 eV and 1.39 eV) are associated with $Al_{Co}$, $Al_{Fe}$ and $M_{nFe}$ antisites, respectively. These high-energy defects can often be removed through annealing processes. $Fe_{Al}$ and $Al_{Mn}$ antisite defects are also likely to form, with formation energies of -0.74 eV and -0.23 eV, respectively. These defects are most likely to happen with $Fe_{Mn}$ defects. Moreover, $Co_{Mn}$, $Co_{Fe}$, $Co_{Al}$, $Mn_{Al}$ and $Mn_{Co}$ antisites have slightly higher values of disordered formation energy and may not be removed easily.

**Table 16:** The formation energy of disorder $E_{fd}$ in (eV), total magnetic moment μtotal ($\mu_B$) , polarisation (%) and the width of spin down gap $W_{gap}$ (eV) of possible structures with antisite disorder.

| **Antisite** | $E_{fd}$ | $W_{gap}$ | *Polarisation* | $\mu_{total}$ | $T_C$ (MFA) |
|---|---|---|---|---|---|
| **Ideal** | | 0.62 | 98.58 | 24.00 | 557 |
| **$Al_{Co}$** | 1.94 | 0.46 | 95.23 | 24.00 | 557 |
| **$Al_{Fe}$** | 2.39 | 0.58 | 98.20 | 25.00 | 580 |
| **$Al_{Mn}$** | -0.13 | 0.26 | 99.02 | 20.00 | 468 |
| **$Fe_{Co}$** | -0.58 | 0.57 | 99.14 | 23.00 | 536 |
| **$Fe_{Mn}$** | -1.25 | 0.39 | 95.71 | 25.00 | 578 |
| **$Fe_{Al}$** | -0.74 | 0.38 | 99.95 | 29.00 | 667 |
| **$Co_{Al}$** | 0.49 | 0.00 | 90.88 | 26.24 | 607 |
| **$Co_{Fe}$** | 0.50 | 0.49 | 97.95 | 26.24 | 607 |
| **$Co_{Mn}$** | 0.09 | 0.00 | 68.14 | 26.16 | 605 |
| **$Mn_{Al}$** | 0.67 | 0.50 | 99.94 | 22.56 | 525 |
| **$Mn_{Co}$** | 0.82 | 0.43 | 98.61 | 28.00 | 646 |
| **$Mn_{Fe}$** | 1.39 | 0.46 | 99.26 | 21.84 | 509 |

## III.4.2. Effects of Antisite Disorder on the Electronic properties:

The band structures (BS) and density of states (DOS) for each of the twelve antisite configurations are shown in (**Figure 38**), (**Figure 39**) and (**Figure 40**), respectively. All twelve antisite configurations exhibit substantial fluctuations in their electronic properties compared to the ideal CoFeMnAl structure, which has a spin polarisation of 98.58% and a spin-down band gap of 0.62 eV, thereby establishing its half-metallic behaviour. Antisite disorders globally reduce the gap width of minority-spin states; nevertheless, certain configurations can destroy half-metallicity. $Co_{Al}$ and $Co_{Mn}$ antisite structures destroy half-metallicity by causing state overlap at the Fermi level, therefore eliminating the spin-down gap. The DOS charts for these combinations demonstrate that states intersect the Fermi level. Their respective band structures display metallic properties because new electronic states emerge within the minority spin band gap at the Fermi level, converting the material into an ordinary metal. However, they claim a polarisation of 90.88% for $Co_{Al}$ and 68.14% for $Co_{Mn}$. $Al_{Mn}$, $Fe_{Mn}$, $Co_{Fe}$, and $Mn_{Co}$ antisite display

reduced half-metallic properties without completely destroying it, often leading to a nearly half-metallic phase. The valence band of the $Fe_{Mn}$ structure barely intersects the Fermi level, suggesting a slight metallic character despite the presence of a clear band gap and high spin polarisation. The $Al_{Mn}$, $Co_{Fe}$, and $Mn_{Co}$ structures, characterised by significant polarisation, have their valence band maxima at the Fermi level, indicating a nearly half-metallic behaviour. $Fe_{Co}$ antisite has high polarisation and gap in the spin-down channel, while it demonstrates reduced robustness compared to the perfect crystal.

Conversely, other antisite configurations, such as $Al_{Fe}$, $Mn_{Al}$, $Mn_{Fe}$, $Fe_{Al}$, $Al_{Co}$, and $Fe_{Co}$, continually preserve their half-metallic characteristics as their valence bands are consistently positioned below the Fermi level. These structures typically demonstrate substantial spin polarisation and noticeable spin-down gaps. For example, $Al_{Fe}$ exhibits significant spin polarisation and a gap that closely aligns with the ideal.

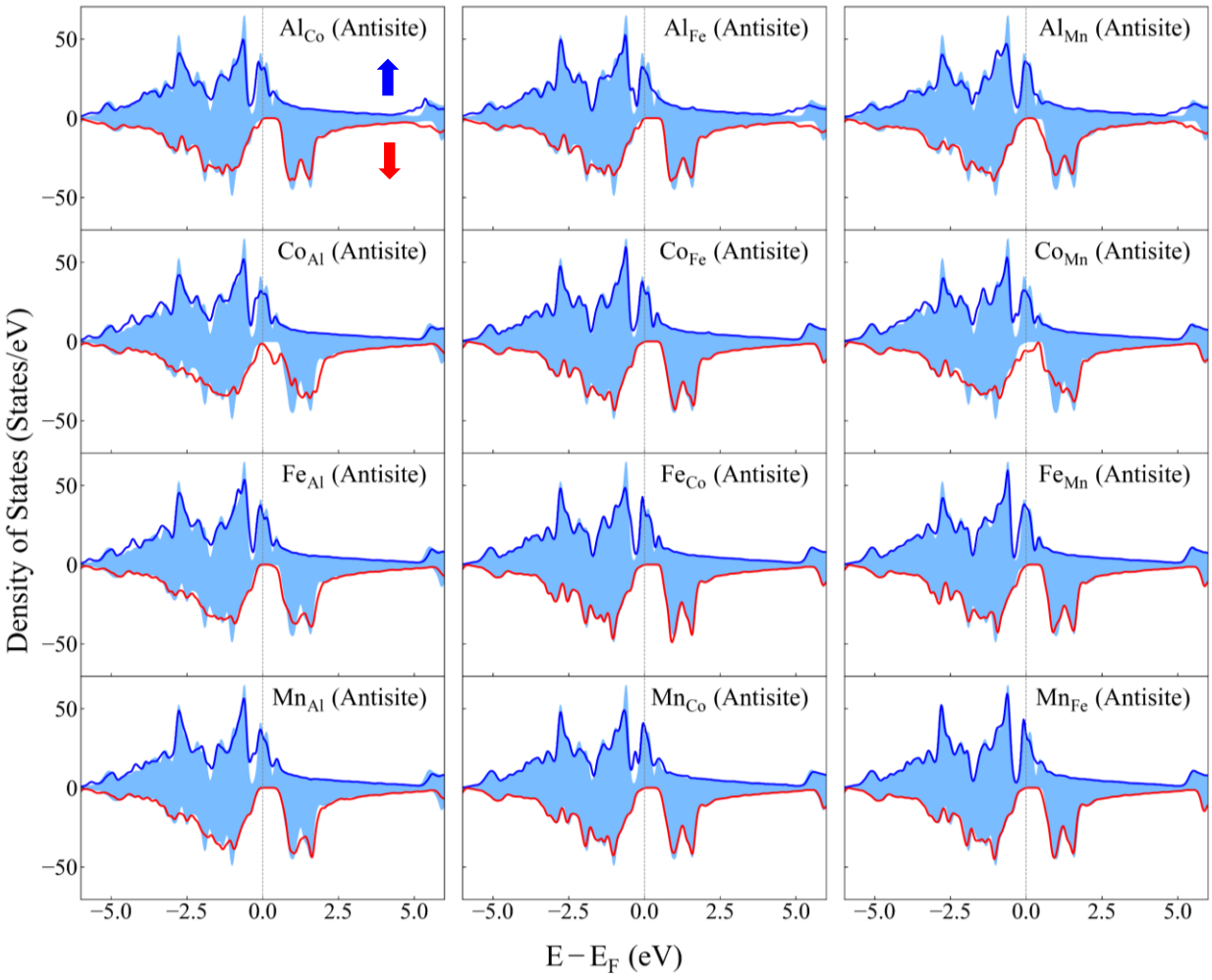


**Figure 38.** The total density of states of possible kinds of antisite disordered structures. The blue shadow region is the DOS of ideal CoFeMnAl, the solid line is the DOS of antisite disordered structures.

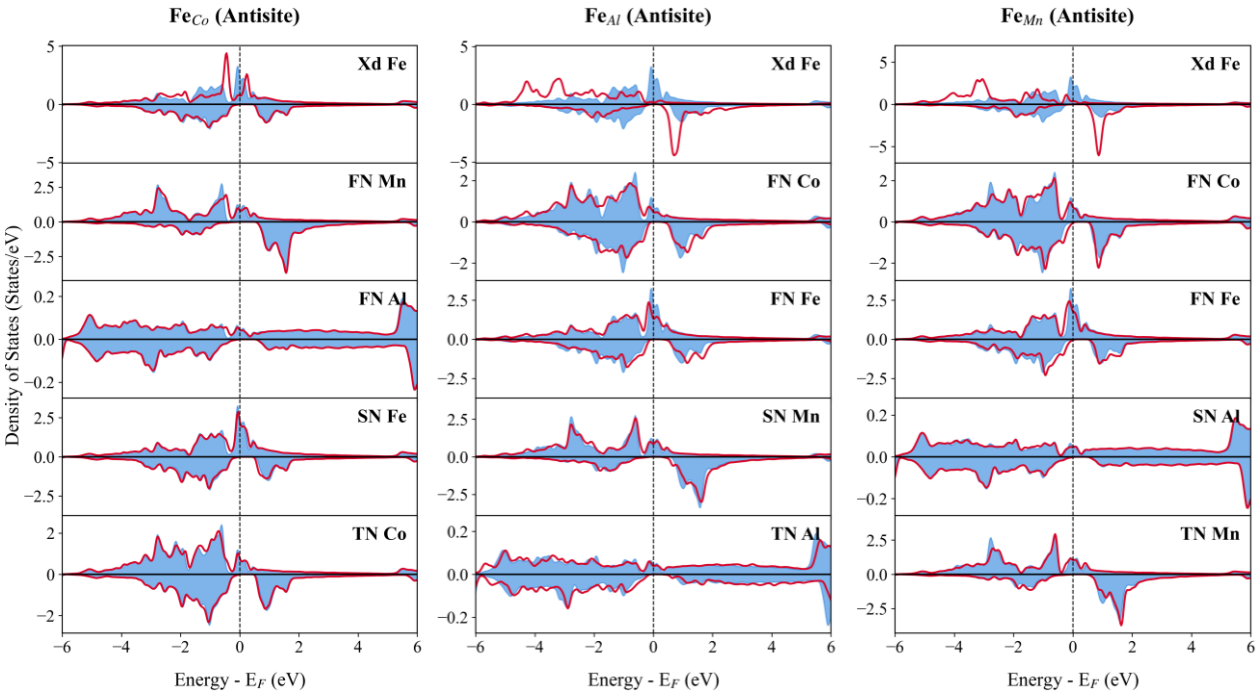


**Figure 39.** The PDOS of most favourable antisite defect structures. The FN, SN and TN are respectively the first-neighbour, second-neighbour and third neighbour of defective atom, the blue shadow is the PDOS of corresponding atom in perfect CoFeMnAl.

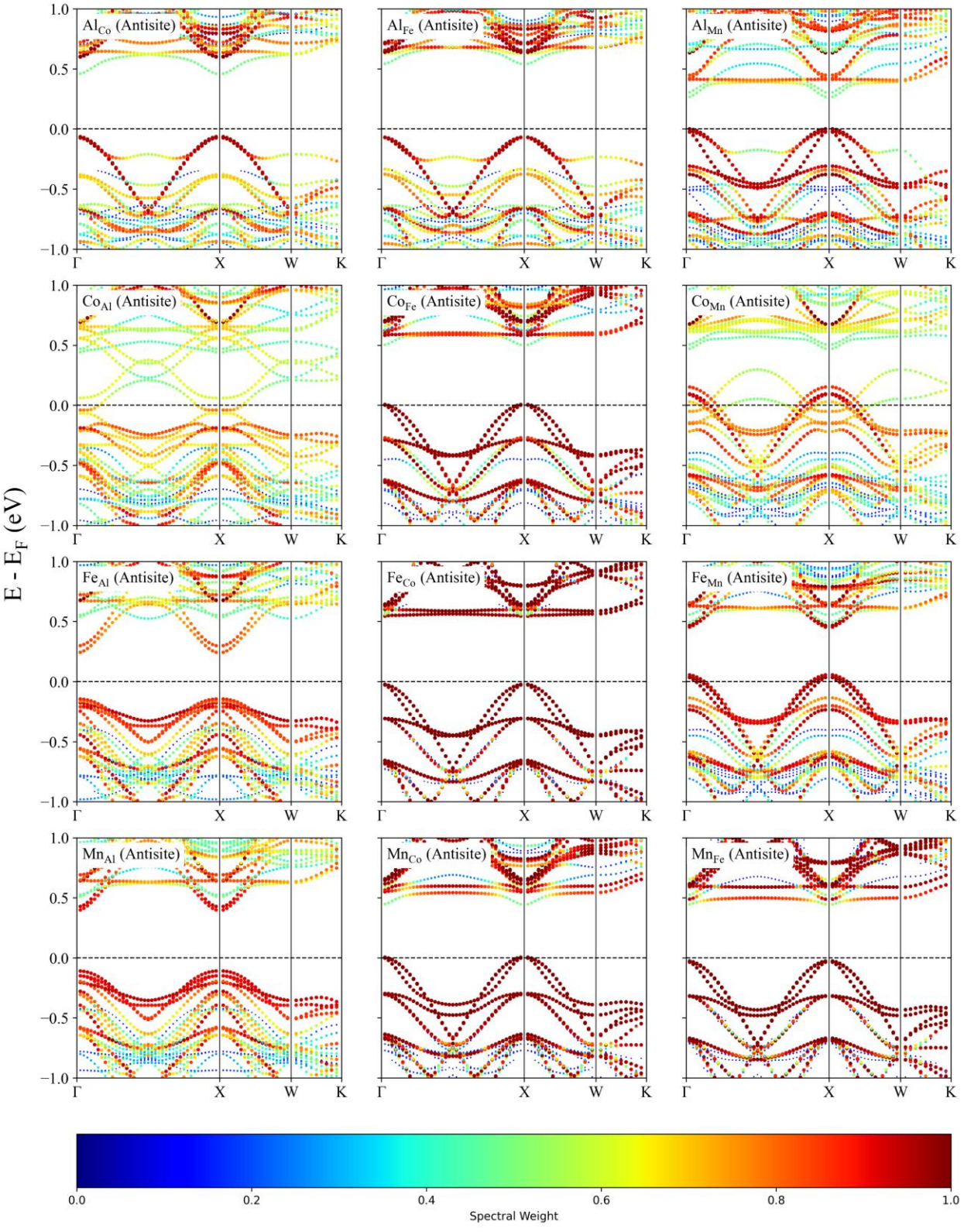


**Figure 40.** The band structure of twelve possible kinds of antisite disordered structures for CoFeMnAl compound.

### III.4.3. Effect of Antisite on the Magnetic Properties:

Antisite imperfections in quaternary Heusler alloys may impact their magnetic properties, particularly the total magnetic moment ($\mu_{total}$) and the Curie temperature ($T_C$). We have summarised these effects across twelve unique antisite combinations in **Table 16** and **Table 18**. The ideal CoFeMnAl supercell configuration, with a total magnetic moment of 24.00 $\mu_B$ and a Curie temperature of 557 K, is mandatory for our investigation. The introduction of antisite disorder disrupts the d-orbital hybridisation between the transition metals (Co, Fe, Mn). This disturbance can modify both the magnetisation and the exchange interactions that define the ferromagnetic state and its thermal stability. For instance, we noted that many antisite defects increase both the total magnetic moment and the Curie temperature, indicating a more robust ferromagnetic state.

The antisites $Fe_{Al}$, $Mn_{Co}$, $Co_{Al}$, $Co_{Fe}$, $Co_{Mn}$, $Al_{Fe}$, and $Fe_{Mn}$ all enhance $\mu_{total}$ and $T_C$. The $Fe_{Al}$ antisite demonstrates a noticeable enhancement in both characteristics, with $\mu_{total}$ attaining 29 $\mu_B$ and $T_C$ reaching 667 K followed by $Mn_{Co}$ antisite which exhibits an increase to 28 $\mu_B$ and 646 K. Conversely, defects such as $Al_{Mn}$ antisite result in decreasing $\mu_{total}$ to 20.00 $\mu_B$ and $T_C$ to 468 K, suggesting reduced magnetic interactions. The magnetic moment for the $Fe_{Mn}$ antisite is 25 $\mu_B$ (3.12 $\mu_B$/*f*.u), closely matching the experimental value measured at 5 K. This indicates that this particular arrangement may represent the material's magnetic state under standard synthesis conditions. The $Al_{Co}$ antisite preserves the magnetic moment and Curie temperature of the ideal structure, showing its thermal stability relative to the ordered configuration. These defects may affect the validity of the Slater-Pauling rule. The total number of valence electrons for an ideal 32-atom supercell of CoFeMnAl is 216. Assuming optimal half-metallicity and the rigid band model during an antisite substitution (e.g., Y → X), we can forecast the total magnetic moment by counting valence electrons and modifying the slater equation:

$$\mu_{total_{supercell}} = (3 \times 8) + (V_X - V_Y) = 24 + (V_X - V_Y)\mu_B \quad (24)$$

Or:

$$\mu_{total} = 3 + \frac{(V_X - V_Y)}{8}\mu_B/f.u \quad (25)$$

The total number of valence electrons is modified by $V_X - V_Y$, $V_X$ and $V_Y$ are the valence electrons of the substituting and substituted atoms, respectively.

For example, $Co_{Fe}$ antisite reduces the supercell's total valence electrons by 1.

$$\mu_{total}(\mathrm{Co_{Fe}}) = 24 + 1 = 25\ \mu_B$$

we would anticipate an integer total moment of 23 $\mu_B$ for the 32-atom defected supercell. By normalising this to the formula unit (divided by 8, as our 32-atom supercell contains eight formula units), we derive an expected moment of $\mu_{total} = 25/8 = 3.125\ \mu_B/f.u.$ Moreover, the total magnetic moment values obtained for these disordered structures, as presented in **Table 16** (even when normalised to the 32-atom supercell), frequently deviate significantly from these straight forward expectations. Specific configurations such as $Al_{Co}$, $Al_{Fe}$, $Al_{Mn}$, $Fe_{Co}$, $Fe_{Mn}$, $Fe_{Al}$, and $Mn_{Co}$ antisites produce total supercell moments that are integer values, e.g., Ideal at 24.0 $\mu_B$, $Al_{Mn}$ at 20.0 $\mu_B$, $Fe_{Al}$ at 29.0 $\mu_B$). In contrast, others, including $Co_{Al}$ (26.24 $\mu_B$), $Co_{Fe}$ (26.24 $\mu_B$), $Co_{Mn}$ (26.16 $\mu_B$), $Mn_{Fe}$ (21.84 $\mu_B$), and $Mn_{Al}$ (22.56 $\mu_B$), lead to non-integer values for the complete supercell indicating that the simple Slater-Pauling rule is not entirely relevant to these disordered systems. These deviations and complex behaviours occur due to the influence of antisite defects on the hybridisation interactions and crystal field splitting of the transition metal d-orbitals. Modifications in bond lengths, orbital overlaps, and the surrounding atomic environment of the defect significantly influence these factors.

This enhancement is driven by the introduction of a large local magnetic moment [27] on the Al site; for the Fe-Al swap, the Fe atom exhibits a strong moment of 2.724 $\mu_B$, which is not offset by the nearly non-magnetic Al atom it replaces. These swap defects also affect the validity of the Slater-Pauling rule. The total magnetic moment values for the entire 32-atom supercells, as derived from **Table 14**, indicate that the CoFe, FeMn, CoMn and MnAl swaps yield exact integer total moments of 24.00 $\mu_B$. CoAl and FeAl swaps have an integer $\mu_{total}$ of 30.00 $\mu_B$ but still deviate from the simple Slater-Pauling rule, since all six types of swap disorder have the same total number of valence electrons and must have the same magnetic moment value of 24.00 μB. This deviation is a direct result of the strong local moment induction on the Al site, an effect not accounted for by the rule.

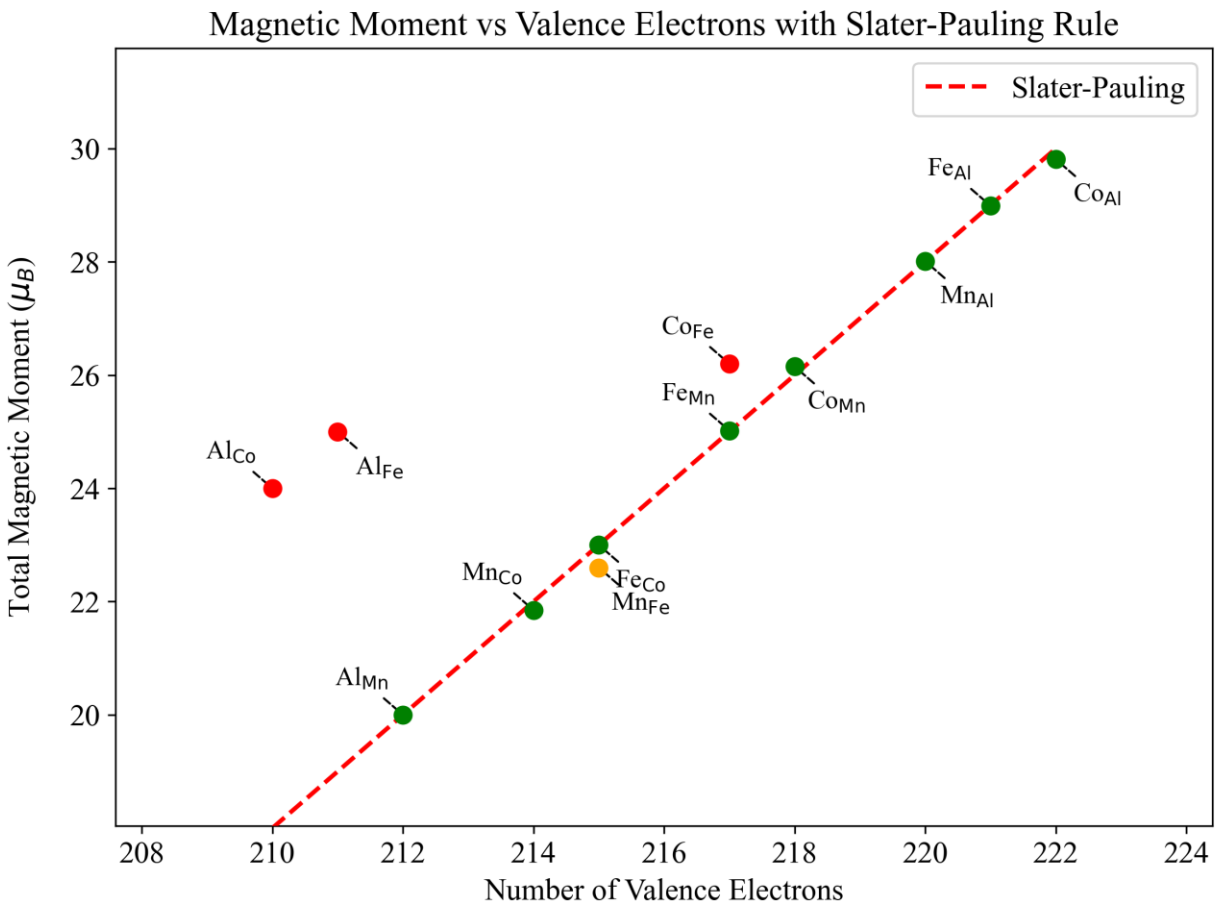


**Figure 41.** Magnetic moment vs valence electrons for defected CoFeMnAl.

### III.4.4. Formation Energy of Swap Disordered Structure:

In the same manner to investigate the effects of swap disorder on CoFeMnAl, we created 32 atoms supercells and we studied all 6 distinct kinds of swap disorder: CoAl, CoFe, CoMn, FeMn, FeAl, and MnAl.

Based on the analysis of formation energies and pair binding energies, MnAl has been identified as the most stable swap defect. It has a negative formation energy of – 1.23 eV and a high positive binding energy of 1.76 eV, showing that it is energetically easier to form and that this structure is stable with its corresponding antisite pairs, MnAl and AlMn. CoFe, although relatively stable with a negative formation energy of – 0.13 eV and a binding energy of 0.06 eV, is less stable than MnAl. CoMn and FeMn swaps have positive formation energies, indicating lower stability. Although not easily removed, they may still

impact on the material's formation. CoAl and FeAl, despite their high formation energies of 1.89 eV and 1.33 eV, respectively, can be eliminated.

**Table 17:** The formation energy of disorder $E_{fd}$ in (eV), the pair binding energy $E_b$ in (eV), the magnetic moment $\mu_{total}$ ($\mu_B/f.u$), polarization (%) and width of spin down gap $W_{gap}$ (eV) of possible structures with swap disorder.

| Swap | $E_{fd}$ | $E_b$ | *Polarisation* | $W_{gap}$ | $\mu_{total}$ | $T_C$ |
|---|---|---|---|---|---|---|
| **Ideal** | | | 98.58 | 0.62 | 24.00 | 557 |
| **CoAl** | 1.89 | 0.56 | 92.97 | 0.00 | 30.00 | 673 |
| **CoFe** | -0.13 | 0.06 | 98.97 | 0.47 | 24.00 | 558 |
| **CoMn** | 0.86 | 0.04 | 65.53 | 0.00 | 24.08 | 560 |
| **FeMn** | 0.08 | -0.84 | 99.61 | 0.36 | 24.00 | 558 |
| **FeAl** | 1.33 | 0.33 | 97.48 | 0.28 | 30.00 | 672 |
| **MnAl** | -1.23 | 1.76 | 98.39 | 0.33 | 24.00 | 556 |

## III.4.5. Effect of Swap Disorder on the Electronic Properties:

The density of states (DOS) and band structures (BS) for all six swap configurations are illustrated in (**Figure 42**), (**Figure 44**) and (**Figure 43**) respectively, with pertinent data summarised in **Table 17**. The investigation of these configurations similarly indicates effects ranging from total annihilation to strong maintenance of half-metallicity.

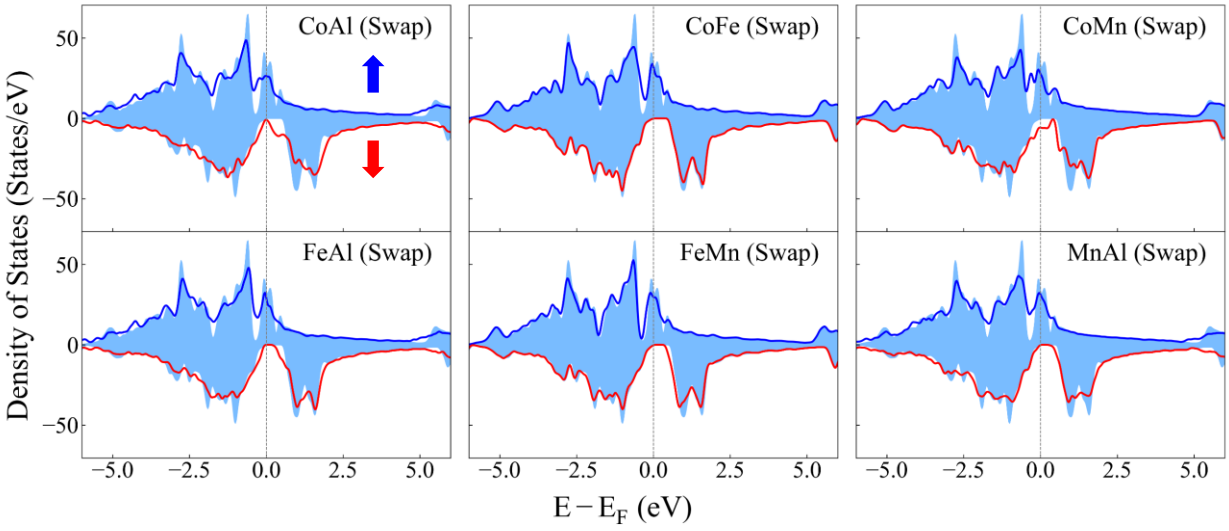


**Figure 42.** The total density of states of possible kinds of swap disordered structures. The shadow region is the DOS of ideal CoFeMnAl, the red solid line is the DOS of antisite disordered structures.

The configurations of CoAl and CoMn swaps destroy half-metallicity, demonstrating no gap in the minority spin channel and notably diminished polarisations (92.97% for CoAl and 65.53% for CoMn).

The band structures reveal states overlapping the Fermi level in the minority spin channel. However, the CoFe, FeMn, FeAl, and MnAl swap structures perfectly maintain the half-metallic character but reveal band gap sensitivity to this type of disorder.

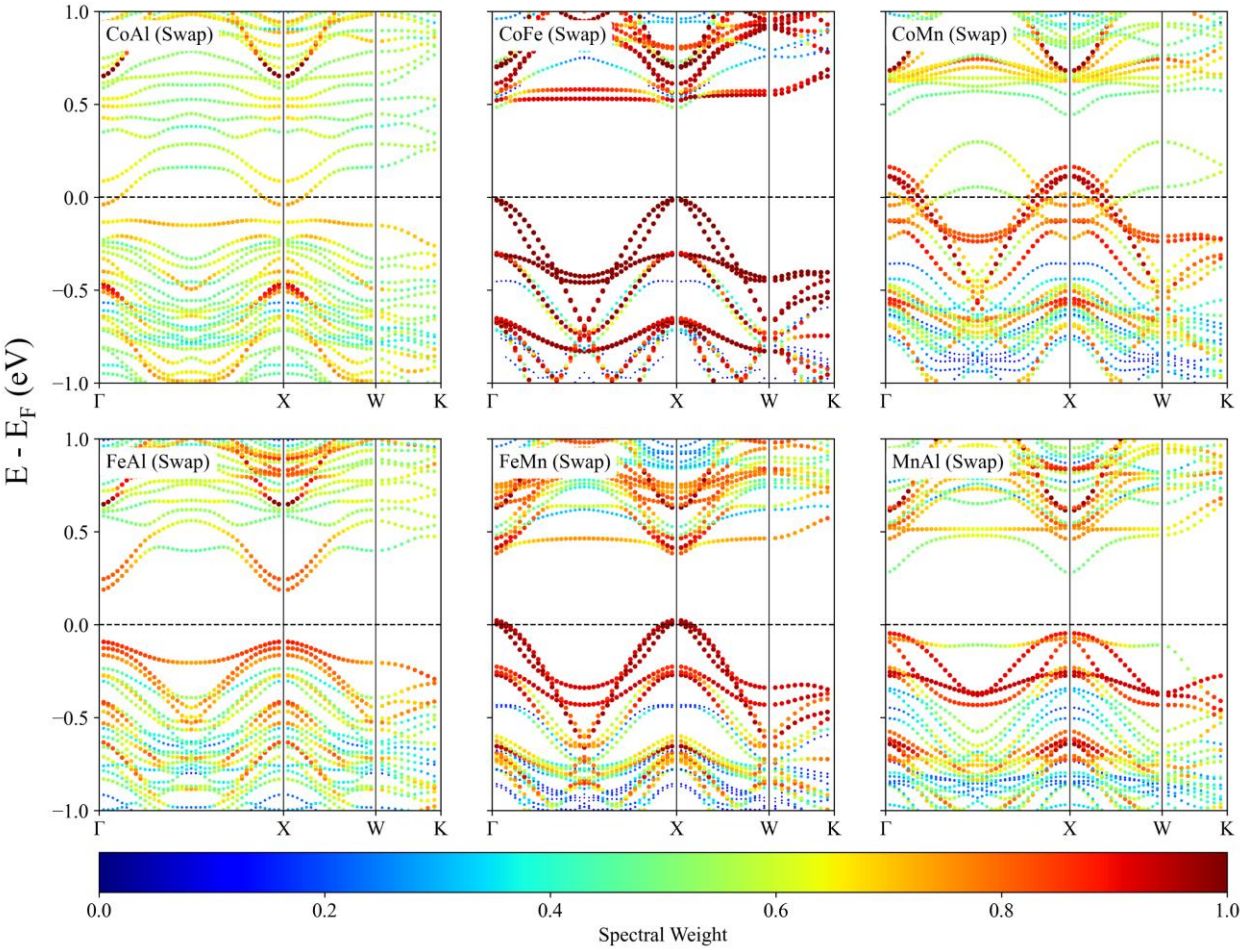


**Figure 43.** The band structure of six possible kinds of swap disordered structures for CoFeMnAl compound.

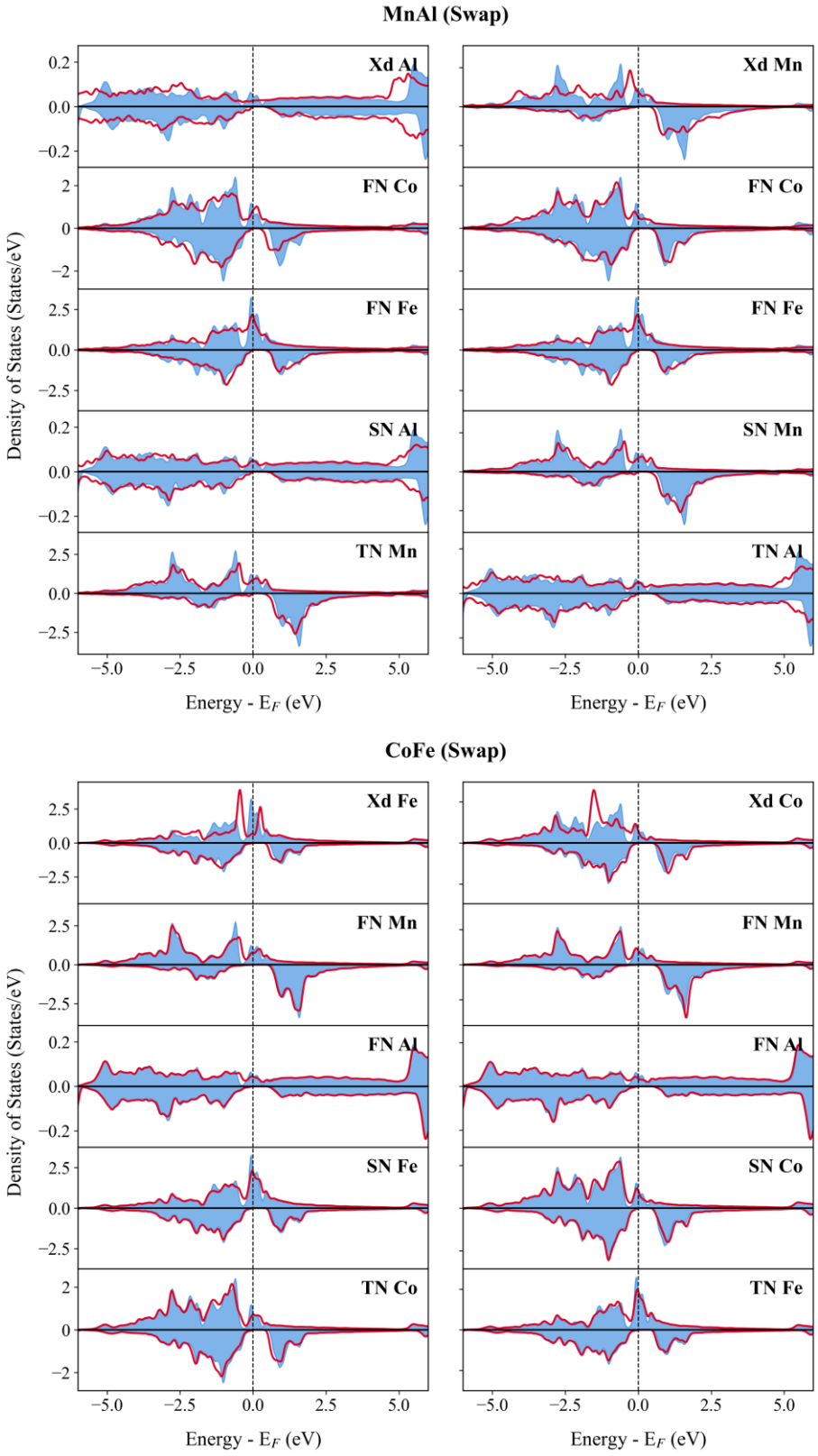


**Figure 44.** The PDOS of most favourable swap defect structures. The FN, SN and TN are respectively the first-neighbour, second-neighbour and third neighbour of defective atom, the blue shadow is the PDOS of corresponding atom in perfect CoFeMnAl.

### III.4.6. Effect of Swap Disorder on the Magnetic Properties

Beyond antisite imperfections, swap disorder, arising from the interchange of atomic positions, also influences the magnetic properties. From **Table 17** and **Table 14**, CoFe, FeMn, CoMn, and MnAl swaps maintain a total magnetic moment of 24.00 $\mu_B$. This is attributed to a local moment compensation; for the CoFe swap, the negative moment induced at the Fe(Co) site (-0.37 $\mu_B$) is effectively balanced by the positive moment at the Co(Fe) site (0.94 $\mu_B$). Their Curie temperatures are very close, with CoFe and FeMn swaps at 558 K and MnAl at 556 K. These particular swap disorders have minimal effect on overall magnetisation and the thermal stability of the ferromagnetic state.

**Table 18:** The calculated total magnetic moment $\mu_{tot}$ of four most favourable defective structures, magnetic moment of defective atoms ($X_d$) and its first-neighbour atom (FN), second-neighbour atom (SN) as well as third neighbour atom (TN).

| System | **Al($\mu_B$)** | **Co($\mu_B$)** | **Fe($\mu_B$)** | **Mn($\mu_B$)** | **$\mu_{tot}$($\mu_B$)** |
|---|---|---|---|---|---|
| **Perfect** | -0.034 | 0.816 | -0.135 | 2.445 | 24 |
| **Defect** | **$X_d$** | **FN** | **SN** | **TN** | **$\mu_{tot}$($\mu_B$)** |
| **$Fe_{Al}$** | Fe: 2.724 | Co: 0.999<br>Fe: 0.490 | Mn: 2.420 | Al: -0.049 | 29 |
| **$Fe_{Co}$** | Fe: -0.483 | Mn: 2.431<br>Al: -0.027 | Fe: -0.117 | Co: 0.778 | 23 |
| **$Fe_{Mn}$** | Fe: 2.634 | Co: 0.818<br>Fe: 0.323 | Al: -0.035 | Mn: 2.344 | 25 |
| **CoFe** | Fe: -0.369<br>Co: 0.944 | Mn: 2.556<br>Al: -0.035 | Fe: -0.200<br>Co: 0.827 | Co: 0.752<br>Fe: -0.139 | 24 |
| **AlMn** | Al: -0.015<br>Mn: 2.615 | Co: 0.923<br>Fe: 0.136 | Al: -0.042<br>Mn: 2.416 | Mn: 2.416<br>Al: -0.042 | 24 |

On the contrary, the CoAl and FeAl swap configurations increase $\mu_{total}$ to 30 $\mu_B$ and the Curie temperatures to 673 K and 672 K, respectively, indicating a significant modification of d-orbital hybridisation and associated exchange interactions. This enhancement is driven by the introduction of a large local magnetic moment [27] on the Al site; for the FeAl swap, the Fe atom exhibits a strong moment of 2.724 $\mu_B$, which is not offset by the nearly non-magnetic Al atom it replaces. These swap defects also affect the validity of the Slater-

Pauling rule. The total magnetic moment values for the entire 32-atom supercells, as derived from **Table 17**, indicate that the CoFe, FeMn, CoMn and MnAl swaps yield exact integer total moments of 24.00 $\mu_B$. CoAl and FeAl swaps have an integer $\mu_{total}$ of 30.00 $\mu_B$ but still deviate from the simple Slater-Pauling rule, since all six types of swap disorder have the same total number of valence electrons and must have the same magnetic moment value of 24.00 $\mu_B$. This deviation is a direct result of the strong local moment induction on the Al site, an effect not accounted for by the rule.

## References:


[1] P. Blaha, K. Schwarz, F. Tran, R. Laskowski, G. K. H. Madsen, and L. D. Marks, "WIEN2k: An APW+lo program for calculating the properties of solids," *Journal of Chemical Physics*, vol. 152, no. 7, Feb. 2020, doi: 10.1063/1.5143061/16727314/074101_1_ACCEPTED_MANUSCRIPT.PDF.

[2] W. Kohn and L. J. Sham, "Self-consistent equations including exchange and correlation effects," *Physical Review*, vol. 140, no. 4A, p. A1133, Nov. 1965, doi: 10.1103/PHYSREV.140.A1133/FIGURE/1/THUMB.

[3] K. Schwarz and P. Blaha, "Solid state calculations using WIEN2k," *Comput Mater Sci*, vol. 28, no. 2, pp. 259–273, Oct. 2003, doi: 10.1016/S0927-0256(03)00112-5.

[4] P. Blaha, K. Schwarz, P. Sorantin, and S. B. Trickey, "Full-potential, linearized augmented plane wave programs for crystalline systems," *Comput Phys Commun*, vol. 59, no. 2, pp. 399–415, Jun. 1990, doi: 10.1016/0010-4655(90)90187-6.

[5] J. P. Perdew and K. Burke, "Generalized gradient approximation for the exchange-correlation hole of a many-electron system," *Phys Rev B*, vol. 54, no. 23, p. 16533, Dec. 1996, doi: 10.1103/PhysRevB.54.16533.

[6] M. J. L. Sangster and A. R. Q. Hussain, "The supercell method for calculating responses in defective lattices," *Physica B+C*, vol. 131, no. 1–3, pp. 119–125, Aug. 1985, doi: 10.1016/0378-4363(85)90145-7.

[7] C. G. Van De Walle and J. Neugebauer, "First-principles calculations for defects and impurities: Applications to III-nitrides," *J Appl Phys*, vol. 95, no. 8, pp. 3851–3879, Apr. 2004, doi: 10.1063/1.1682673.

[8] A. Togo, "First-principles Phonon Calculations with Phonopy and Phono3py," *J. Phys. Soc. Japan*, vol. 92, no. 1, p. 012001, Jan. 2023, doi: 10.7566/jpsj.92.012001.

[9] A. Togo, L. Chaput, T. Tadano, and I. Tanaka, "Implementation strategies in phonopy and phono3py," *Journal of Physics: Condensed Matter*, vol. 35, no. 35, p. 353001, Jun. 2023, doi: 10.1088/1361-648X/ACD831.

[10] H. Ebert, D. Ködderitzsch, and J. Minár, “Calculating condensed matter properties using the KKR-Green’s function method—recent developments and applications,” *Reports on Progress in Physics*, vol. 74, no. 9, p. 096501, Aug. 2011, doi: 10.1088/0034-4885/74/9/096501.

[11] S. H. Vosko, L. Wilk, and M. Nusair, “Accurate spin-dependent electron liquid correlation energies for local spin density calculations: a critical analysis,” *Can J Phys*, vol. 58, no. 8, pp. 1200–1211, Aug. 1980, doi: 10.1139/P80-159.

[12] R. F. L. Evans, W. J. Fan, P. Chureemart, T. A. Ostler, M. O. A. Ellis, and R. W. Chantrell, “Atomistic spin model simulations of magnetic nanomaterials,” *Journal of Physics: Condensed Matter*, vol. 26, no. 10, p. 103202, Feb. 2014, doi: 10.1088/0953-8984/26/10/103202.

[13] V. G. Tyuterev and N. Vast, “Murnaghan’s equation of state for the electronic ground state energy,” *Comput Mater Sci*, vol. 38, no. 2, pp. 350–353, Dec. 2006, doi: 10.1016/J.COMMATSCI.2005.08.012.

[14] J.S. Zhao, Q. Gao, L. Li, H.H. Xie, X.R. Hu, C.L. Xu and J.B. Deng, First-principles study of the structure, electronic, magnetic and elastic properties of half-Heusler compounds LiXGe (X = Ca, Sr and Ba). Intermetallics 89 (2017), pp. 65–73.

[15] F. Mouhat and F. X. Coudert, “Necessary and sufficient elastic stability conditions in various crystal systems,” *Phys Rev B*, vol. 90, no. 22, p. 224104, Dec. 2014, doi: 10.1103/PhysRevB.90.224104.

[16] F. Benlakhdar *et al.*, “Structural, elastic, mechanical and optoelectronic properties of zinc-doped SrTiO3 perovskite compounds,” *Modern Physics Letters B*, vol. 38, no. 1, Jan. 2024, doi: 10.1142/S0217984923502007/ASSET/IMAGES/LARGE/S0217984923502007FIGF10.JPEG.

[17] H. Abbassa, A. Labdelli, S. Meskine, Y. B. Cherif, and A. Boukortt, “Half-metallic properties in Co2XSn (X = Ti, V and Cr) full-Heusler compound,” *https://doi.org/10.1142/S0217984920500281*, vol. 34, no. 2, Dec. 2019, doi: 10.1142/S0217984920500281.

[18] X. P. Wei, X. Zhang, J. Shen, W. L. Chang, and X. Tao, “Gilbert damping, electronic and magnetic properties for quaternary Heusler alloys CrYCoZ: First-principles and Monte Carlo studies,” *Comput Mater Sci*, vol. 210, Jul. 2022, doi: 10.1016/j.commatsci.2022.111453.

[19] L. Bainsla and K. G. Suresh, “Equiatomic quaternary Heusler alloys: a material perspective for spintronic applications.”

[20] L. Latreche, H. Abbassa, E. H. Abbes, and A. Boukortt, “First-Principles Investigation of the Influence of Disorder on Electronic and Magnetic Properties in CoFeMnAl Quaternary Heusler Alloys,” *Journal of Superconductivity and Novel Magnetism 2025 38:5*, vol. 38, no. 5, pp. 1–19, Sep. 2025, doi: 10.1007/S10948-025-07048-W.

[21] V. Alijani *et al.*, “Electronic, structural, and magnetic properties of the half-metallic ferromagnetic quaternary Heusler compounds CoFeMnZ (Z=Al, Ga, Si, Ge),” *Phys Rev B Condens Matter Mater Phys*, vol. 84, no. 22, Dec. 2011, doi: 10.1103/PhysRevB.84.224416.

[22] I. Galanakis, K. Özdoğan, B. Aktaş, and E. Şaşioğlu, “Effect of doping and disorder on the half metallicity of full Heusler alloys 042502,” *Appl Phys Lett*, vol. 89, no. 4, Jul. 2006, doi: 10.1063/1.2235913/986460.

[23] I. Galanakis, “Slater–Pauling Behavior in Half-Metallic Heusler Compounds,” *Nanomaterials 2023, Vol. 13, Page 2010*, vol. 13, no. 13, p. 2010, Jul. 2023, doi: 10.3390/NANO13132010.

[24] K. Özdoğan, E. Şaşioğlu, and I. Galanakis, “Slater-Pauling behavior in LiMgPdSn-type multifunctional quaternary Heusler materials: Half-metallicity, spin-gapless and magnetic semiconductors,” *J Appl Phys*, vol. 113, no. 19, May 2013, doi: 10.1063/1.4805063/370344.

[25] X. P. Wei *et al.*, “Exchange interactions and Curie temperatures in Fe2 NiZ compounds,” *J Alloys Compd*, vol. 694, pp. 1254–1259, Feb. 2017, doi: 10.1016/J.JALLCOM.2016.10.105.

[26] X. P. Wei and Y. H. Zhou, “First-principles and Monte Carlo studies of the Fe2NiZ compounds on exchange interactions and Curie temperatures,” *Intermetallics (Barking)*, vol. 93, pp. 283–289, Feb. 2018, doi: 10.1016/j.intermet.2017.10.006.

[27] X. P. Wei, J. R. Liu, X. Zhang, W. L. Chang, and X. Tao, “Defect effect on the stability, electronic and magnetic properties equal-atomic CrLaCoAl alloy by the first-principles calculations,” *Appl Phys A Mater Sci Process*, vol. 128, no. 10, pp. 1–10, Oct. 2022, doi: 10.1007/S00339-022-06070-2/METRICS.

# Conclusion and further research:

The influence of antisite and swap defects on the electronic and magnetic properties of the CoFeMnZ (Z = Ge; Al) quaternary Heusler alloy was investigated using first-principles calculations based on Density Functional Theory (DFT), supercell approach and Monte Carlo simulation. Results for the ideal structure show that the Type I atomic arrangement with a ferromagnetic (FM) state is the most energetically favourable ground state for both compounds. The ordered structure satisfies the requirements for mechanical stability and is classified as a ductile material; however, phonon calculations indicate the absence of imaginary frequencies, signifying that the perfect crystal is dynamically stable. Electronic structure calculations indicate that the ordered CoFeMnGe alloy behaves as a nearly-half-metallic ferromagnet with 0.15 eV gap. A systematic analysis of 18 different defect types shows that disorder is often energetically favourable; the $Fe_{Ge}$ antisite is identified as the most probable defect with a formation energy of -9.98 eV, followed by the $Fe_{Mn}$, $Co_{Ge}$, $Co_{Mn}$ and $Fe_{Co}$ antisites. Defects significantly affect the characteristics of the material. The spin-down gap ($W_{gap}$) is notably influenced, varying from 0.00 eV to 0.60 eV across various disorder configurations. $Co_{Ge}$, $Co_{Mn}$ ,$Ge_{Fe}$ antisite, CoGe and CoMn swap defects destroy half-metallicity completely, underscoring the imperative necessity of avoiding these configurations during experimental synthesis. Moreover, structural disorder is evident in the magnetic aspects; the total magnetic moment ($\mu_{total}$) swings significantly between 29.13 $\mu_B$ and 38 $\mu_B$, while the polarisation spans from 51.05% to 99.95% across all antisite and swap disorder types. The calculated magnetic moment for the $Fe_{Mn}$ antisite arrangement is 4.125 $\mu_B$/*f.u*, closely aligning with the experimental value of 4.2 $\mu_B$. The Curie temperature varies from 527 K to 683 K, in reference to 579 K for the pristine structure. CoFeMnAl alloy behaves as a half-metallic ferromagnet, exhibiting an integer magnetic moment of 3.00 $\mu_B$/*f.u* in accordance with the Slater-Pauling rule. The origin of the 0.62 eV half-metallic gap is the hybridization of Co, Fe, and Mn d-orbitals, which pushes the minority spin states away from the Fermi level. A systematic analysis of 18 different defect types shows that disorder is often energetically favourable; the $Fe_{Mn}$ antisite is identified as the most probable defect with a formation energy of -1.25 eV, followed by the MnAl swap and $Fe_{Al}$ antisite. Defects significantly affect the characteristics

of the material. The spin-down gap ($W_{gap}$) ranges from 0.00 eV to 0.58 eV across various disorder configurations. $Co_{Al}$, $Co_{Mn}$ antisite, CoAl and CoMn swap defects entirely destroy half-metallicity, underscoring the imperative necessity of avoiding these configurations during experimental synthesis. Moreover, structural disorder is evident in the magnetic aspects; the total magnetic moment ($\mu_{total}$) swings significantly between 20 $\mu_B$ and 30 $\mu_B$, while the polarisation spans from 65.53% to 99.95% across all antisite and swap disorder types. The calculated magnetic moment for the $Fe_{Mn}$ antisite arrangement is 3.12 $\mu_B$/*f.u*, closely aligning with the experimental value of 3.10 $\mu_B$. The Curie temperature varies from 468 K to 673 K, in reference to 557 K for the pristine structure. Our research highlights the significance of atomic disorder in predicting the properties of Heusler alloys, offering crucial insights for the development of durable material options for spintronic applications.

We successfully modelled collinear ferromagnetism; however, the presence of heavy elements (such as Ge) and the broken inversion symmetry in disordered local environments indicate the potential occurrence of Dzyaloshinskii-Moriya Interactions (DMI). Future research may investigate non-collinear magnetic configurations, including spin spirals or skyrmions, within these disordered Heusler systems, which would be highly relevant for next-generation spintronics applications.

# Scientific production:

Journal of Superconductivity and Novel Magnetism (2025) 38:216
https://doi.org/10.1007/s10948-025-07048-w

RESEARCH

## First-Principles Investigation of the Influence of Disorder on Electronic and Magnetic Properties in CoFeMnAl Quaternary Heusler Alloys

Laid Latreche[1] · Hamza Abbassa[1,2] · El Habib Abbes[1,3] · Abdelkader Boukortt[1]

Received: 1 March 2025 / Accepted: 28 August 2025


**Abstract**
First-principles calculations, combined with the supercell approach, are employed to investigate the effects of atomic disorder on the electronic properties of the CoFeMnAl quaternary Heusler alloy (LiMgPdSn-type). The ordered alloy is a half-metallic ferromagnet; its moment obeys the Slater-Pauling rule with $T_C > 300$ K. We analyse twelve antisite and six swap disorder configurations. Calculations show that the $Fe_{Mn}$ antisite is the most energetically favourable defect (−1.25 eV), followed by the FeCo antisite and the MnAl swap. The disorder generally contracts the spin-down gap. Half-metallicity is largely preserved but completely lost for $Co_{Al}$, $Co_{Mn}$ antisite and CoAl, CoMn swap defects. Disorder has a significant effect on the magnetic moment and Curie temperature. The $Fe_{Mn}$ antisite gives 3.12 $\mu_B$, which is very close to the experimental value of 3.10 $\mu_B$. This study demonstrates the importance of considering disorder when predicting the properties of Heusler alloys.

**Keywords** Quaternary Heusler · Disorder · Half metal · FP-LAPW calculations

### 1 Introduction

In recent years, Heusler alloys have attracted considerable attention due to their diverse properties and broad potential applications. These compounds exhibit interesting and diverse magnetic properties [1–4], such as itinerant and localised magnetism, giant magnetoresistance, and magnetic shape-memory effects. Such characteristics made them promising for advanced technological topics beyond spintronics [5–7]. Heusler alloys comprise a large group of intermetallic compounds, typically with compositions such as $X_2YZ$ or XY′Z, where X and Y are transition metals, and Z is a main group element [8]. They usually crystallise in cubic space groups, such as Fm-3m or F-43m. The electronic and magnetic properties of this group of compounds are highly dependent on the distribution of the constituent elements in the crystallographic sites. These materials often exhibit a certain level of atomic disorder, making them suitable for investigating the effects of disorder and variations in electron concentration on their magnetic properties [9]. Quaternary Heusler alloys (XX′YZ) represent more advanced evolution within the Heusler family and offer enhanced flexibility in compositional and site engineering [10, 11]. This versatility facilitates the realisation of crucial spintronic features, including half-metallicity where one spin channel conducts while the other is insulating, leading to fully spin-polarised conduction electrons. Numerous Heusler alloys also exhibit high Curie temperatures, and their magnetic moments often adhere to the generalised Slater-Pauling rule, underscoring their robust ferromagnetic order, which is essential for practical applications. First-principles calculations, utilising advanced methods like the supercell approach within Density Functional Theory and SPRKKR, are indispensable tools for investigating these properties, along with thermodynamic and mechanical stability. The CoFeMnAl equiatomic quaternary Heusler (EQH) is a half-metallic ferromagnet with an integer magnetic moment of 3.0 $\mu_B$ and possessing a Curie temperature above 300 K. Despite these promising properties of its ideal ordered structure, the impact of atomic disorder is an inherent and unavoidable aspect during the experimental synthesis; CoFeMnAl's

✉ Laid Latreche
latreche.laid@gmail.com

[1] Elaboration and Characterization Physical Mechanics and Metallurgical of Materials Laboratory (ECP3M), Abdelhamid Ibn Badis University, Mostaganem, Algeria

[2] Department of Physics, Faculty of Exact Sciences and Computer Science, Abdelhamid Ibn Badis University, Mostaganem, Algeria

[3] Department of Physics, Higher Normal School of Mostaganem, Mostaganem, Algeria

Published online: 29 September 2025

جامعة الجيلالي اليابس بسيدي بلعباس
Djillali Liabès University , Sidi Bel-Abbès
Faculty of Exact Sciences
Physics Department
Physico-Chemistry Laboratory Of Advanced Materials (LPCMA)

The 3rd edition of the international conference on materials science and engineering and their impact on the environment ICMSE'2024

Sidi bel abbés May 29-30, 2024

# CERTIFICATE OF PARTICIPATION

The scientific committee certified that:

*Mr. Latreche Laid*

Has presented poster Communication, entitled:

« *Effect of swap defect on the electronic and magnetic properties of quaternary heuslers alloys* ».

CO-AUTHORS : Hamza Abbassa .

General Chair:

THE INTERNATIONAL CONFERENCE ON MATERIALS SCIENCE AND ENGINEERING AND THEIR IMPACT ON THE ENVIRONMENT
ICMSE 2024 - MAY 29 - 30
CHAIRMAN
Prof Mohammed AMERI

Physico-Chemistry Laboratory Of Advanced Materials (LPCMA), Djillali Liabès University , Sidi Bel-Abbès
Tél. : 048 79 90 02/048 74 56 19, Email: lttnsameri@yahoo.fr , https://www.univ-sba.dz/lpcma/

République Algérienne Démocratique et Populaire
Ministère de l'enseignement supérieur et de la Recherche Scientifique
École Normale Supérieure de Mostaganem

# Attestation de participation

Le Directeur de l'École Normale Supérieure de Mostaganem et les présidents du colloque attestent que :

*Dr. Laid Latreche*

Laboratoire ECP3M , Université de Mostaganem

A présenté une communication intitulée « **Prédiction des Paramètres de Maille des Alliages Heusler Quaternaires par Apprentissage Automatique** » dans le cadre du colloque national en ligne intitulé « **L'intelligence artificielle dans la recherche scientifique innovation responsable et optimisation** » organisé le **22 novembre 2025** par l'École Normale Supérieure de Mostaganem .

**Dr AMAMRA Laid**
**ENS de Mostaganem**
**Président du colloque**

**Dre MESSOUS Khansa**
**ENS de Mostaganem**
**Présidente du colloque**

**Dr MANSERI Kada**
**Directeur de l'ENS de Mostaganem**

Manifestations Scientifiques Nationales et Internationales


People's Democratic Republic of Algeria
Ministry of Higher Education and Scientific Research
University AHMED ZABANA of Relizane
Faculty of Science and Technology
Civil Engineering and Publics Works Department
Innovative Materials Laboratory and Renewable Energies
LMIER
RSDT
CERTIFICATE OF PARTICIPATION
THIS CERTIFICATE IS PROUDLY PRESENTED TO:
Laid Latreche
In technical presentation, recognition and appreciation of contributions to the
Second Edition of the International Seminar on Materials and Engineering Structures (ISMES"25)
Held in Relizane, Algeria, during February 07-08, 2026, with the paper entitled:
Effect of Pressure on the Electronic and Magnetic Properties of the Quaternary Heusler Alloy CoFeMnSb
Co-authors: Abdesamed benbedra , El Habib abbes , Hamza abbassa
Seminar Chairwoman
Vice Dean of the faculty
Chair Women
LAOUFI Imene
Sponsors :
SELMA
ADM PROMOTION
ENTEC
Bamberg
ISMES'25


People's Democratic Republic of Algeria
Ministry of Higher Education and Scientific Research
University AHMED ZABANA of Relizane
Faculty of Science and Technology
Civil Engineering and Publics Works Department
Innovative Materials Laboratory and Renewable Energies
LMIER
RSDT
CERTIFICATE OF PARTICIPATION
THIS CERTIFICATE IS PROUDLY PRESENTED TO:
Laid Latreche
In technical presentation, recognition and appreciation of contributions to the
Second Edition of the International Seminar on Materials and Engineering Structures (ISMES"25)
Held in Relizane, Algeria, during February 07-08, 2026, with the paper entitled:
The Role of Structural Disorder in Modulating the Electronic and Magnetic Properties of Heusler Alloys:
A First-Principles Analysis and Monte Carlo Simulation
Co-authors: Abdesamed benbedra , El Habib abbes , Hamza abbassa , Abdelkader boukortt
Seminar Chairwoman
Vice Dean of the faculty
Chair Women
LAOUFI Imene
Sponsors :
SELMA
ADM PROMOTION
ENTEC
Bamberg
ISMES'25